FEDERAL UNIVERSITY OF TECHNOLOGY - PARANÁ
DEPARTMENT OF MECHANICAL ENGINEERING
POSTGRADUATE PROGRAM IN MECHANICAL AND MATERIALS ENGINEERING

RODRIGO SALDANHA ROMANUS

DIRECT NUMERICAL SIMULATION OF SPHEROIDAL PARTICLE SETTLING IN VISCOPLASTIC FLUID USING LATTICE BOLTZMANN METHOD

MSc Project

CURITIBA
2020

RODRIGO SALDANHA ROMANUS

DIRECT NUMERICAL SIMULATION OF SPHEROIDAL PARTICLE SETTLING IN VISCOPLASTIC FLUID USING LATTICE BOLTZMANN METHOD

Simulação Numérica Direta de Partícula Esferoidal Sedimentando em Fluido Viscoplástico Utilizando Método Lattice Boltzmann

MSc Project presented to the Postgraduate Program in Mechanical and Materials Engineering – PPGEM from the Federal University of Technology – Paraná, as fulfillment of requirements for the Master degree in Mechanical Engineering.

Supervisor: Prof. Admilson Teixeira Franco, Dr.
Co-Supervisor: Alan Lugarini de Souza, MSc.

CURITIBA

2020

Dados Internacionais de Catalogação na Publicação

Romanus, Rodrigo Saldanha
Direct numerical simulation of spheroidal particle settling in viscoplastic fluid using lattice Boltzmann method [recurso eletrônico] / Rodrigo Saldanha Romanus. -- 2020.
1 arquivo texto (119 f.): PDF; 5,9 MB.

Modo de acesso: World Wide Web.
Título extraído da tela de título (visualizado em 31 out. 2020).
Texto em inglês com resumo em português.
Dissertação (Mestrado) - Universidade Tecnológica Federal do Paraná. Programa de Pós-graduação em Engenharia Mecânica e de Materiais, Curitiba, 2020.
Bibliografia: f. 95-102.

1. Engenharia mecânica - Dissertações. 2. Método Lattice Boltzmann. 3. Dinâmica da partícula. 4. Materiais viscoelásticos. 5. Fluidos não-newtonianos. I. Franco, Admilson Teixeira, orient. II. Souza, Alan Lugarini, coorient. III. Universidade Tecnológica Federal do Paraná - Programa de Pós-graduação em Engenharia Mecânica e de Materiais, inst. IV. Título.

CDD: Ed. 23 -- 620.1

Biblioteca Ecoville da UTFPR, Câmpus Curitiba
Bibliotecária: Lucia Ferreira Littiere – CRB 9/1271
Aluna de Biblioteconomia: Josiane Mangueira

Ministério da Educação
Universidade Tecnológica Federal do Paraná
Diretoria de Pesquisa e Pós-Graduação

UNIVERSIDADE TECNOLÓGICA FEDERAL DO PARANÁ
CAMPUS CURITIBA

TERMO DE APROVAÇÃO DE DISSERTAÇÃO Nº393

A Dissertação de Mestrado intitulada **Direct Numerical Simulation of Spheroidal Particle Settling in Viscoplastic Fluid Using Lattice Boltzmann Method**, defendida em sessão pública pelo(a) candidato(a) **Rodrigo Saldanha Romanus**, no dia 18 de Setembro de 2020, foi julgada para a obtenção do título de Mestre em Engenharia, área de concentração Engenharia Térmica, linha de pesquisa: Mecânica dos Fluidos, e aprovada em sua forma final, pelo Programa de Pós-Graduação em Engenharia Mecânica e de Materiais.

BANCA EXAMINADORA:

Prof. Dr. Admilson Teixeira Franco - Presidente - UTFPR
Prof. Dr. Silvio Luiz de Mello Junqueira - UTFPR
Prof. Christian Naaktgeboren, Ph.D. – UTFPR - Guarapuava
Prof. Dr. Paulo Cesar Philippi - PUC-PR

A via original deste documento encontra-se arquivada na Secretaria do Programa, contendo a assinatura da Coordenação após a entrega da versão corrigida do trabalho.

Curitiba, 18 de Setembro de 2020.

Carimbo e Assinatura do(a) Coordenador(a) do Programa

ACKNOWLEDGEMENTS

This research was carried out at Center for Rheology and Non-Newtonian Fluids (CERNN) at the Federal University of Technology - Paraná (UTFPR) with financial support from the National Council for Scientific and Technological Development of Brazil (CNPq), the Brazilian Coordination for the Improvement of Higher Education (CAPES) - Finance Code 001 and Petrobras. I deeply appreciate this support. I also thank my fellow colleague, Marco A. Ferrari, for stimulating discussions which contributed to this work. I am especially grateful for the technical support provided by Waine B. Oliveira Jr for the development of the computational code in GPU.

I will be forever grateful to my parents, Jurcelis A. Saldanha and Raul C. Romanus, the ones that made me into the person I am today. They raised me and provided everything I needed even in harsh times. I owe them both a debt I will never be able to repay. I would also like to express my appreciation and gratitude to my dear love, Helena B. Góes. She was one of the reasons that I never felt alone amid this difficult period of quarantine. Thank you for being my best friend, and for being a caring and trustworthy partner.

Moreover, I would like to express my great admiration, respect and gratitude to my supervisor, Admilson T. Franco, and to my co-supervisor, Alan Lugarini. Their guidance was essential during the course of this work. I am also thankful to my past coworker and great friend, Yuri B. Matos, for encouraging me to engage in the science career.

Last but not least, I thank the Post-Graduation Program in Mechanical and Materials Engineering at UTFPR for this opportunity and all my previous teachers and professors, which gave me the necessary tools and lighted my way up here.

RESUMO

ROMANUS, Rodrigo Saldanha. **Simulação Numérica Direta de Partícula Esferoidal Sedimentando em Fluido Viscoplástico Utilizando Método Lattice Boltzmann**. 2020. 119 f. Dissertação (Mestrado em Engenharia Mecânica) – Universidade Tecnológica Federal do Paraná. Curitiba, 2020.

Neste documento, é apresentado um estudo numérico da sedimentação de uma partícula elipsoidal em fluido quiescente Newtoniano e viscoplástico. A pesquisa é motivada por seus aspectos teóricos e aplicações industriais, tais como o transporte de sedimentos no setor de exploração de petróleo. Para números de Reynolds moderados a altos, um objeto sob a ação da gravidade requer uma distancia considerável para atingir um regime periódico ou estatisticamente permanente, o que implica em restrições do tamanho máximo do domínio em simulações numéricas diretas (DNS) para essa classe de escoamento, devido a limitações de memória. Algumas alternativas, tais como técnicas de reposicionamento do domínio, permitem simulações em domínios sem fronteiras e são encontradas em métodos espectrais e de diferenças finitas. Por questões de localidade, a utilização do método lattice Boltzmann (LBM) para DNS tem se popularizado cada vez mais. O presente trabalho apresenta uma metodologia de realocação de fronteiras desenvolvida para o LBM que permite simular uma partícula se deslocando em um meio virtualmente infinito. O principio do método consiste no truncamento do domínio do escoamento e realocação das fronteiras, transferindo-as para nós exteriores ao domínio de simulação. O método da fronteira imersa (IBM) é adotado para descrição da interação sólido-líquido. Ao longo do texto, a metodologia para confecção de malhas elipsoidais é detalhada e uma releitura da estratégia de Suzuki e Inamuro (2011) para compensação da massa interna de fluido é desenvolvida. O modelo do fluido de Bingham é então adaptado para o LBM com a adequação apropriada do método de relocação das fronteiras. O algoritmo é então avaliado sequencialmente para cada um de seus recursos, apresentando boa concordância com soluções analíticas e resultados disponíveis na literatura. Também são evidenciadas melhorias nos resultados de acordo com a resolução adotada para o domínio computacional. Foi então realizada investigação da sedimentação de esferoides oblatos em fluido Newtoniano, sendo identificados diversos padrões de movimento. Por fim, foi conduzida uma analise da sedimentação de elipsoides em fluido viscoplástico, na qual foram identificadas influencias de forma e que, para um elipsoide inclinado, o aumento do número de Bingham pode levar à constrição e até mesmo à inversão do sentido de rotação da partícula.

Palavras-chave: domínio sem fronteira. método da fronteira imersa. método lattice Boltzmann. sedimentação em meio viscoplástico. partícula elipsoidal.

ABSTRACT

ROMANUS, Rodrigo Saldanha. **Direct Numerical Simulation of Spheroidal Particle Settling in Viscoplastic Fluid Using Lattice Boltzmann Method**. 2020. 119 p. Dissertation (Master's Degree in Mechanical Engineering) – Federal University of Technology. Curitiba, 2020.

A numerical study of ellipsoidal particle settling in quiescent Newtonian and viscoplastic fluid is presented motivated by theoretical aspects and industrial applications, such as cuttings transport in oil drilling. As particle settling at moderate to high Reynolds numbers takes considerable distance to reach periodical or statistically steady regime, memory limitations in direct numerical simulations (DNS) constrain the maximum domain size for this class of flow. In spectral and finite difference methods, some workarounds that allow simulation in unbounded vertical extents are available, such as domain transferring schemes. Due to the locality in most of its algorithm, the lattice Boltzmann method (LBM) is increasingly popular for DNS studies. In present work, a boundary relocation approach is presented, enabling LBM simulations of particle motion in a virtually infinite domain. The scheme consists basically of the truncation of flow domain with the relocation of boundaries to nodes kept outside simulation confines. The immersed boundary method (IBM) is implemented for the liquid-fluid interaction. A thorough mesh generation for ellipsoidal particles is disclosed, as well as an extension of the internal mass compensation strategy of Suzuki and Inamuro (2011). The Bingham model is implemented with a proper adaptation of the boundary relocation approach. The numerical model is assessed sequentially for each of its features, showing good agreement with analytical solutions and results available in the literature. The possibility of improvement through an increase in resolution is also evidenced. Simulations were then performed for oblate spheroids in quiescent Newtonian fluid, in which a variety of motion patterns was delineated. Then, an investigation of ellipsoidal particles settling in viscoplastic fluid was conducted, analyzing shape influence on the motion of a solid-body. It was also shown that for an inclined ellipsoid, the increase of Bingham number leads to constriction and even an inversion in the direction of particle rotation.

Keywords: unbounded domain. immersed boundary method. lattice Boltzmann method. viscoplastic settling. ellipsoidal particle.

LIST OF FIGURES

LIST OF TABLES

LIST OF ACRONYMS

ACRONYMS

ALE	Arbitrary Lagrangian Eulerian
BGK	Bhatnagar, Gross and Krook
CFL	Courant-Friedrichs-Lewy
DNS	Direct Numerical Simulation
DLM	Distributed Lagrange Multiplier
FD	Fictitious Domain
GNF	Generalized Newtonian Fluid
GPU	Graphics Processing Unit
IBM	Immersed Boundary Method
LBGK	Lattice BGK Equation
LBM	Lattice Boltzmann Method
MLUPS	Million Lattice Updates per Second
NSE	Navier-Stokes Equations
SRT	Single Relaxation Time

LIST OF SYMBOLS

LATIN LETTERS

A	Ellipsoid semi-axis at x-direction	$[\mathrm{m}]$
A_s	Surface area	$[\mathrm{m}^2]$
B	Ellipsoid semi-axis at y-direction	$[\mathrm{m}]$
c	Lattice speed	$[\mathrm{m\,s}^{-1}]$
c_s	Speed of sound	$[\mathrm{m\,s}^{-1}]$
C	Ellipsoid semi-axis at z-direction	$[\mathrm{m}]$
d	Diameter of the spherical particle	$[\mathrm{m}]$
d_{z1}	Distance from the particle's centroid to the upwind boundary	$[\mathrm{m}]$
D_h	Discrete Dirac Delta	$[\mathrm{m}^{-3}]$
e	Internal energy density	$[\mathrm{J\,m}^{-3}]$
E	Elastic energy	$[\mathrm{J}]$
f	Particle distribution function	$[\mathrm{part\,s}^3\,\mathrm{m}^{-6}]$
f_i	Distribution population component in the i^{th} direction	$[\mathrm{part\,s}^3\,\mathrm{m}^{-6}]$
G	Elastic modulus	$[\mathrm{Pa}]$
h	Grid spacing	$[\mathrm{m}]$
H	Frustum height	$[\mathrm{m}]$
k	Boltzmann constant	$[\mathrm{Kg\,m}^2\,\mathrm{s}^{-2}\mathrm{K}^{-1}]$
l	Length	$[\mathrm{m}]$
L_1	Norm error	$[-]$
L_2	Quadratic norm error	$[-]$
m	Particle mass	$[\mathrm{kg}]$
m^*	Particle-fluid density ratio	$[-]$
M	Lagrangian surface mass density	$[\mathrm{kg\,m}^{-3}]$
n	Density of particles in mesoscopic analysis	$[\mathrm{part\,m}^{-3}]$
p	Pressure	$[\mathrm{Pa}]$
S_i	Source term in the i^{th} direction	$[\mathrm{part\,s}^3\,\mathrm{m}^{-6}]$
t	Time	$[\mathrm{s}]$
T	Temperature	$[\mathrm{K}]$
u	fluid velocity	$[\mathrm{m\,s}^{-1}]$
U	Solid-body velocity	$[\mathrm{m\,s}^{-1}]$
~~$\mathbf{V}$~~	Solid-body volume	$[\mathrm{m}^3]$
x,y,z	Cartesian coordinates	[m]
w_i	Weight function component in the i^{th} direction	$[-]$

GREEK LETTERS

γ	Adiabatic index	$[-]$
δ	Dirac Delta	$[\mathrm{m}^{-3}]$
δ_t	Time-step	$[\mathrm{s}]$
ϕ	One-dimensional discrete delta function	$[-]$

ρ	Density	$[\mathrm{kg\,m^{-3}}]$
∇	Nabla operator	$[-]$
∇^2	Laplacian operator	$[-]$
ν	Kinematic viscosity	$[\mathrm{m^2\,s^{-1}}]$
μ	Dynamic viscosity for Newtonian fluid	$[\mathrm{Pa\,s}]$
η	Apparent viscosity	$[\mathrm{Pa\,s}]$
Ω	Collision operator	$[\mathrm{kg\,s^2\,m^6}]$
ω	Collision frequency	$[\mathrm{s^{-1}}]$
τ	Relaxation time	$[\mathrm{s}]$

NON-DIMENSIONAL PARAMETERS

Ar	Archimedes number	$[-]$
Bi	Bingham number	$[-]$
Ga	Galileo number	$[-]$
Kn	Knudsen number	$[-]$
Ma	Mach number	$[-]$
Re	Reynolds number	$[-]$
C_D	Drag coefficient	$[-]$
C_S	Stokes drag coefficient	$[-]$
Y_g	Yield criterion	$[-]$

SUPERSCRIPTS

$(\,)_0$	Reference
$(\,)_b$	Boundary
$(\,)_c$	Centroid
$(\,)_I$	Reynolds above Stokes solution
$(\,)_p$	Particle
$(\,)_S$	Stokes solution as reference
$(\,)_T$	Terminal
$(\,)_y$	Yield
$(\,)_{\mathrm{calc}}$	Calculated
$(\,)_{\mathrm{conv}}$	Convective
$(\,)_{\mathrm{crit}}$	Critical
$(\,)_{\mathrm{eff}}$	Effective
$(\,)_{\mathrm{eq}}$	Equivalent
$(\,)_{\mathrm{interp}}$	Interpolated
$(\,)_{\mathrm{int}}$	Internal
$(\,)_{\mathrm{mfp}}$	Mean free-path
$(\,)_{\mathrm{num}}$	Numerical quantity from simulation
$(\,)_{\mathrm{ref}}$	Reference value – e.g., analytical solution
$(\,)_{\mathrm{sound}}$	Sound

$(\,)_{\text{wall}}$	Wall
$I_{(\,)}$	First tensor invariant
$II_{(\,)}$	Second tensor invariant
$III_{(\,)}$	Third tensor invariant

SUBSCRIPTS

$\bar{(\,)}$	In dimensionless lattice-units
$\dot{(\,)}$	Time-derivative
$(\,)^*$	Post-collision populations
$(\,)'$	Quaternion conjugate
$(\,)^T$	Transposed
$(\,)^{\text{reg}}$	Regularized
$(\,)^{\text{eq}}$	Equilibrium
$(\,)^{\text{neq}}$	Non-Equilibrium

VECTORS AND TENSORS

$2\mathbf{D}$	Shear rate tensor	$[\mathrm{s}^{-1}]$
$\mathbf{e}_i$	LBM velocity vector at i^{th} direction	$[-]$
$\mathbf{f}$	Lagrangian force density	$[\mathrm{N\,m}^{-3}]$
$\mathbf{F}$	Eulerian force density	$[\mathrm{N\,m}^{-3}]$
$\mathbf{F}_B$	Buoyant force	$[\mathrm{N}]$
$\mathbf{g}$	Gravity acceleration vector	$[\mathrm{m\,s}^{-2}]$
$\mathbf{I}$	Moment of inertia tensor	$[\mathrm{Kg\,m}^2]$
$\mathbf{L}$	Angular momentum	$[\mathrm{Kg\,m}^2\,\mathrm{s}^{-1}]$
$\mathbf{P}$	Linear momentum	$[\mathrm{Kg\,m\,s}^{-1}]$
$\mathbf{M}$	Moment of force	$[\mathrm{N\,m}]$
$\mathbf{n}$	Normal vector	$[-]$
$\mathbf{u}$	Velocity field vector	$[\mathrm{m\,s}^{-1}]$
$\mathbf{U}$	Solid-body velocity vector	$[\mathrm{m\,s}^{-1}]$
$\mathbf{v}$	Relative velocity vectors	$[\mathrm{m\,s}^{-1}]$
$\mathbf{x}$	Position vector in Eulerian grid	$[\mathrm{m}]$
$\mathbf{X}$	Position vector in Lagrangian mesh	$[\mathrm{m}]\ \mathrm{s}$
$\mathbf{\Pi}$	Second moment of distribution function	$[\mathrm{Pa}]$
$\boldsymbol{\sigma}$	Stress tensor	$[\mathrm{Pa}]$
$\boldsymbol{\tau}$	Viscous stress tensor	$[\mathrm{Pa}]$
$\boldsymbol{\delta}$	Kronecker delta tensor	$[-]$
$\boldsymbol{\xi}$	Mesoscopic velocity vector	$[\mathrm{m\,s}^{-1}]$
$\mathbf{\Omega}$	Solid-body angular velocity vector	$[\mathrm{rad\,s}^{-1}]$
$\boldsymbol{\gamma}$	Strain tensor	$[\mathrm{s}^{-1}]$

CONTENTS

1 INTRODUCTION

The underlying motivation of the present work arises from its application in the oil industry, in which the cuttings stemming from the drilling process must be kept suspended during an operational stop. Viscoplastic or yield-stress fluids are capable of holding rigid particles statically since they only flow when a certain stress value is exceeded. It must be noticed that the presence of solid particles can affect flow properties. Thereby mathematical modeling of fluid-structure interaction problems requires a multiphysics coupling between fluid dynamics and rigid body motion laws, leading to non-linear systems with no analytical solution.

1.1 CONTEXT AND MOTIVATION

The rotary drilling method was introduced at the beginning of the 20^{th} century by Anthony Lucas, showing how effective a rotating bit with continuous mud injection is. In this technique, a downward vertical force is applied to the drill bit while it rotates around its axis. This movement crushes the rock creating sediments that are transported to the surface by the drilling mud (NGUYEN, 1996). As depicted in Figure 1, there are two ways to perform the hole cleaning. In direct circulation, the fluid flows down, passing over the drill bit and returning through the annular region. Whereas in reverse circulation, the drilling mud travels oppositely, flowing down over the annular region and returning through the drill pipe.

Figure 1 – Example of direct (a) and reverse (b) circulation in rotary drilling. The fluid returning from well bore carries the cuttings that will be filtered off as drilling fluid is pumped back to the well bore.

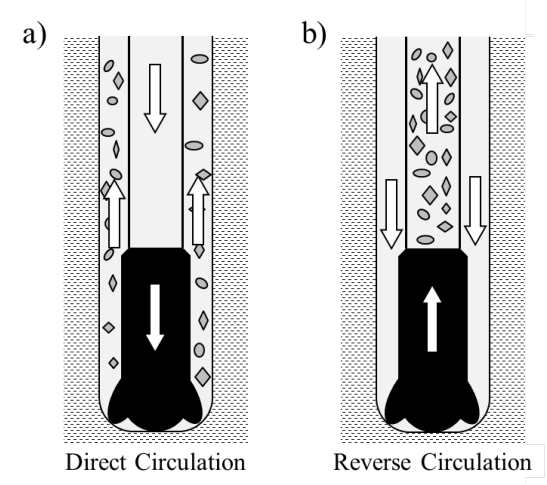

Source: Own elaboration.

In the oil industry, drilling muds are non-Newtonian fluids that can perform numerous roles, such as, cooling the drill bit; lessening drill pipe friction; providing geological information; consolidating the well bore wall; hindering influx of fluids and gas into the well bore; transporting the cuttings and suspending them during drill stop (NGUYEN, 1996). The drilling fluid is usually a colloidal dispersion, in which a solid is dispersed in a liquid; or an emulsion, attained by spreading different liquids (OMLAND, 2009). Such complex materials are best described as thixo-elasto-viscoplastic, that is, it presents elastic, viscoplastic and time-dependent behavior (EWOLDT; MCKINLEY, 2017).

During drilling, the cuttings are carried by the circulating fluid. However for some processes, like well bore cementation, an operational stop is necessary. That way, the drilling mud stops circulating and cuttings begin to settle. To avoid imprisonment of the drill bit, the drilling fluids are designed to assume a gel state when they are not under shear. As this behavior is presented by viscoplastic fluids, this project was designed to put forward a reliable yet computationally efficient algorithm for the fully-resolved simulation of particle motion in viscoplastic fluid by describing the flow evolution with lattice Boltzmann method (LBM).

1.2 LITERATURE REVIEW

This section brings a review of the pertinent literature on single-particle settling, starting with the earlier analytical developments of a sphere moving in Newtonian fluid at creeping flow regime, proceeding with the numerical developments and experimental findings such as, the diversified motion patterns observed at intermediate Reynolds numbers, and concluding with relevant studies of rigid body motion in viscoplastic fluid.

1.2.1 Early Studies

The interest in the behavior of flows with particles drove a considerable scientific effort over the years. Stokes (1851) made a substantial contribution by calculating the steady-state creeping flow ($\mathrm{Re} < 0.01$) around a sphere undergoing uniform translation. He also postulated that at creeping flow, there is no non-trivial steady state solution for the Newtonian flow past an infinitely long cylinder, which became known as Stokes paradox. Addressing the same phenomenon, Whitehead (1889) proposed an iterative procedure, using low-order approximations to calculate inertial terms. However, this scheme was not able to satisfy the boundary conditions

at the infinity. Both Stokes and Whitehead's issues were successfully solved by Oseen (1910) when he observed that if the velocity field is spatially invariant at the infinity, then friction is negligible, and inertia holds the strongest influence on the flow dynamics. With a perturbation method that partially included convective acceleration, Oseen (1913) developed an expression of the sphere drag coefficient. Oseen's study inspired several relevant works (GOLDSTEIN, 1929; TOMOTIKA; AOI, 1950; STEWARTSON, 1956), and his expression for the drag coefficient was validated by Maxworthy (1965) to produce accurate results up to $\mathrm{Re} = 0.45$. Higher-order approximations were obtained by Proudman and Pearson (1957) with the method of asymptotic expansions. Despite all development achieved over the years, analytical solutions for particle settling still cannot be attained for solids of complex geometries or for intermediate to high Reynolds number.

1.2.2 Motion Patterns at Intermediate Reynolds

Though axial symmetry may be expected for the ideal situation of uniform flow past a stationary sphere, for $\mathrm{Re} \geq 203$ (CHRUST *et al.*, 2013b), the resulting downstream wake can be fully three-dimensional and capable of admitting complex vortical structures, as registered by Magarvey and MacLatchy (1965) in an excellent series of photographs showing the characteristic structure of the wakes behind a sphere for Reynolds numbers extending from 200 to 500. An illustration of the vortex loops for $300 < \mathrm{Re} < 420$ is shown in Figure 2.

Figure 2 – Upper and side views of vortex loops in the downstream wake of flow over a stationary sphere for $300 < \mathrm{Re} < 420$.

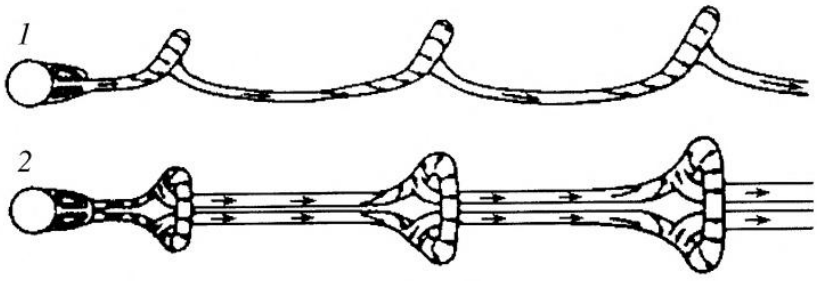

Source: Gushchin and Matyushin (2006)

For the gravity-driven motion of a sphere, the onset of wake instabilities causes the particle to travel oscillatory or chaotic paths. In their study, Horowitz and Williamson (2010) performed particle settling investigations at terminal Reynolds numbers ranging from an order of 10^2 to 10^4. They used spheres with the diameter d varying between 0.2 and 3.8 cm, moving in two

large containers of dimensions 0.4×0.4×1.5 m and 0.2×0.2×0.9 m. Among many observations, they registered that the sphere traveled a zigzaggy path when the particle-fluid density ratio ($m^* = \rho_p/\rho$) was lower than 0.36 and the terminal Reynolds number higher than 260. To minimize wall effects and approximate an unbounded domain situation, they designed tanks with sizes much larger than particle's diameter. This level of particle-tank scale ratio is highly challenging to reproduce in DNS, especially for three-dimensional cases. Ardekani *et al.* (2016) studied the settling of prolate and oblate spheroids using 480×480×4000 grid nodes (almost 1 billion) and were able to represent a rather small tank, of dimensions $15d \times 15d \times 125d$. Such a high amount of grid nodes can produce overwhelming computational cost.

1.2.3 Fluid-Structure Interaction

In numerical methods, the no-slip boundary condition around an immersed object can be achieved by either body-conformal or fixed grid techniques. Despite the good accuracy that is provided by body-conformal methods, their implementation can be rather cumbersome, especially in problems with moving particles, where the necessity to rebuild the computational grid at each time step is a major computational bottleneck. Hence, many resorts to fixed grid methods, such as distributed Lagrange multiplier/fictitious domain (DLM/FD) and immersed boundary (IBM) methods.

The DLM/FD was initially introduced by Glowinski *et al.* (1994) for stationary rigid bodies and later extended for moving particles (GLOWINSKI *et al.*, 2000). In this methodology, a geometrically complex domain is embedded in a larger simple-shaped domain, and the interaction between fluid and solid-body is modeled through variational principles. It results in a weak formulation for fluid-particle motion, with rigidity constraint enforced using distributed Lagrange multiplier. IBM was developed by Peskin (1972) to study flow patterns around heart valves and evolved to a handy tool for studying fluid-structure interaction problems. This methodology uses an interpolative scheme in which a Lagrangian mesh delineates particle's surface and the given, or calculated, boundary condition is assured with the distribution of force terms in the Eulerian domain. For a more meticulous analysis of body conformal and fixed grid schemes, the reader may refer to (HAERI; SHRIMPTON, 2012).

In 1994, Ladd pioneered the studies of liquid-solid flows with LBM (LADD, 1994a; LADD, 1994b) and since then, many strategies have been employed for LBM simulations of fluid-structure interaction problems. Bouzidi *et al.* (2001) proposed the second-order accurate

interpolated bounce-back approach for curved boundaries and, Lallemand and Luo (2003) extended the method to simulate moving boundaries. As the LBM approach is based on Cartesian grids, it is convenient to use fixed grid techniques. The implementation of LBM with DLM/FD and IBM was introduced by Shi and Phan-Thien (2005) and Feng and Michaelides (2009), respectively.

1.2.4 Infinite Domain Approximations

As previously mentioned, it is not a trivial task to numerically represent particle settling in an unbounded domain. Jenny and Dušek (2004) proposed an implicit scheme of spectral Fourier decomposition in the azimuthal direction and performed DNS of falling and ascending spherical particles (JENNY *et al.*, 2004). They designed a vertical cylindrical domain translating with the sphere. The cylinder's depth was of $37d$ and radius of $8d$. Jenny and Dušek (2004) found a variety of motion patterns, such as vertical, oblique, zigzaggy, time-periodic oscillatory, helical and chaotic, by varying the particle-fluid density and the Galileo number, calculated by:

$$\mathrm{Ga} = \frac{\sqrt{|m^* - 1|\, g d^3}}{\nu}, \tag{1}$$

in which, g is the gravitational acceleration and ν is the kinematic viscosity for a Newtonian fluid. The Galileo number (or alternatively the Archimedes number $\mathrm{Ar} = \mathrm{Ga}^2$) measures the ratio between gravitational and viscous forces acting on the immersed particle and it determines the terminal velocity that the solid-body will reach. In more recent work, Zhou and Dušek (2015) extended and improved the parametric study from (JENNY; DUŠEK, 2004) assessing the different modes of falling and ascending spheres. Zhou *et al.* (2017) used basically the same approach and added decomposition of the cylindrical vertical domain into a spherical subdomain rotating with the solid-body. By doing so, they investigated some motion regimes from oblate spheroids settling in quiescent fluid. Huang *et al.* (2014) employed a superposition of fine and coarse grids in LBM and studied the behavior of an ellipsoidal particle under action of gravity. Their results agreed well with arbitrary-Lagrangian-Eulerian (ALE) simulations from Swaminathan *et al.* (2006). The domain strategy they implemented consisted of a fine grid traveling with the particle, with its top and bottom layers being added or removed from the coarser grid. Their coupling between grids was essentially identical to the multi-block scheme (FILIPPOVA; HÄNEL, 1998). This strategy resulted in a very long yet finite tube.

In a DLM/FD study, Yu *et al.* (2002) approximated the case of a sphere settling in an infinitely long channel by transferring the simulation domain vertically following the particle. Rahmani and Wachs (2014) produced results for spherical and angular particles with a stretched $192\times192\times248$ mesh with a length-width ratio around 3. They followed the same domain transferring approach but adopted lateral periodicity. Good agreement with experimental drag coefficient data from Haider and Levenspiel (1989) was achieved. Mougin and Magnaudet (2002) demonstrated how the generalized Kirchhoff equations allow solving the velocity field from the disturbance flow produced by a moving body in infinite viscous media. Auguste and Magnaudet (2018) employed this procedure using spherical grids of 94 and 86 cells in the radial direction, 64 in polar, and 128 in azimuthal. They examined the path oscillations of spheres rising in quiescent fluid. The same technique with a cylindrical domain was adopted by Shenoy and Kleinstreuer (2010), in an investigation of the influence of the aspect ratio of a circular disk settling dynamics, and by Auguste *et al.* (2013) that performed several simulations for thin disks, producing a phase diagram of trajectory regimes. Their computational grid was $20d$ long with $100\times80\times32$ grid nodes, and their results yielded a reasonable qualitative agreement with spectral Fourier decomposition from Chrust *et al.* (2013a). While there are alternatives for DNS of particle motion in infinite media by spectral or finite element methods, no LB scheme for unbounded domain fully-resolved simulation has been provided in the literature up to this date.

1.2.5 Particle Motion in Yield-Stress Fluid

Yield-stress fluids are those with a viscoplastic behavior, they flow only if their yield-stress σ_y is surpassed, otherwise, they act as a plastic material. A dimensionless parameter commonly used to characterize viscoplastic flows is the Bingham number, which gives the ratio between yield and viscous stresses, for a single-particle flow:

$$\mathrm{Bi} = \frac{\sigma_y l}{\eta_0 u_0}, \tag{2}$$

where η_0 is fluid's plastic viscosity, u_0 the reference velocity, which for particle motion problems is usually the solid-body terminal velocity, and l the reference length of the flow.

Volarovich and Gutkin (1953) presented the earliest investigations of particle motion in this category of fluid, in which they found that the particle will move within a bounded subset, considering that sufficiently far from particle stress falls below σ_y. The yielded fluid

region was envisioned as a 'sphere of influence' by Andres (1960). In meantime, Boardman and Whitmore (1960) performed experiments with a cube falling in yield-stress fluid and, by changing solid-body orientation and measuring limiting forces, verifying that the stress does not act uniformly at the object's surface. As an answer to Boardman and Whitmore (1960) study, Rae (1962) proposed assertively that there would be unsheared material adhering to certain portions of the particle's surface, stagnant zones. In experimental research, Valentik and Whitmore (1965) measured the terminal velocity of a sphere falling in viscoplastic fluid and tried to establish an expression for the drag force. Ansley and Smith (1967) borrowed concepts from the slip-line field theory, whose fundamentals can be found in "The mathematical theory of plasticity" by Hill (1998). Though their postulated shape of a torus centered at sphere equator for the yielded region was not accurate, they revealed the usefulness of plasticity theory when analyzing this kind of problem and proposed an drag coefficient expression as a function of a dynamical dimensionless parameter Q.

Using flow visualization techniques, Brookes and Whitmore (1969) confirmed stagnant zones for cylinder, plate, and wedge-shaped particles moving in yield-stress fluid. Adachi and Yoshioka developed a variational scheme to calculate lower and upper-bounds of drag force for creeping viscoplastic flow past spherical (YOSHIOKA *et al.*, 1971) and 2D cylindrical (ADACHI; YOSHIOKA, 1973) particles. Their flow profile was later proven to be different from the actual solution, that was uncovered in finite-element numerical work from Beris *et al.* (1985), which extended the plastic boundary-layer analysis from Oldroyd (1947) to an axisymmetric flow around the sphere. The evolution of predictions for the unsheared region that moves along with a spherical particle settling in viscoplastic fluid is shown in Figure 3.

Figure 3 – Shape of the sheared envelope surrounding a sphere in creeping motion in viscoplastic fluids: (a) Ansley and Smith (1967); (b) Yoshioka *et al.* (1971); (c) Beris *et al.* (1985).

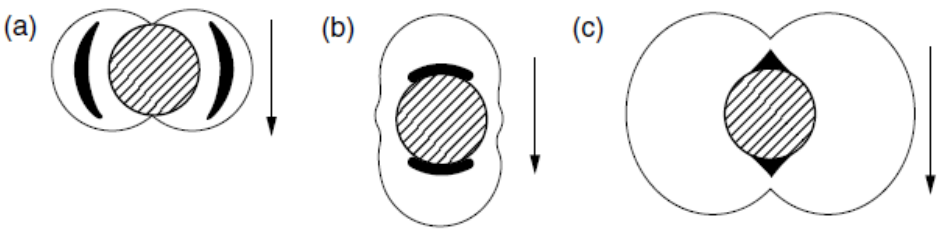

Source: Adapted from Chhabra (2006)

In their study, Beris *et al.* (1985) calculated the critical limit Y_{crit} of a yield-stress dimensionless parameter Y_g, formed from the ratio of yield-stress to external forces. A particle

left from rest will move only if $Y_g < Y_{\text{crit}}$, otherwise it will be kept suspended. Atapattu *et al.* (1990) experimentally investigated wall effects for spheres falling slowly under gravity in a tube filled viscoplastic fluid and, by varying the sphere-to-tube diameter ratio d/D, they verified the existence of a critical value $(d/D)_{\text{crit}}$, correlated to Y_g, to which no wall effect is discernible. In a later publication, Atapattu *et al.* (1995) verified that at a fixed confinement ratio, a higher Bingham number increases drag exerted on particle. The wall effect on the creeping motion of a sphere moving inside tubes filled with viscoplastic fluid was also investigated in the numerical study from Blackery and Mitsoulis (1997), with the fluid represented by the Bingham constitutive equation with Papanastasiou (1987) modification. By analyzing the geometry from the yielded zone, they verified that tight gaps tend to press and deform the yielded region.

Jossic and Magnin (2001) covered a subject that was explored very little on experimental grounds until then, estimating the drag coefficient of sphere, disk, cylinder, cube, and cone-shape particles in non-thixotropic viscoplastic fluids at a very low velocity quasi-static domain. Using carefully prepared aqueous solutions of Carbopol ETD 2050, Tabuteau *et al.* (2007) calculated the drag coefficient for a spherical particle, obtaining results that agreed well with theoretical predictions from Beaulne and Mitsoulis (1997). Putz *et al.* (2008) experimentally investigated the flow fields around a spherical object falling freely in a viscoplastic fluid for $\text{Re} < 1$. Numerical studies from Wachs and Frigaard (2016) and Chaparian and Frigaard (2017a) analyzed the influence of the particle geometry on the sheared region and the yield parameter Y_{crit} for a 2D configuration (CHAPARIAN; FRIGAARD, 2017b).

1.2.6 Gaps and Open Issues

Despite the aforementioned development, several knowledge gaps persist when it comes to the sedimentation of particles in viscoplastic fluids, for experimental results still have not covered a very extensive range of parameters and most of the existent numerical studies are limited to steady-state 2D cases and spherical particles. One issue from the Bingham constitutive equation is that its discontinuity causes the numerical implementation to be rather cumbersome. As a consequence, many opt to use regularized models (LIU *et al.*, 2002; FRIGAARD; NOUAR, 2005; TOKPAVI *et al.*, 2008), such as Papanastasiou's, which are not fit for representing a perfect plasticity below yield-stress.

These limitations, reduce the range of analyses available for the motion of a solid-body in yield-stress fluids. In addition to require up-dated methods of analysis, we think that the study

of viscoplastic settling of particles with arbitrary shapes or, at least, with aspect ratios different from 1 is of great scientific interest.

1.3 OBJECTIVES AND DOCUMENT OUTLINE

Present work addresses the three-dimensional study of a ellipsoidal particle settling in Newtonian and Bingham fluids. The numerical formulation combines lattice Boltzmann and immersed boundary methods in an IB-LBM scheme. This approach fully describes the transient phenomenon of a solid-body settling from a rest position. The general objective was partitioned in sequential steps that served as milestones for the project execution, those were:

i) Implementation of LBM for a 3D Newtonian flow, verified for a Poiseuille flow in rectangular cross-section channel;

ii) Implementation of IBM for an ellipsoidal particle, verified by a series of simulations including the uniform flow over a stationary sphere, a particle settling in a closed tank, and an ellipsoid centered in a Couette flow;

iii) Development of a viable approximation for particle motion in an unbounded domain, which is verified for a Stokes flow and experimental data of a sphere ascending at a Galileo number of 173;

iv) Extension of LBM to the simulation of a Bingham fluid, initially validated for a Poiseuille flow between parallel plates and then for a creeping flow sphere settling in viscoplastic fluid.

iv) Simulations of an oblate spheroid settling in Newtonian fluid, with Galileo numbers ranging from 100 to 250, delineating the variety of presented motion patterns.

v) Investigation of shape influences on the dynamics of an ellipsoidal particle settling in viscoplastic fluid for Bingham and Reynolds numbers ranging from 0 to 400 and 0.1 to 100, respectively.

This work is divided in six chapters. Chapter 2 provides the fundamentals of IBM and LBM, including some insights for its application in non-Newtonian flows. Chapter 3 details the numerical methodology developed throughout the study. Verification with analytical solutions and literature data is presented in Chapter 4. Simulations of oblate spheroids at intermediate and

high Reynolds numbers in Newtonian fluid and analyses of shape and orientation influence in viscoplastic settling are presented in Chapter 5. Finally, a summary of the conducted work, the conclusions drawn and recommendations for future research are given in Chapter 6.

2 THEORETICAL BACKGROUND

This chapter overviews fundamental concepts from the methods used as the basis on the formulation of a numerical model, detailed in Chapter 3. Section 2.1 covers the ideas behind the immersed boundary method (IBM). Section 2.5 brings a brief discussion of flow representation at microscopic, mesoscopic and macroscopic scales. Section 2.3 proceeds with the Kinetic Theory overview, followed by a comprehensive review of the lattice Boltzmann method (LBM) with external force term in Section 2.4. The correlation between macroscopic and mesoscopic variables through Chapman-Enskog expansion is examined in Section 2.5 and implementation of LBM for generalized Newtonian fluids (GNF) is briefly discussed in Section 2.6.

2.1 IMMERSED BOUNDARY METHOD

The immersed boundary method was developed by Peskin (1972) to study flow patterns around heart valves, later evolving into a very useful tool for fluid-structure interaction problems. Its formulation comes from the consideration of an elastic incompressible solid filling a three-dimensional space. IBM uses a Lagrangian approach to track the set of elastic fibers whose position is $\boldsymbol{X}\,(q,r,s,t)$, and describes the fluid domain with velocity field $\boldsymbol{u}$ in an Eulerian fashion (PESKIN, 2002).

Let (q,r,s) be the curvilinear coordinates attached to the surface of material and $\boldsymbol{X}\,(q,r,s,t)$, the position vector in Cartesian coordinates of the material point whose label is (q,r,s) at time t. By assuming that all part of elastic material immersed in fluid is confined in a surface, only two Lagrangian parameters (r,s) will be required to its description, as illustrated by Figure 4, in which M represents the Lagrangian surface mass density and the integral of ρ over any finite volume is the sum of fluid and elastic boundary masses contained within that volume.

For this description, the no-slip boundary condition at a solid-body surface is written as:

$$\frac{\partial \boldsymbol{X}}{\partial t}\,(r,s,t) = \boldsymbol{u}\,(\boldsymbol{X}\,(r,s,t)\,,t)\,. \tag{3}$$

The Lagrangian points from elastic boundary create a discontinuity in the Eulerian domain. Being $\boldsymbol{x}$ the position vector and $\delta\,(\boldsymbol{x})$ the three-dimensional Dirac delta, Equation 3 can

Figure 4 – Example of immersed boundary method description for a solid-body described by its external surface. The mass of a d~~V~~ element is the summation of fluid and elastic boundary masses inside this volume.

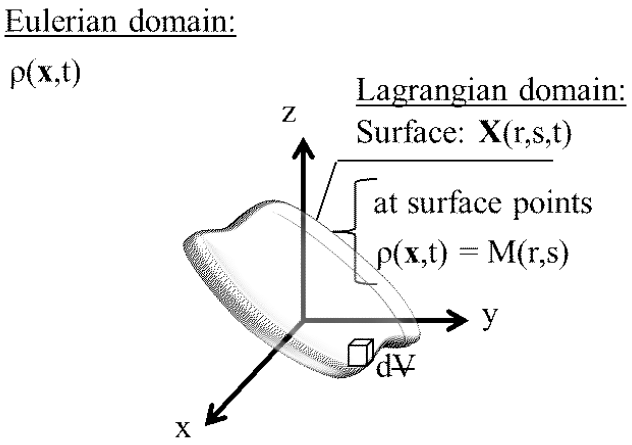

Source: Own elaboration.

be rewritten in terms of an integral over the Eulerian domain with $\boldsymbol{u}$ multiplied by $\delta\left(\boldsymbol{x}-\boldsymbol{X}\right)$:

$$\frac{\partial \boldsymbol{X}}{\partial t}=\int \boldsymbol{u}(\boldsymbol{x},t)\delta(\boldsymbol{x}-\boldsymbol{X}(r,s,t))\mathrm{d}\boldsymbol{x}. \tag{4}$$

In Equation 4, the Dirac delta is the singular pulse function that expresses the discontinuity at $\boldsymbol{x}=\boldsymbol{X}$, in an analogous manner but integrating over a Lagrangian domain, the force and mass densities are written as (PESKIN, 2002):

$$\rho(\boldsymbol{x},t)=\int M(r,s)\delta(\boldsymbol{x}-\boldsymbol{X}(r,s,t))\mathrm{d}r\mathrm{d}s; \tag{5a}$$

$$\boldsymbol{f}(\boldsymbol{x},t)=\int \boldsymbol{F}(r,s,t)\delta(\boldsymbol{x}-\boldsymbol{X}(r,s,t))\mathrm{d}r\mathrm{d}s. \tag{5b}$$

Here, $\boldsymbol{F}(r,s,t)$ and $\boldsymbol{f}(\boldsymbol{x},t)$ are the Lagrangian and Eulerian densities of elastic force, respectively. Equation 5b assures that $\boldsymbol{f}(\boldsymbol{x},t)$ is zero at all space points lying in fluid regions at time t and that the integral of $\boldsymbol{f}(\boldsymbol{x},t)$ over a finite volume is the total force applied to the fluid by the part of the immersed boundary contained within this volume. It should be noticed that, despite delta $\delta(\boldsymbol{x})$ being three-dimensional, there are only two integrals $\mathrm{d}r\mathrm{d}s$. As a result, $\rho(\boldsymbol{x},t)$ and $f(\boldsymbol{x},t)$ are each singulars like a one-dimensional delta function, with this singularity being supported on the immersed elastic boundary. However, their integrals will be finite over any limited volume, since Dirac delta works as a pulse function (PESKIN, 2002).

The function $\boldsymbol{F}(r,s,t)$ arises from an assumed perturbation $\delta\boldsymbol{X}$ at the Lagrangian domain configuration $\boldsymbol{X}$ and, using the principle of virtual work, is given by the Fréchet derivative of the elastic energy E evaluated at configuration $\boldsymbol{X}$ (PESKIN, 2002):

$$\boldsymbol{F} = -\frac{\delta E}{\delta \boldsymbol{X}}, \tag{6}$$

which is the derivative of a single-variable function to a vector, if $\boldsymbol{X} = (X_1,X_2,X_2)$:

$$\boldsymbol{F} = -\left(\frac{\delta E}{\delta X_1},\frac{\delta E}{\delta X_2},\frac{\delta E}{\delta X_3}\right), \tag{7}$$

where δ represents a virtual infinitesimal variation and is used to represent a derivative.

By extending those concepts to a numerical scheme, the IBM originates from a spatial and temporal discretization of fluid-structure equations. A discrete form of the Dirac delta function D_h, whose development comes from identities satisfied by the spatially discretized scheme, is also necessary (PESKIN, 2002).

The spatial discretization of IBM employs two independent mesh and grid, one for the Lagrangian and other for the Eulerian variables. The Eulerian grid, denoted E_h, is uniform with a distance h between nodes, the Lagrangian mesh, denoted L_h is the set (q,r,s) of form $(k_q\Delta q,k_r\Delta r,k_s\Delta s)$, where $\boldsymbol{k} = (k_q,k_r,k_s)$ has integer components. Figure 5 illustrates IBM applied for a stationary boundary also exemplifying a no-slip condition described in this scheme.

Figure 5 – Example of a discretized IBM scheme with a static particle, in which velocity field is modeled through force terms and velocity at the boundary is assumed as the interpolation of near Eulerian nodes.

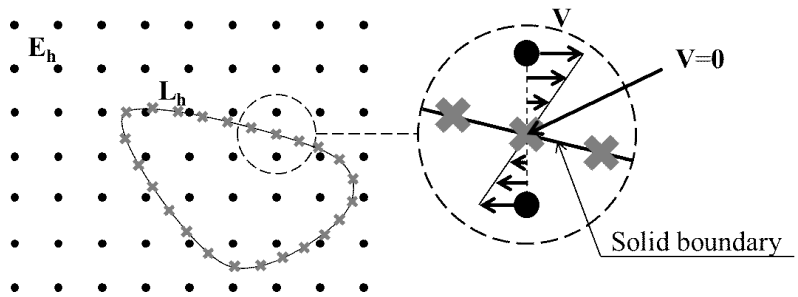

Source: Own elaboration.

The velocity at each Lagrangian node is obtained from interpolation of velocity field $\boldsymbol{u}\,(\boldsymbol{x},t)$ from nearest Eulerian locations, this domain transference can be written by a discrete form of Equation 4 as (PESKIN, 2002):

$$\frac{\mathrm{d}\boldsymbol{X}(q,r,s,t)}{\mathrm{d}t} = \sum_{\boldsymbol{x}\in E_h} \boldsymbol{u}(\boldsymbol{x},t)D_h(\boldsymbol{x} - \boldsymbol{X}(q,r,s,t))h^3, \tag{8}$$

in which D_h works as weighting function and can be seen as a discrete equivalent of the three-dimensional Dirac delta that is assumed as being a product of one-variable functions scaling with mesh-width h hence (PESKIN, 2002):

$$D_h(\boldsymbol{y}) = \frac{1}{h^3}\phi\left(\frac{y_1}{h}\right)\phi\left(\frac{y_2}{h}\right)\phi\left(\frac{y_3}{h}\right), \tag{9}$$

where y_1, y_2, and y_3 are the components of a three-dimensional $\boldsymbol{y}$ vector and ϕ is the one-dimensional discrete delta function. An in-depth analysis of different functional forms for ϕ can be found in (YANG *et al.*, 2009). The four-point piecewise version of this function is given by:

$$\phi(r) = \begin{cases} \frac{1}{8}\left(3 - 2|r| + \sqrt{1 + 4|r| - 4|r|^2}\right) & , 0 \leq |r| \leq 1; \\ \frac{1}{8}\left(5 - 2|r| - \sqrt{-7 + 12|r| - 4|r|^2}\right) & , 1 \leq |r| \leq 2; \\ 0 & , |r| \geq 2. \end{cases} \tag{10}$$

This function is developed under a sequence of postulates meant to assure that $D_h \to \delta$ as $h \to 0$. In its definition, the continuous Dirac delta function is zero everywhere except at $\delta(0)$ and the integral of $\delta(x)$ over the entire real line equals one, this results in the following properties

$$\int_{-\infty}^{\infty} \delta(x)\mathrm{d}x = 1; \tag{11a}$$

$$\int_{-\infty}^{\infty} x\delta(x)\mathrm{d}x = 0. \tag{11b}$$

At Equation 11b, by multiplying $\delta(x)$ by its argument, the integral over entire real line becomes zero. Similarly, the summation of discrete Dirac delta over the entire Eulerian domain must equal one and the summation of D_h multiplied by its argument has to be zero thus (PESKIN, 2002):

$$\sum_{\boldsymbol{x}\in E_h} D_h(\boldsymbol{x} - \boldsymbol{X})h^3 = 1; \tag{12a}$$

$$\sum_{\boldsymbol{x}\in E_h} (\boldsymbol{x} - \boldsymbol{X})D_h(\boldsymbol{x} - \boldsymbol{X})h^3 = 0. \tag{12b}$$

A thorough description of ϕ formulation are outside the scope of present work and can be found in (PESKIN, 2002). By substituting D_h at fluid-structure equations (Equations 5b and

5a) and replacing the integrals by finite sums, as done for the velocity equation, the discrete fluid-structure equations are:

$$\rho(\boldsymbol{x},t) = \sum_{(q,r,s)\in L_h} M(q,r,s) D_h(\boldsymbol{x} - \boldsymbol{X}(q,r,s,t))\Delta q \Delta r \Delta s; \tag{13a}$$

$$\boldsymbol{f}(\boldsymbol{x},t) = \sum_{(q,r,s)\in L_h} \boldsymbol{F}(q,r,s,t) D_h(\boldsymbol{x} - \boldsymbol{X}(q,r,s,t))\Delta q \Delta r \Delta s. \tag{13b}$$

In practice, Equations 13a and 13b spread Lagrangian variables into the Eulerian domain while the operation in Equation 8 is best described as an interpolation, since it averages the Eulerian velocities into a Lagrangian material point (PESKIN, 2002). The discrete Dirac delta D_h works as a pulse function, whose weight is valued by the proximity between Eulerian and Lagrangian points $|\boldsymbol{x} - \boldsymbol{X}(q,r,s,t)|$.

If the points from L_h are too spaced in comparison to E_h, there will be discrete points from Eulerian mesh "passing through" immersed boundary. Peskin (2002) estabilished the following restrictions to avoid leaks:

$$|\boldsymbol{X}(q+\Delta q,r,s,t) - \boldsymbol{X}(q,r,s,t)| < \frac{h}{2}; \tag{14a}$$

$$|\boldsymbol{X}(q,r+\Delta r,s,t) - \boldsymbol{X}(q,r,s,t)| < \frac{h}{2}; \tag{14b}$$

$$|\boldsymbol{X}(q,r,s+\Delta s,t) - \boldsymbol{X}(q,r,s,t)| < \frac{h}{2}. \tag{14c}$$

However, Pinelli *et al.* (2010) showed an increase of interpolation error as the distance between Lagrangian markers become smaller than Eulerian mesh spacing, with optimal values for a distancing of approximately h.

2.2 RELEVANT SCALES

Before engaging in the equations of lattice Boltzmann method (LBM), a topic of relevant scales seems worth discussing. When analyzed on a microscopic scale, fluids are composed of molecules in constant motion undergoing collision with each other (KUNDU *et al.*, 2012). However, usual mathematical descriptions of fluid dynamics rely on the concept of continuum, an idealization in which fluids have a continuous distribution of mass, without gaps.

The continuum assumption operates at time and length scales sufficiently large such that the atomistic picture of the fluid can be taken out (GREENKORN, 2018) and properties, like density or velocity, are given for fixed places in space. A microscopic scale works at length scales of the mean free path of fluid atom or molecule l_{mfp} and, as it tracks individual particles and all their degrees of freedom, flow simulations described in the microscopic scale are computationally expensive.

An alternative lying in-between these two descriptions is the mesoscale, in which clusters of molecules are represented by a probabilistic distribution. Figure 6 presents a hierarchy schematic of the mentioned length scales.

Figure 6 – Hierarchy of length and time scales in fluid dynamics problems.

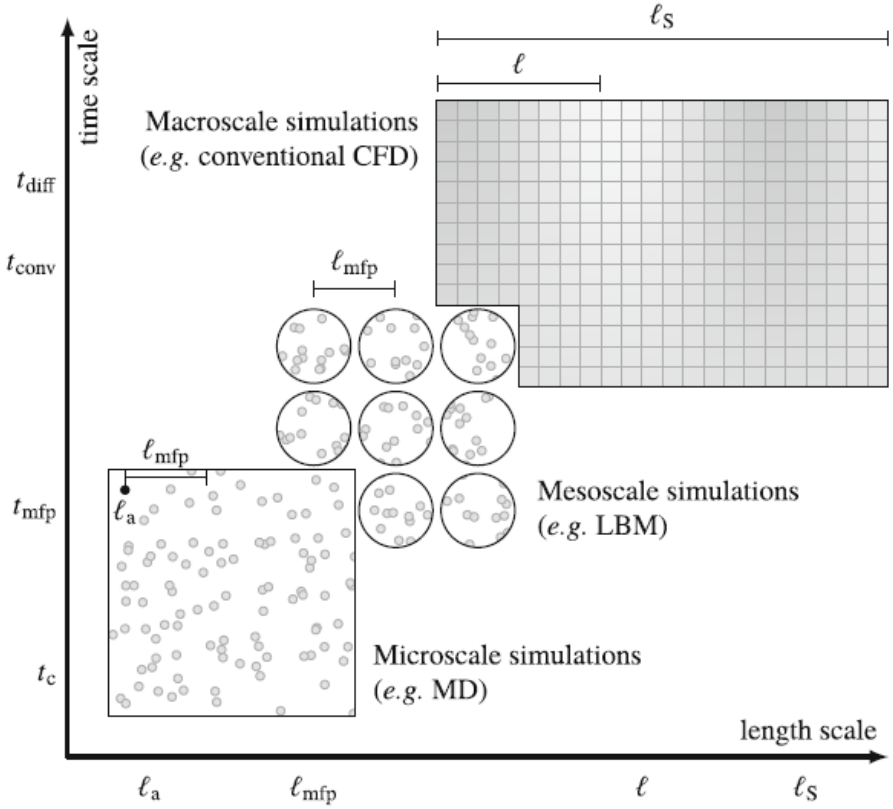

Source: Krüger *et al.* (2017).

The ratio of the mean free path l_{mfp} to the representative physical length scale l, is known as Knudsen number ($\text{Kn} = l_{\text{mfp}}/l$) which is helpful on delineating whether a microscopic treatment of the phenomenon is necessary or not (KRÜGER *et al.*, 2017). If l_{mfp} is sufficiently large in comparison to l, collisions occur very rarely between particles and they move independently of each other, thus, the flow requires a microscopic treatment. The transition between flow regimes for different Kn is (HALWIDL, 2016):

- Kn > 1 – Molecular flow;
- $0.01 <$ Kn < 1 – Transition flow;
- Kn ≤ 0.01 – Macroscopic flow.

The Mach number Ma defines the ratio of acoustic to advective time scales (KRÜGER *et al.*, 2017), determining how fast pressure waves propagate through the fluid and providing a good measurement whether or not a flow can be treated as incompressible. This dimensionless parameter is given by:

$$\text{Ma} = \frac{t_{\text{sound}}}{t_{\text{conv}}} = \frac{u_0}{c_s}, \tag{15}$$

where c_s is the speed of sound, which for an ideal gas is given by (JEANS, 1940):

$$c_s = \sqrt{\gamma \frac{kT}{m}}, \tag{16}$$

in which, T is the temperature in Kelvin, m is the particle mass, γ the adiabatic index, whose value varies from 1.3 to 1.67, and k is the Boltzmann constant ($k = 1.3 \times 10^{23}$J K^{-1}), a proportionality factor that relates a gas average relative kinetic energy with its thermodynamic temperature (FEYNMAN, 1970). In practice, a flow can be assumed as incompressible when Ma ≤ 0.1 (BALACHANDRAN, 2006). Dividing the Mach number by Reynolds number Re $= \rho u_0 l/\mu$

$$\frac{\text{Ma}}{\text{Re}} = \frac{u_0/c_s}{\rho u_0 l/\mu} = \frac{\mu}{\rho l}\sqrt{\frac{m}{\gamma kT}}, \tag{17}$$

and given that for an ideal gas, the mean free path l_{mfp} is given by (DAI *et al.*, 2017)

$$l_{\text{mfp}} = \frac{\mu}{\rho}\sqrt{\frac{\pi m}{2kT}}, \tag{18}$$

the multiplication of Eq 17 by $\sqrt{\gamma\pi/2}$ yields the Knudsen number Kn, hence the Reynolds, Mach and Knudsen numbers are related by:

$$\text{Kn} = \frac{\text{Ma}}{\text{Re}}\sqrt{\frac{\gamma\pi}{2}}, \tag{19}$$

which is known as *von Kármán relation* (WEISSTEIN, 2009).

2.3 KINETIC THEORY

The mesoscopic kinetic theory is the cornerstone of LBM and describes gas media as a distribution of particles, evolving on timescales about the mean collision time t_{mfp} (MOHAMAD, 2011). In 1872, Boltzmann published a long memoir named "Further Investigations on the Thermal Equilibrium of Gas Molecules", in which he poses that: "whatever the state of the gas have may be initially, it must always approach the limiting distribution found by Maxwell" (BOLTZMANN, 1872). Based on what he called "exact consideration of the collision process", Boltzmann provided a fundamental basis for further developments in kinetic theory.

The particle distribution function f, a fundamental variable in kinetic theory and LBM, can be seen as a generalization of density ρ, which also takes the microscopic particle velocity into account. Thus, instead of a deterministic approach, where $\rho(\boldsymbol{x},t)$ represents the density of particles in position $\boldsymbol{x}$ at time t, the fluid flow is described in a probabilistic fashion. The distribution function $f(\boldsymbol{x},\boldsymbol{\xi},t)$ can be seen as the expected number of particles to be found at position coordinates in each small volume element $(\boldsymbol{x},\boldsymbol{x}+\mathrm{d}\boldsymbol{x})$ with velocities lying in the interval $(\boldsymbol{\xi},\boldsymbol{\xi}+\mathrm{d}\boldsymbol{\xi})$ at time t (BOLTZMANN, 1877).

2.3.1 Continuous Boltzmann Equation

The particles are constantly changing their velocity direction as they collide, as shown in Figure 7, where, for an infinitesimal time interval Δt, the distribution function f evolves from:

$$f\left(\boldsymbol{x},\boldsymbol{\xi},t\right) \quad \rightarrow \quad f\left(\boldsymbol{x}+\Delta\boldsymbol{x},\boldsymbol{\xi}+\Delta\boldsymbol{\xi},t+\Delta t\right)$$

Physically, this can be understood as many molecules in a portion of space traveling at certain speed intervals. Due to collisions, particle velocities $\boldsymbol{\xi}$ are constantly changing and, consequently, the distribution f. This phenomenon can be described by the total derivative in time of the distribution function:

$$\frac{\mathrm{d}f}{\mathrm{d}t} = \lim_{\Delta t\to 0} \frac{f\left(\boldsymbol{x}+\Delta\boldsymbol{x},\boldsymbol{\xi}+\Delta\boldsymbol{\xi},t+\Delta t\right) - f\left(\boldsymbol{x},\boldsymbol{\xi},t\right)}{\Delta t}. \tag{20}$$

It is convenient to adopt Einstein notation for subsequent LBM formulations. In this convention, a repeated index implies summation over a set of indexed terms. The Taylor series

Figure 7 – Schematic of particle distribution evolution due to collision. The particles are constantly moving, colliding and changing their directions, consequently f.

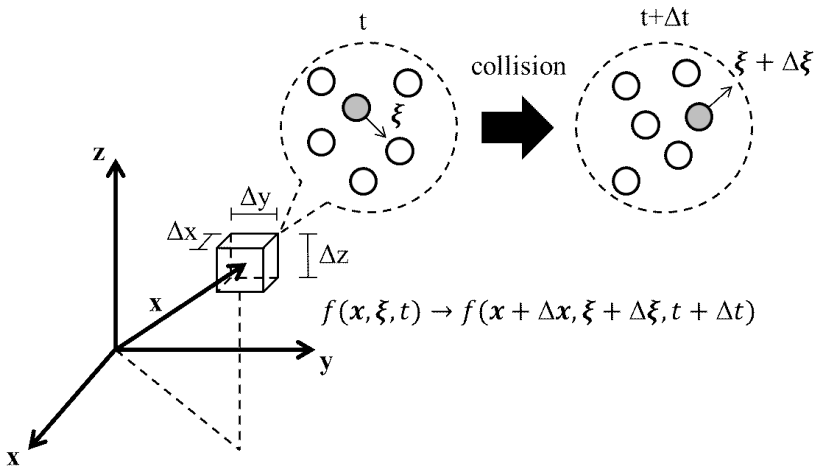

Source: Own elaboration.

expansion of Equation 20 until second-order is then written as:

$$\frac{\mathrm{d}f}{\mathrm{d}t} = \left(\frac{\partial f}{\partial t}\right)\frac{\mathrm{d}t}{\mathrm{d}t} + \left(\frac{\partial f}{\partial x_\alpha}\right)\frac{\mathrm{d}x_\alpha}{\mathrm{d}t} + \left(\frac{\partial f}{\partial \xi_\alpha}\right)\frac{\mathrm{d}\xi_\alpha}{\mathrm{d}t}. \tag{21}$$

The total derivative $\mathrm{d}f/\mathrm{d}t$ is replaced by collision operator $\Omega(f)$ (BEENAKKER *et al.*, 1973). Being $(\mathrm{d}x_\alpha/\mathrm{d}t) = \xi_\alpha$ and $(\mathrm{d}\xi_\alpha/\mathrm{d}t) = F_\alpha/n$ (specific body force), Equation 21 is rewritten as

$$\Omega(f) = \frac{\partial f}{\partial t} + \xi_\alpha\frac{\partial f}{\partial x_\alpha} + \frac{F_\alpha}{n}\frac{\partial f}{\partial \xi_\alpha}, \tag{22}$$

in which n represents the density of molecules. Equation 22 is known as the Boltzmann equation and can be seen as a type of advection equation, with the two first RHS terms representing the distribution function being advected with velocity ξ_α, and the third RHS term, the forces affecting velocity ξ_α (CHAPMAN *et al.*, 1990). This description returns the macroscopic moments up to the second-order. Mass n, momentum nu_α and energy densities ne can be written, respectively, as:

$$n = \int f\mathrm{d}\xi_\alpha; \tag{23a}$$

$$nu_\alpha = \int \xi_\alpha f\mathrm{d}\xi_\alpha; \tag{23b}$$

$$ne = \frac{1}{2}\int v_\alpha v_\alpha f\mathrm{d}\xi_\alpha. \tag{23c}$$

here, e represents the macroscopic internal energy density and $v_\alpha = \xi_\alpha - u_\alpha$ the relative velocity, which is the deviation of the microscopic particle's velocity from macroscopic local velocity.

An important variable in Kinetic Theory is the equilibrium function f^{eq} which consists of an expansion of Maxwell-Boltzmann distribution function for low Mach number, given by (MAXWELL, 1867):

$$f^{\text{eq}} = n\left(\frac{m}{2\pi kT}\right)^{D/2} e^{-\frac{m}{2kT}v_\alpha v_\alpha}, \tag{24}$$

where D the dimension of considered description. This result was first derived in 1860, by James C. Maxwell, on heuristic grounds and later, in the 1870s, by Ludwig E. Boltzmann, who performed significant investigations through a statistical mechanical approach into the physical origins of this distribution. The equilibrium function f^{eq} is a key element when solving LBM problems.

2.3.2 BGK Collision Operator

Boltzmann original collision operator considers all possible outcomes of two-particle collisions for any choice of intermolecular forces which results in (BOLTZMANN, 1896, 1898):

$$\Omega(f) = \int\int \left[f(\boldsymbol{x}, \boldsymbol{\xi}^*, t) f_1(\boldsymbol{x}, \boldsymbol{\xi}_1^*, t) - f(\boldsymbol{x}, \boldsymbol{\xi}, t) f_1(\boldsymbol{x}, \boldsymbol{\xi_1}, t\right] \beta \left|\xi_{1\alpha} - \xi_\alpha\right| \mathrm{d}\Omega \mathrm{d}\xi_{1\alpha}, \tag{25}$$

where the subscript 1 denotes a bullet particle, $|\xi_{1\alpha} - \xi_\alpha|$ is the relative velocity between target and bullet, β is the impact parameter, which is the distance of closest approach between two particles, and the superscript * is given for post-collision variables. Therefore, Eq 25 describes the net change of distribution function due to collisions between material points. A particle will change its velocity from ξ_α to ξ_α^* after a collision, causing the bullet particle to change its velocity from $\xi_{1\alpha}$ to $\xi_{1\alpha}^*$. The integral of all possibilities in collision space $\int \mathrm{d}\Omega$ determine the distribution function change for an infinitesimal time interval $\mathrm{d}f/\mathrm{d}t$.

Collisions conserve quantities of mass, momentum and translational energy (for monatomic case) (CHAPMAN *et al.*, 1990), thereby those constraints are represented as moments

of $\Omega(f)$:

$$\text{mass conservation:} \qquad \int \Omega(f) \mathrm{d}\xi_\alpha = 0; \tag{26a}$$

$$\text{momentum conservation:} \qquad \int \xi_\alpha \Omega(f) \mathrm{d}\xi_\alpha = 0; \tag{26b}$$

$$\text{total energy conservation:} \qquad \int v_\alpha v_\alpha \Omega(f) \mathrm{d}\xi_\alpha = 0. \tag{26c}$$

Boltzmann collision operator results in a burdensome integral over velocity space and can be highly non-linear. To avoid such complications, Bhatnagar *et al.* (1954) introduced a much simpler operator:

$$\Omega_{BGK}(f) = -\frac{1}{\tau}\left(f - f^{\mathrm{eq}}\right). \tag{27}$$

Named after its inventors, Bhatnagar, Gross and Krook, the BGK collision operator uses a mean free-path treatment and expresses the fact that collisions tend to relax the distribution function towards an equilibrium value f^{eq} (BHATNAGAR *et al.*, 1954). The constant τ, known as relaxation time, represents some suitable average collision time.

An appropriate collision operator has to respect the equalities expressed in Equation 26 and ensure that the distribution function f evolves towards its equilibrium f^{eq}. Within these constraints, the BGK-operator is the simplest collision operator available. Since τ is the only time parameter, the BGK-operator is often referred to as single-relaxation-time (SRT) (SUCCI, 2001). The BGK-operator is very robust for single-phase fluids and its stability can be tremendously improved through regularization (MATTILA *et al.*, 2017).

The BGK-Boltzmann equation is written by substituting Ω_{BGK} in Eq 22, which gives:

$$\frac{\partial f}{\partial t} + \xi_\alpha \frac{\partial f}{\partial x_\alpha} + \frac{F_\alpha}{n}\frac{\partial f}{\partial \xi_\alpha} = -\frac{1}{\tau}\left(f - f^{\mathrm{eq}}\right). \tag{28}$$

This equation is the most popular kinetic model and can be used to replace the equation of motion in fluid dynamics problems. The sum of effects caused by advection of the distribution function (two first LHS terms) and application of external forces (third LHS term) is represented by f evolution approaching equilibrium for a relaxation time τ.

2.4 LATTICE BOLTZMANN METHOD

The lattice Boltzmann method was introduced by McNamara and Zanetti (1988) and differs from traditional computational fluid dynamics methods because is formulated on the mesoscopic scale and, instead of solving the equations of mass, momentum and energy, it numerically solves Boltzmann equation. The LBM development for a fluid flow occurs through the discretization of: physical space, velocities domain, and time (HE; LUO, 1997; PHILIPPI *et al.*, 2006). Figure 8 exemplifies this continuous-discrete transition for a two-dimensional space. As illustrated, the discrete set of velocities $\{\boldsymbol{\xi}_i\}$ must be built such that the distribution function is shifted between neighboring points.

Figure 8 – Discretization example of Boltzmann equations through the creation of a velocity set with 9 directions, $\xi_0 = 0$ included.

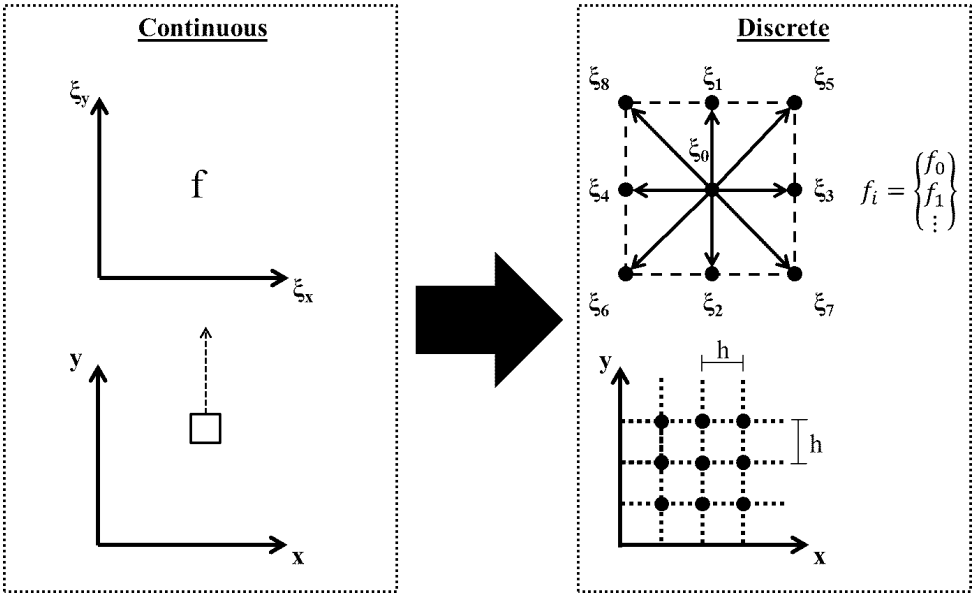

Source: Own elaboration.

This restriction for the discretization of mesoscopic velocity is described by the Courant-Friedrichs-Lewy (CFL) condition, which states that the distance traveled by any information during the time-step must be lower than the distance between two mesh points (LANEY, 1998). The CFL number will then be given by the following equation:

$$\mathrm{CFL} = \frac{|\Delta \boldsymbol{x}|}{|\boldsymbol{\xi}|\,\delta_t}. \tag{29}$$

The CFL condition relates time-step, interval lengths of each spatial coordinate and the maximum speed which information can travel at the physical space (COURANT *et al.*, 1967).

The discretization of the velocity space results in a discrete set of the distribution function $\{f_i(\boldsymbol{x},t)\}$, whose elements are also referred as populations. Substituting in Equation 28

$$\frac{\partial f_i}{\partial t} + \xi_{i\alpha}\frac{\partial f_i}{\partial x_\alpha} + \frac{F_{i\alpha}}{n}\frac{\partial f_i}{\partial \xi_{i\alpha}} = -\frac{1}{\tau}\left(f_i - f_i^{\mathrm{eq}}\right), \tag{30}$$

where f_i^{eq} is the equilibrium function discretized for the velocity space. The Taylor series expansion of f_i up to second-order for a time interval δ_t, is written as:

$$f_i(\boldsymbol{x}+\Delta\boldsymbol{x}, t+\delta_t) = f_i(\boldsymbol{x},t) + \delta_t\left(\frac{\partial f_i}{\partial t} + \frac{\Delta x_{i\alpha}}{\delta_t}\frac{\partial f_i}{\partial x_\alpha}\right) + O(\delta_t^2) + O(|\Delta\boldsymbol{x}|^2). \tag{31}$$

Neglecting the second-order or above terms and being $\Delta x_{i\alpha}/\delta_t = \xi_{i\alpha}$, Equations 30 and 31 can be combined into:

$$f_i(\boldsymbol{x}+\Delta\boldsymbol{x}, t+\delta_t) = f_i(\boldsymbol{x},t) - \frac{[f_i(\boldsymbol{x},t) - f_i^{eq}(\boldsymbol{x},t)]}{\bar{\tau}} - \delta_t\frac{F_{i\alpha}}{n}\frac{\partial f_i}{\partial \xi_{i\alpha}}(\boldsymbol{x},t), \tag{32}$$

where the bar symbol (e.g $\bar{\tau} = \tau/\delta_t$) is used to distinguish dimensionless terms. It is common practice in LBM to work using variables with no physical dimension often referred to as lattice variables.

The value of a non-dimensional variable is completely independent of the measuring units, therefore, it can be advantageous to work using dimensionless quantities in fluid dynamics problems, as they do not involve human-invented scales (m, kg, K...). Nondimensionalization is achieved by dividing a dimensional quantity by a chosen reference value of the same dimension. For the considered LBM development, the characteristic set of reference parameters is:

- h[m] - the constant distance between neighbor nodes;
- δ_t[s] - the physical value of a time interval under which f_i was expanded in a Taylor series;
- $\langle|\boldsymbol{\xi}|\rangle$[m/s] - the average molecule speed in an ideal gas;
- n_0[particles/m^3] - the reference density of molecules, it is common to adopt dimensionless reference density as $\bar{\rho}_0 = 1$ in LBM simulations;
- u_0[m/s] - the reference flow velocity. To operate in the quasi-incompressible limit, all simulated velocities have to be significantly smaller than sound speed $u_0 \ll c_s$.

Kinetic theory shows that the average particle speed in an ideal gas is (JEANS, 1940):

$$\langle|\boldsymbol{\xi}|\rangle = \sqrt{\frac{kT}{m}}. \tag{33}$$

Therefore, for ideal gases, particles travel at an average velocity close to the speed of sound, as $c_s = \sqrt{\gamma kT/m}$. In LBM, the dimensionless speed of sound $\bar{c}_s$ is given by:

$$\bar{c}_s = \frac{\delta_t}{h}\langle|\boldsymbol{\xi}|\rangle, \tag{34}$$

where the ratio h/δ_t is commonly referred to as lattice speed c. Using those parameters, the dimensionless lattice-variables in a D-dimensional representation are:

$$\Delta\bar{x} = \frac{\Delta x}{h}; \quad \Delta\bar{t} = \frac{\Delta t}{\delta_t}; \quad \bar{\rho} = \frac{n}{n_0}; \quad \bar{\boldsymbol{u}} = \frac{\boldsymbol{u}}{c}; \quad \bar{f}_i = \frac{\langle|\boldsymbol{\xi}|\rangle^D}{n_0} f_i; \quad \bar{\boldsymbol{\xi}}_i = \frac{\boldsymbol{\xi}_i}{\langle|\boldsymbol{\xi}|\rangle}; \quad \boldsymbol{e_i} = \frac{\boldsymbol{\xi_i}}{c}.$$

Which also implies $\boldsymbol{e}_i = \bar{c}_s\bar{\boldsymbol{\xi}}_i$. The non-dimensional form of Equation 32, or lattice Boltzmann equation (LBE) is given by:

$$\bar{f}_i(\bar{\boldsymbol{x}} + \Delta\bar{\boldsymbol{x}}, \bar{t} + \Delta\bar{t}) = \bar{f}_i(\bar{\boldsymbol{x}},\bar{t}) - \frac{\left[\bar{f}_i(\bar{\boldsymbol{x}},\bar{t}) - \bar{f}_i^{\text{eq}}(\bar{\boldsymbol{x}},\bar{t})\right]}{\bar{\tau}} + \bar{S}_i(\bar{\boldsymbol{x}},\bar{t}), \tag{35}$$

in which $\bar{S}_i$ is a source term that represents the discretization of third RHS term from Equation 32. The Hermite expansion of S_i from body force in Boltzmann equation is shown in (SHAN *et al.*, 2006). Guo *et al.* (2002) approximates S_i with a power series written as:

$$\bar{S}_i = \left(1 - \frac{1}{2\bar{\tau}}\right) w_i \left(\frac{e_{i\alpha}}{\bar{c}_s^2} + \frac{\left(e_{i\alpha}e_{i\beta} - \bar{c}_s^2\delta_{\alpha\beta}\right)\bar{u}_\beta}{\bar{c}_s^4}\right)\bar{F}_\alpha, \tag{36}$$

where w_i are the weighting factors and $\bar{F}_\alpha$ is the dimensionless macroscopic force density. The first three velocity moments of source term $\bar{S}_i$ are (KRÜGER *et al.*, 2017):

$$\sum_i \bar{S}_i = 0; \tag{37a}$$

$$\sum_i \bar{S}_i e_{i\alpha} = \left(1 - \frac{1}{2\bar{\tau}}\right)\bar{F}_\alpha; \tag{37b}$$

$$\sum_i \bar{S}_i e_{i\alpha}e_{i\beta} = \left(1 - \frac{1}{2\bar{\tau}}\right)\left(\bar{F}_\alpha\bar{u}_\beta + \bar{u}_\alpha\bar{F}_\beta\right). \tag{37c}$$

The equilibrium function $\bar{f}_i^{\text{eq}}$ for discretized velocity space can be obtained through a Hermite expansion up to second-order (PHILIPPI *et al.*, 2006), which gives:

$$\bar{f}_i^{\text{eq}} = w_i \bar{\rho} \left[1 + \frac{(e_{i\alpha}\bar{u}_\alpha)}{\bar{c}_s^2} + \frac{\bar{u}_\alpha \bar{u}_\beta \left(e_{i\alpha} e_{i\beta} - \bar{c}_s^2 \delta_{\alpha\beta} \right)}{2\bar{c}_s^4} \right]. \tag{38}$$

With the three first velocity moments of f_i^{eq} given by (KRÜGER *et al.*, 2017):

$$\sum_i \bar{f}_i^{\text{eq}} = \bar{\rho}; \tag{39a}$$

$$\sum_i \bar{f}_i^{\text{eq}} e_{i\alpha} = \bar{\rho}\bar{u}_\alpha; \tag{39b}$$

$$\sum_i \bar{f}_i^{\text{eq}} e_{i\alpha} e_{i\beta} = \bar{\rho}\bar{c}_s^2 \delta_{\alpha\beta} + \bar{\rho}\bar{u}_\alpha \bar{u}_\beta = \bar{\Pi}_{\alpha\beta}^{\text{eq}}; \tag{39c}$$

$$\sum_i \bar{f}_i^{\text{eq}} e_{i\alpha} e_{i\beta} e_{i\gamma} = \bar{\rho}\bar{c}_s^2 \left(\bar{u}_\alpha \delta_{\beta\gamma} + \bar{u}_\beta \delta_{\alpha\gamma} + \bar{u}_\gamma \delta_{\alpha\beta} \right) = \bar{\Pi}_{\alpha\beta\gamma}^{\text{eq}}. \tag{39d}$$

The values for w_i are given according to the defined lattice arrangement. For the sake of simplicity, the bar notation for dimensionless variables will be dropped from this point on.

2.4.1 Lattice Arrangements

The lattice arrangements also referred to as velocity sets, are named according to the number of its spatial dimensions and discrete velocities, hence a D3Q19 velocity set, represents a 3-dimensional space with velocity discretized for 19 directions (QIAN *et al.*, 1992). The velocity sets can be modeled from Boltzmann equation through Gauss-Hermite quadrature. The reader may refer to (PHILIPPI *et al.*, 2006) for a detailed discussion over this procedure.

A velocity set for a LBM algorithm is fully described by two arrays of defined variables: the velocities $\{\boldsymbol{e}_i\}$ and their corresponding weights $\{w_i\}$. Those variables have to obey some general conditions. Apart from conservation of mass and momentum, a preeminent requirement is the rotational isotropy of the lattice, achieved when all moments of weight w_i up to fifth-order

are isotropic, this leads to (KRÜGER *et al.*, 2017):

$$\sum_i w_i = 1; \tag{40a}$$

$$\sum_i w_i e_{i\alpha} = 0; \tag{40b}$$

$$\sum_i w_i e_{i\alpha} e_{i\beta} = c_s^2 \delta_{\alpha\beta}; \tag{40c}$$

$$\sum_i w_i e_{i\alpha} e_{i\beta} e_{i\gamma} = 0; \tag{40d}$$

$$\sum_i w_i e_{i\alpha} e_{i\beta} e_{i\gamma} e_{i\mu} = c_s^4 \left(\delta_{\alpha\beta}\delta_{\gamma\mu} + \delta_{\alpha\gamma}\delta_{\beta\mu} + \delta_{\alpha\mu}\delta_{\beta\gamma}\right); \tag{40e}$$

$$\sum_i w_i e_{i\alpha} e_{i\beta} e_{i\gamma} e_{i\mu} e_{i\nu} = 0. \tag{40f}$$

Additionally, all weights w_i have to be non-negative. Some of the most usual lattice arrangements employed in LBM flow simulation can be seen in Figure 9.

Figure 9 – D1Q3, D2Q9 and D3Q19 velocity sets. The square and cube denoted by solid lines have an edge length $2\Delta x$.

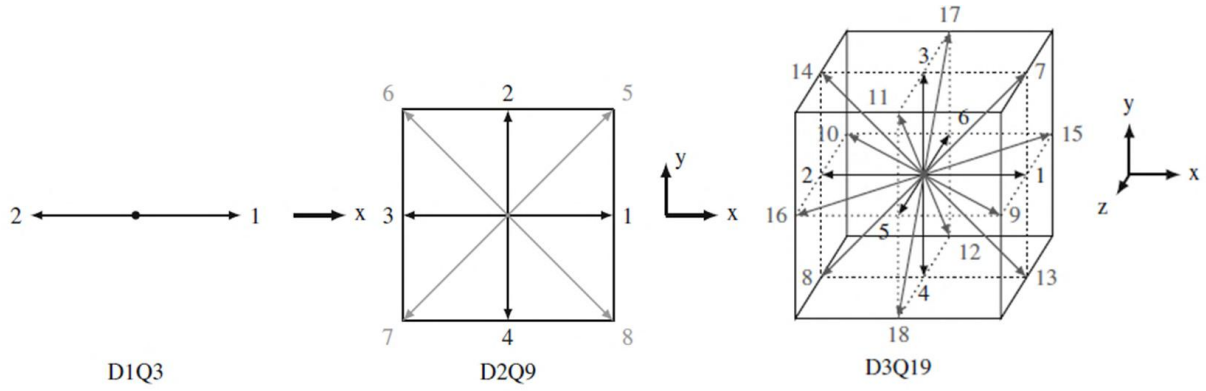

Source: Adapted from Krüger *et al.* (2017).

As velocities vectors $\boldsymbol{e}_i$ direct connect the lattice sites, for lattices separated by a constant distance Δx and time step Δt, the velocity vectors are multipliers of $\Delta x/\Delta t$. It is very common to set the dimensionless parameters Δx and Δt to the unity, and c_s to $1/\sqrt{3}$ (KRÜGER *et al.*, 2017). Table 1 summarizes some usual velocity sets.

Table 1 – Properties of usual dimensionless velocity sets for LBM simulation. The speed of sound for those is taken as $c_s = 1/\sqrt{3}$.

Notation	Velocities $\boldsymbol{e}_i$	Number	Length $\lvert\boldsymbol{e}_i\rvert$	Weight w_i
D1Q3	(0)	1	0	$2/3$
	(±1)	2	1	$1/6$
D2Q9	$(0,0)$	1	0	$2/3$
	$(\pm1,0),(0,\pm1)$	4	1	$4/9$
	$(\pm1,\pm1)$	4	$\sqrt{2}$	$1/36$
D3Q19	$(0,0,0)$	1	0	$1/3$
	$(\pm1,0,0),(0,\pm1,0),(0,0,\pm1)$	6	1	$1/18$
	$(\pm1,\pm1,0),(\pm1,0,\pm1),(0,\pm1,\pm1)$	12	$\sqrt{2}$	$1/36$

Source: Krüger *et al.* (2017).

2.5 FROM MESOSCOPIC TO MACROSCOPIC

In flow simulations one is mostly interested in the macroscopic behavior, therefore it is important to understand how LBM mesoscopic variables can return the macroscopic quantities from the equations of change. As the continuous distribution function f, LBM variables preserve macroscopic moments through summation of f_i, $e_{i\alpha}$ and S_i (SILVA; SEMIAO, 2012):

$$\rho = \sum_i f_i; \tag{41a}$$

$$\rho u_\alpha = \sum_i f_i e_{i\alpha} + \frac{\Delta t}{2} F_\alpha; \tag{41b}$$

$$\Pi_{\alpha\beta} = \left(1 - \frac{\Delta t}{2\tau}\right) \sum_i f_i e_{i\alpha} e_{i\beta} + \frac{\Delta t}{2} \sum_i S_i e_{i\alpha} e_{i\beta}, \tag{41c}$$

where $\Pi_{\alpha\beta}$ is related to inertial and viscous forces. The first and second velocity moments of the non-equilibrium populations $f_i^{\text{neq}} = f_i - f_i^{\text{eq}}$ can be deduced from Equations 39a, 39b, 41a and 41b as being:

$$\sum_i f_i^{\text{neq}} = 0; \tag{42a}$$

$$\sum_i f_i^{\text{neq}} e_{i\alpha} = -\frac{\Delta t}{2} F_\alpha. \tag{42b}$$

The Navier-Stokes equations (NSE) are a macroscopic description of momentum balance for a Newtonian fluid and can be related with LBE through Chapman-Enskog analysis,

a procedure named after Sydney Chapman and David Enskog, who independently developed analogous methods to obtain NSE from the Boltzmann equation.

The core of Chapman-Enskog analysis resides on observing that since Boltzmann equation returns Euler momentum equation when $f \simeq f^{\text{eq}}$, the viscous forces are connected to a non-equilibrium part of distribution function $f^{\text{neq}} = f - f^{\text{eq}}$. Through a perturbation expansion of f_i around f_i^{eq} with the Knudsen number as expansion parameter $Kn = \epsilon$, such that $f_i^{\text{neq}} = \epsilon f_i^{(1)} + \epsilon^2 f_i^{(2)}$.... The populations f_i are written as (CHAPMAN *et al.*, 1990):

$$f_i = f_i^{\text{eq}} + \epsilon f_i^{(1)} + \epsilon^2 f_i^{(2)} + ... \tag{43}$$

By the ansatz that only the two lowest-orders in Kn are sufficient to return NSE, $f_i^{\text{neq}} = \epsilon f_i^{(1)} + \epsilon^2 f_i^{(2)}$. Writing f_i in a Taylor expansion up to second-order:

$$f_i\left(\boldsymbol{x} + \boldsymbol{e}_i \Delta t, t + \Delta t\right) - f_i\left(\boldsymbol{x}, t\right) = \Delta t \left(\partial_t + e_{i\alpha}\partial_\alpha\right) f_i + \frac{\Delta t^2}{2}\left(\partial_t + e_{i\alpha}\partial_\alpha\right)^2 f_i, \tag{44}$$

where the contracted derivative notation is adopted, $\partial_\alpha\left(\right) = \partial\left(\right)/\partial x_\alpha$ and $\partial_t\left(\right) = \partial\left(\right)/\partial t$. The LHS of Equation 44 can be combined with Equation 35 resulting in:

$$-\frac{\left[f_i - f_i^{\text{eq}}\right]}{\tau} + S_i = \Delta t \left(\partial_t + e_{i\alpha}\partial_\alpha\right) f_i + \frac{\Delta t^2}{2}\left(\partial_t + e_{i\alpha}\partial_\alpha\right)^2 f_i. \tag{45}$$

The second-order terms are eliminated by subtraction of $\left(\Delta t/2\right)\left(\partial_t + e_{i\alpha}\partial_\alpha\right)$ applied to Equation 45 itself, which after simplifications results in:

$$-\frac{1}{\tau}\left(f_i - f_i^{\text{eq}}\right) + S_i = \left(\partial_t + e_{i\alpha}\partial_\alpha\right)\left[f_i - \frac{\Delta t}{2\tau}\left(f_i - f_i^{\text{eq}}\right) + \frac{\Delta t}{2} S_i\right]. \tag{46}$$

Time derivative is rewritten as a multiple scale expansion $\partial_t = \epsilon\partial_t^{(1)} + \epsilon^2\partial_t^{(2)}$ and space derivative labeled as $\partial_\alpha = \epsilon\partial_\alpha^{(1)}$. An ansatz that the order $O(\epsilon)$ is sufficient for the representation of source term $S_i = \epsilon S_i^{(1)}$ (BUICK; GREATED, 2000) is also employed. Applying the expansions to f_i, S_i, and the derivatives in Equation 46, and separating the terms by their Knudsen order gives:

$$O\left(\epsilon\right): \qquad \left(\partial_t^{(1)} + e_{i\alpha}\partial_\alpha^{(1)}\right) f_i^{\text{eq}} - S_i^{(1)} = -\frac{f_i^{(1)}}{\tau}; \tag{47a}$$

$$O\left(\epsilon^2\right): \qquad \partial_t^{(2)} f_i^{\text{eq}} + \left(\partial_t^{(1)} + e_{i\alpha}\partial_\alpha^{(1)}\right)\left[\left(1 - \frac{\Delta t}{2\tau}\right) f_i^{(1)} + \frac{\Delta t}{2} S_i^{(1)}\right] = -\frac{f_i^{(2)}}{\tau}. \tag{47b}$$

Through the multiplication of Equation 47 by 1, $e_{i\alpha}$ and $e_{i\alpha}e_{i\beta}$ followed by summation over index i, the velocity moments for $O(\epsilon)$ are:

$$\partial_t^{(1)}\rho + \partial_\alpha^{(1)}\left(\rho u_\alpha\right) = 0; \tag{48a}$$

$$\left(1 - \frac{\Delta t}{2\tau}\right)\left[\partial_t^{(1)}\left(\rho u_\alpha\right) + \partial_\alpha^{(1)}\Pi_{\alpha\beta}^{\text{eq}}\right] = \sum_i S_i^{(1)} e_{i\alpha}; \tag{48b}$$

$$-\tau\left[\left(1 - \frac{\Delta t}{2\tau}\right)\left(\partial_t^{(1)}\Pi_{\alpha\beta}^{\text{eq}} + \partial_\gamma^{(1)}\Pi_{\alpha\beta\gamma}^{\text{eq}}\right) - \sum_i S_i^{(1)} e_{i\alpha}e_{i\beta}\right] = \Pi_{\alpha\beta}^{(1)}. \tag{48c}$$

and the two first velocity moments for $O(\epsilon^2)$ are:

$$\partial_t^{(2)}\rho = 0; \tag{49a}$$

$$\partial_t^{(2)}\left(\rho u_\alpha\right) + \partial_\beta^{(1)}\Pi_{\alpha\beta}^{(1)} = 0. \tag{49b}$$

Combining Equations 48a and 49a gives:

$$\partial_t\rho + \partial_\alpha\left(\rho u_\alpha\right) = 0, \tag{50}$$

which is the equation of continuity obtained through the continuum approach, stating that mass is conserved in the system (PANTON, 2013). Analogously, the assembly of Equations 48b and 49b should yield the macroscopic momentum balance:

$$\partial_t\left(\rho u_\alpha\right) + \partial_\beta\left(\Pi_{\alpha\beta}^{\text{eq}} + \epsilon\Pi_{\alpha\beta}^{(1)}\right) = F_\alpha. \tag{51}$$

An explicit expression for $\Pi_{\alpha\beta}^{(1)}$ can be obtained from Equation 48c. Substituting the values from Equations 39c and 39d, the derivatives $\partial_t^{(1)}\Pi_{\alpha\beta}^{\text{eq}}$, $\partial_\beta^{(1)}\Pi_{\alpha\beta}^{\text{eq}}$ and $\partial_\gamma^{(1)}\Pi_{\alpha\beta\gamma}^{\text{eq}}$ are:

$$\partial_t^{(1)}\Pi_{\alpha\beta}^{\text{eq}} = \partial_t^{(1)}\left(\rho c_s^2\delta_{\alpha\beta}\right) + \partial_t^{(1)}\left(\rho u_\alpha u_\beta\right); \tag{52a}$$

$$\partial_\beta^{(1)}\Pi_{\alpha\beta}^{\text{eq}} = \partial_\beta^{(1)}\left(\rho c_s^2\delta_{\alpha\beta}\right) + \partial_\beta^{(1)}\left(\rho u_\alpha u_\beta\right); \tag{52b}$$

$$\partial_\gamma^{(1)}\Pi_{\alpha\beta\gamma}^{\text{eq}} = c_s^2\left[\partial_\beta^{(1)}\left(\rho u_\alpha\right) + \partial_\alpha^{(1)}\left(\rho u_\beta\right) + \delta_{\alpha\beta}\partial_\gamma^{(1)}\left(\rho u_\gamma\right)\right]. \tag{52c}$$

The product rule is then applied for $(\rho u_\alpha u_\beta)$ terms and $\partial_t^{(1)}(\rho u_\alpha)$ is obtained from Equation 48b. After some simplifications, $\epsilon\Pi_{\alpha\beta}^{(1)}$ is reduced to:

$$\epsilon\Pi_{\alpha\beta}^{(1)} = -\left(\tau - \frac{\Delta t}{2}\right)\rho c_s^2\left(\partial_\alpha u_\beta + \delta_\beta u_\alpha\right). \tag{53}$$

By defining an apparent viscosity η

$$\eta = \rho c_s^2\left(\tau - \frac{\Delta t}{2}\right), \tag{54}$$

and being the thermodynamic pressure $p = \rho c_s^2$, Equation 51 is rewritten as:

$$\partial_t(\rho u_\alpha) + \partial_\beta(\rho u_\alpha u_\beta) = -\partial_\alpha p + \partial_\beta\left[\eta\left(\partial_\alpha u_\beta + \partial_\beta u_\alpha\right)\right] + F_\alpha, \tag{55}$$

which is the momentum conservation equation for a Generalized Newtonian fluid (BIRD *et al.*, 1987). From Equation 54 it can be found $\tau \geq 0.5\Delta t$ as a necessary condition for LBM stability (KRÜGER *et al.*, 2017).

2.6 GENERALIZED NEWTONIAN FLUID

Firstly proposed by Isaac Newton in his famous "Principia Mathematica" and subsequently, in 1845, expanded by Stokes for three-dimensional mathematical form, the viscous stress of a incompressible Newtonian fluid can be written as (MACOSKO, 1994):

$$\boldsymbol{\tau} = \eta 2\boldsymbol{D}, \tag{56}$$

where η is a material function called fluid dynamic viscosity and is a measure of its resistance to deformation by shear stress. For a Newtonian fluid this value is independent of shear stress and shear rate, being a function only of some properties like pressure and temperature (BIRD *et al.*, 1987). The factor $2\boldsymbol{D}$ (also written as $\dot{\boldsymbol{\gamma}}$) is the rate-of-strain tensor and is defined as:

$$2\boldsymbol{D} = \dot{\boldsymbol{\gamma}} = \nabla\boldsymbol{u} + \nabla(\boldsymbol{u})^T, \tag{57}$$

in which, $\nabla(\boldsymbol{u})^T$ represents the transpose of $\nabla\boldsymbol{u}$.

By incorporating the idea of a shear-dependent viscosity one can describe some non-Newtonian effects like shear-thinning, where the fluid apparent viscosity decreases with increasing shear rate, and shear-thickening, where the apparent viscosity rises with increasing shear rate.

The Generalized Newtonian fluid (GNF) results from a minor modification of the Newtonian fluid constitutive equation (BIRD *et al.*, 1987):

$$\boldsymbol{\tau} = \eta(I_{2\boldsymbol{D}}, II_{2\boldsymbol{D}}, III_{2\boldsymbol{D}})2\boldsymbol{D}, \tag{58}$$

where $I_{2\boldsymbol{D}}$, $II_{2\boldsymbol{D}}$ and $III_{2\boldsymbol{D}}$ are the first, second, and third shear rate tensor invariants, respectively. They can be written as (MACOSKO, 1994):

$$I_{2\boldsymbol{D}} = \text{tr}2\boldsymbol{D}; \tag{59a}$$

$$II_{2\boldsymbol{D}} = \frac{1}{2}\left((\text{tr}2\boldsymbol{D})^2 - \text{tr}\,(2\boldsymbol{D})^2\right); \tag{59b}$$

$$III_{2\boldsymbol{D}} = \text{det}2\boldsymbol{D}. \tag{59c}$$

where tr is the matrix trace. For an incompressible fluid, the first invariant will be zero since $I_{2\boldsymbol{D}} = \nabla \cdot \boldsymbol{u}$, also for simple shear flows, $III_{2\boldsymbol{D}} = 0$, and the above equation is simplified to:

$$\boldsymbol{\tau} = \eta(II_{2\boldsymbol{D}})2\boldsymbol{D}. \tag{60}$$

The GNF still cannot describe normal stresses or time-dependent elastic effects (BIRD *et al.*, 1987), however, under the basis of a $\eta(II_{2\boldsymbol{D}})$, some constitutive equations were developed to describe other non-Newtonian phenomena. Some of the most widely employed are the Power-Law, that can be used to describe some pseudoplastic and dilatant fluids, and the Bingham constitutive equation, that targets the representation of viscoplastic fluids.

The three described behaviors are qualitatively represented in Figure 10. In which is shown that the pseudoplastic fluid exhibits shear-thinning behavior, its apparent viscosity decreases with stress application while a dilatant fluid has the opposite response, shear-thickening. Present work focuses on viscoplasticity, to which the fluid only flows for stresses above a critical value.

2.6.1 Viscoplastic Fluid

A Viscoplastic fluid presents both plastic and viscous behavior. Plastic material is one that shows little or no deformation up to a certain level of stress. Above this *yield-stress*, the

Figure 10 – Comparative curve of non-Newtonian viscoplastic, dilatant and pseudoplastic fluids behavior with Newtonian fluid shear rate response over applied stress.

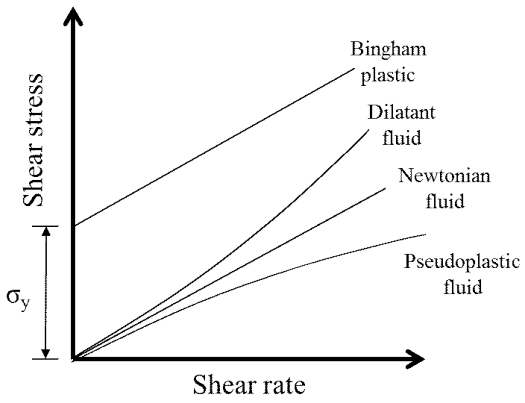

Source: Own elaboration.

material flows readily. House paint, margarine and ketchup are examples of viscoplastic materials (MACOSKO, 1994).

For ideal elastic materials, shear stress is proportional to the imposed strain as stated by an empirical, scalar, rule much like Newton's law of viscosity called Hooke's law, given by:

$$\boldsymbol{\tau} = G\boldsymbol{\gamma}, \tag{61}$$

where $\boldsymbol{\gamma}$ is the strain tensor and G is the elastic modulus. This equation may be used to describe a material operating below its yield stress.

A material that is completely rigid until a certain yield-stress σ_y, and that flows after this value is surpassed can be modeled by allowing no motion below the yield stress

$$\begin{aligned} \dot{\gamma} &= 0 \qquad\qquad \text{for } |\tau| < \sigma_y; \\ \tau &= \eta_0\dot{\gamma} + \sigma_y \quad \text{for } |\tau| \geq \sigma_y. \end{aligned} \tag{62}$$

This one-dimensional form is the one Bingham used in his original paper and was named after him as Bingham constitutive equation. To extend Equation 62 to the three-dimensional form it is necessary to replace one-dimensional yield criterion with some scalar function of the invariants of $\boldsymbol{\tau}$ (MACOSKO, 1994), that way:

$$\begin{aligned} 2\boldsymbol{D} &= \mathbf{0} \qquad\qquad\qquad\qquad \text{for } |II_{\boldsymbol{\tau}}| < \sigma_y^2; \\ \boldsymbol{\tau} &= \left(\eta_0 + \frac{\sigma_y}{|II_{2\boldsymbol{D}}|^{1/2}}\right) 2\boldsymbol{D} \quad \text{for } |II_{\boldsymbol{\tau}}| \geq \sigma_y^2, \end{aligned} \tag{63}$$

where η_0 is the zero shear viscosity. The Bingham fluid presents a linear shear rate dependence for stresses above yield-stress. The value of σ_y for a specific fluid found through experimental data can strongly vary for different $\dot{\gamma}$ ranges, especially in the lower shear rate range. As a consequence, picking the wrong shear rate range to fit the Bingham fluid can result in large σ_y errors (MACOSKO, 1994).

To avoid the discontinuity in the flow curve due to incorporation of a yield criterion, Papanastasiou (1987) proposed a modification to the Bingham equation by incorporating an exponential term that allowed the use of one equation for the entire flow curve, before and after yield. A Bingham fluid with the Papanastasiou modification can then be expressed as (PAPANASTASIOU, 1987):

$$\boldsymbol{\tau} = \left\{ \eta_0 + \frac{\sigma_y \left[1 - e^{\left(-a|II_{2\boldsymbol{D}}|^{1/2}\right)}\right]}{|II_{2\boldsymbol{D}}|^{1/2}} \right\} 2\boldsymbol{D}. \tag{64}$$

This is a regularization method widely employed in numerical simulations of viscoplastic fluids flows, as it facilitates implementation by eliminating the singularity in the Bingham equation. However, its dependence on a non-rheological parameter a, which controls the exponential growth of the yield-stress term of the classical Bingham fluid in regions subjected to very small strain-rates, can be pointed as a disadvantage of this constitutive equation (SOTO *et al.*, 2010). Besides, it is harder to delineate yield surfaces, since the regularization of apparent viscosity replaces the solid behavior by a very viscous fluid.

2.6.2 LBM for non-Newtonian Fluids

As there are advantages of working with LBM for Newtonian flow simulations, it is highly desirable to extend this methodology for non-Newtonian analysis. Most approaches use the fact that relaxation time from LBM does not have to be obligatory constant and, since it is possible to correlate the relaxation time with apparent viscosity of a GNF, some formulations of non-Newtonian fluids are possible by using a variable relaxation time $\tau = \tau(\eta)$. Nardi (2018) used this kind of approach in LBM for a 2D numerical study of a spherical particle settling in Power-Law fluid.

2.7 CHAPTER SUMMARY

This chapter provided some of the fundamental concepts that are used in the development of DNS algorithm. IBM and its formulation are introduced as an alternative of implementation in the Cartesian LBM grid for the representation of a particle immersed in fluid. The LBM was also discussed, from its roots at continuous Boltzmann equation until the establishment of a relationship with the macroscopic momentum equations. The chapter concluded with a brief discussion over generalized Newtonian fluids, focusing on the viscoplastic fluid and concluding with insight over the implementation of non-Newtonian constitutive equations in LBM.

3 NUMERICAL METHODOLOGY

This excerpt of the document is directed towards the interpretation of the gravity-driven motion of a particle in quiescent fluid and the numerical techniques used on the discretization of the problem proposed. Starting with IBM formulation, where meshing methodology and description of solid-body motion are detailed, proceeding with LBM regularization, boundary conditions implementation, the boundary relocation scheme and modification of relaxation time for a representation of the Bingham model. The Chapter is concluded with a summary of the proposed IB-LBM algorithm.

3.1 RIGID BODY MOTION IN IBM

To attain a specified boundary condition at particle's coordinates, the IBM considers a force density $\boldsymbol{f}(\boldsymbol{X})$ at the Lagrangian points denoting the force exerted on fluid by the particle. This vector $\boldsymbol{f}(\boldsymbol{X})$ is spread into Eulerian nodes defining a force field $\boldsymbol{F}(\boldsymbol{x})$ that assures that the interpolated velocity at the particle's surface respects a determined or calculated boundary condition. The described procedure is illustrated in Figure 11.

Figure 11 – Illustration of the spreading process of IBM. The forces calculated for Lagrangian nodes are distributed into Eulerian nodes, so that the interpolated velocities at the particle's surface respect a given or calculated boundary conditions.

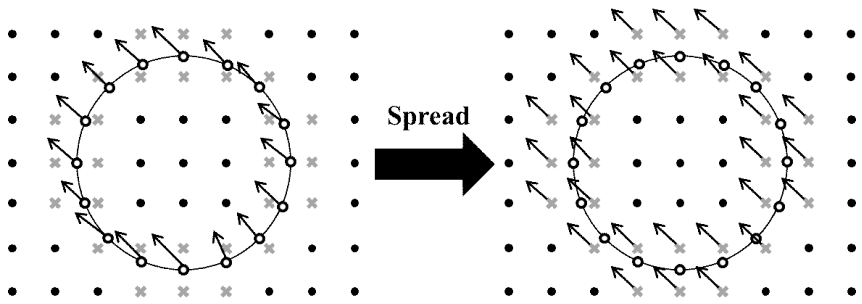

Source: Own elaboration.

The product $\Delta q \Delta r \Delta s$ from Equation 13b is rewritten as a relative volume element $\Delta b \Delta A$, with $\Delta b = 1$ being the assumed thickness of particle shell and ΔA the surface area of a single node. That way, spreading is performed through:

$$\boldsymbol{F}(\boldsymbol{x}) = \sum_{\boldsymbol{X} \in L_h} \boldsymbol{f}(\boldsymbol{X})\, D_h(\boldsymbol{x} - \boldsymbol{X})\, \Delta b \Delta A. \tag{65}$$

The force spreading is carried using a velocity correction term $\delta \boldsymbol{u}$, which is the difference between calculated and interpolated velocities $\delta \boldsymbol{u} = \boldsymbol{u}_{\text{calc}} - \boldsymbol{u}_{\text{interp}}$. From Equation 41b it is possible to establish an iterative scheme for the force density at Lagrangian nodes to satisfy a no-slip boundary condition, this is written as (DASH *et al.*, 2014):

$$\boldsymbol{f}^{(n+1)}\left(\boldsymbol{X}\right) = \boldsymbol{f}^{(n)}\left(\boldsymbol{X}\right) + 2\frac{\rho\left(\boldsymbol{X}\right)}{\Delta t}\delta \boldsymbol{u}^{(n)}\left(\boldsymbol{X}\right), \tag{66}$$

where $\rho\left(\boldsymbol{X}\right)$ is obtained from:

$$\rho\left(\boldsymbol{X}\right) = \sum_{\boldsymbol{x}\in E_h} \rho\left(\boldsymbol{x}\right) D_h\left(\boldsymbol{x} - \boldsymbol{X}\right) \Delta x^3. \tag{67}$$

The velocity field is then recalculated and spreading is repeated until a criterion error $L_1 = \sum ||\delta \boldsymbol{u}|| / \sum ||\boldsymbol{u}_{\text{calc}}||$ is attained or a predetermined amount of iterations is reached. Assuming a constant $\Delta A = A_s/N$ for a solid-body of surface area A_s and N Lagrangian nodes, it is desirable to design an IBM mesh of equally spaced points.

3.1.1 Meshing

The employed meshing technique can produce spherical and ellipsoidal meshes and consists of three main steps. The first step is to draw the vertices of an icosahedron and then make use of a hierarchical triangular mesh method (KUNSZT *et al.*, 2001). Each face of the regular polyhedron is regularly split into smaller triangles, as illustrated in Figure 12. This recursive decomposition is applied to each facet of the original icosahedron according to a desired refinement degree n_r.

Figure 12 – Representation of hierarchical triangular mesh. A triangular plane is subdivided in more triangular faces for each refinement degree n_r.

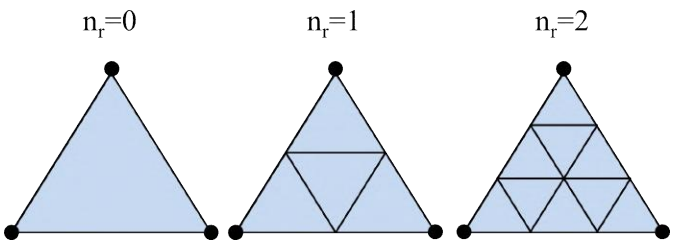

Source: Own elaboration.

Subsequently, the generated nodes are projected into a circumscribed sphere, as shown in Figure 13, building a spherical mesh of almost equally distributed points.

Figure 13 – Schematic of the meshing process for sphere: (a) the circumscribed regular icosahedron with vertices at sphere surface, (b) has each of its faces divided in 4 equal triangles, and (c) the new vertices are normalized and extended to sphere surface creating 80 faces circumscribed polyhedron.

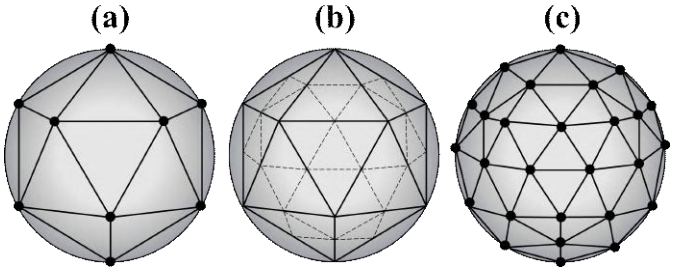

Source: Own elaboration.

In the second main step, all the constructed vector points are normalized to $\boldsymbol{X}^{(0)}$, and this unitary radius sphere is distorted through directional scaling, resulting in an ellipsoidal surface with A, B, and C as its principal axes. The new positions $\boldsymbol{X}^{(1)}$ of Lagrangian nodes are given by:

$$\boldsymbol{X}^{(1)} = [A \quad B \quad C]\, \boldsymbol{X}^{(0)}. \tag{68}$$

When the axes are unequal, the distortion differences in linear transformation leads to irregular distances between $\boldsymbol{X}^{(1)}$ points, and to overcome this issue the third step of the meshing procedure uses an iterative refinement process that considers vector positions $\boldsymbol{X}$ as particles that repel each other but are only allowed to move on the ellipsoidal surface. First the average force $\boldsymbol{R}_A\left(\boldsymbol{X}_i\right)$ inversely proportional to the square of distances between nodes is calculated. that way for a position $\boldsymbol{X}_i$:

$$\boldsymbol{R}_A\left(\boldsymbol{X}_i\right) = \frac{1}{N}\sum_{j=1}^{N} \frac{\boldsymbol{X}_i - \boldsymbol{X}_j}{||\boldsymbol{X}_i - \boldsymbol{X}_j||^3} \quad , \quad j \neq i. \tag{69}$$

By decomposing $\boldsymbol{R}_A$ in its normal and tangential forces $\boldsymbol{R}_A = \boldsymbol{R}_n + \boldsymbol{R}_t$, the normal component of repulsive force $\boldsymbol{R}_n$ is given by:

$$\boldsymbol{R}_n\left(\boldsymbol{X}_i\right) = \left[\boldsymbol{R}_A\left(\boldsymbol{X}_i\right) \cdot \boldsymbol{n}\left(\boldsymbol{X}_i\right)\right] \boldsymbol{n}\left(\boldsymbol{X}_i\right), \tag{70}$$

where the unitary normal of a quadric surface $\alpha(x,y,z)$ is $\boldsymbol{n} = \nabla\alpha/||\nabla\alpha||$. Tangential force is obtained by the subtraction $\boldsymbol{R}_t = \boldsymbol{R}_A - \boldsymbol{R}_n$ and, taking this force component, the nodes are dislocated tangentially to the their surface. The vector $\boldsymbol{R}_t$ will give the displacement of mesh

points so that the mid-process positions are given by:

$$\boldsymbol{X}_i^{(n+\frac{1}{2})} = \boldsymbol{X}_i^{(n)} + \frac{\Delta A}{\pi} \boldsymbol{R}_t \left(\boldsymbol{X}_i^{(n)} \right), \tag{71}$$

where $\Delta A/\pi$ is a factor used to scale with $1/||\boldsymbol{X}_i - \boldsymbol{X}_j||^2$ from Equation 69 and prevent an exaggerated displacement. The post-iteration position $\boldsymbol{X}_i^{(n+1)}$ is determined by the position in which the line coming from ellipsoid's center $\boldsymbol{X}_c$ towards $\boldsymbol{X}_i^{(n+1/2)}$ crosses the function defining the quadric surface $\alpha\,(x,y,z)$. This procedure is illustrated in Figure 14.

Figure 14 – Refinement procedure in which a point moves tangentially to ellipsoid's surface with resultant direction calculated from the total repulsive force exerted by other nodes. After dislocation, the mesh points are projected into ellipsoid geometry.

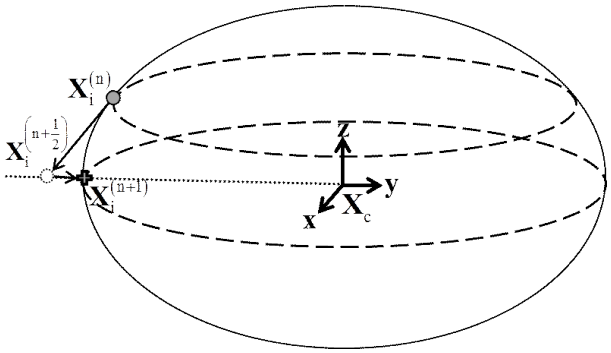

Source: Own elaboration.

In present work, a total of 200,000 iterations were adopted in each mesh generation, creating meshes of fair regularity , as shown in a summary of the three meshing steps in Figure 15. This mesh generation procedure only takes place once in pre-processing, and the resulting mesh can be reused in other simulations.

Figure 15 – Summary of the meshing process. At the end of step 1 we obtain a geodesic dome mesh, this geometry is distorted in an ellipsoidal shape at step 2. In an iterative process, mesh refinement is performed for more regular distances between points at step 3.

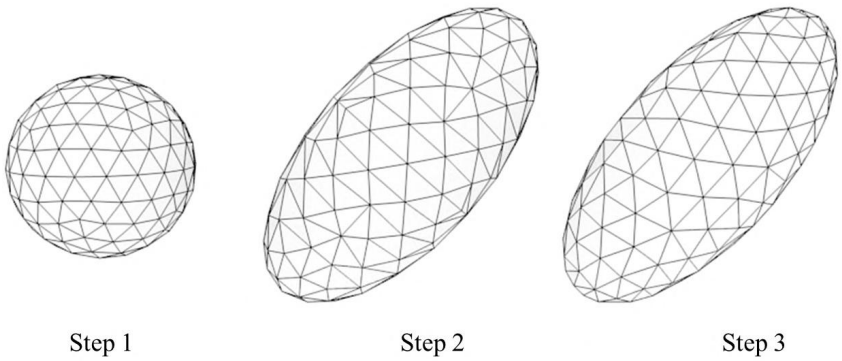

Source: Own elaboration.

The Lagrangian mesh at its final state contains almost equally distributed nodes and is suitable for IBM. The surface area of an ellipsoid is calculated using the approximation from Knud Thomsen[1]:

$$A_s = 4\pi \sqrt[p]{\frac{A^p B^p + A^p C^p + B^p C^p}{3}}, \tag{72}$$

in which $p = 1.6075$. A thorough discussion on area approximations of n-dimensional ellipsoids can be found in (KLAMKIN, 1971; KLAMKIN, 1976)

3.1.2 Gravity-Driven Motion

It must be noticed that, ultimately, IBM only creates a control volume with an imposed boundary velocity. The modeling of a gravity-driven particle must take into account the effects of the fluid inside Lagrangian mesh in particle motion equations. We highlight the difference between an IBM numerical model and a homogeneous solid material of mass m in Figure 16. The particle surface boundary is shown as ∂S and interior of convex geometry as $\partial \forall$. In IBM, there will be fluid "imprisoned" inside Lagrangian mesh, as a water balloon, while the homogeneous material moves with no relative movement in its interior.

Figure 16 – Comparison of (a) IBM control volume and (b) a homogeneous solid particle. In (a) the fluid remains "imprisoned" inside the Lagrangian mesh and its movement has to be compensated from the particle motion equations.

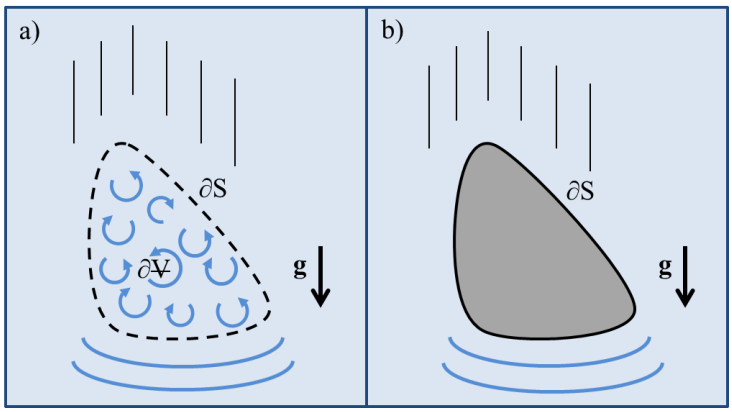

Source: Own elaboration.

Newton's second law dictates the translational motion of a homogeneous particle under

[1] http://www.numericana.com/answer/ellipsoid.htm#thomsen; This approximation has been discussed in sci.math newsgroup by Sigma Xi mathematician David W. Cantrell.

action of gravity represented in Fig 16b for a rigid body as

$$\oint_{\partial S} \boldsymbol{\sigma} \cdot \mathrm{d}\boldsymbol{S} + m\boldsymbol{g} + \boldsymbol{F}_B = m\frac{\mathrm{d}\boldsymbol{U}_c}{\mathrm{d}t}, \tag{73}$$

where $\boldsymbol{U}_c$ is the velocity from mass center $\boldsymbol{X}_c$, gravity acceleration is denoted by $\boldsymbol{g}$ and $\boldsymbol{F}_B$ is the buoyant force. The integral from Equation 73 represents the total force exerted by the stress tensor $\boldsymbol{\sigma}$ on solid-body surface ∂S. The particle angular movement can be described by Euler's rotation equation.

$$\oint_{\partial S} (\boldsymbol{X} - \boldsymbol{X}_c) \times (\boldsymbol{\sigma} \cdot \mathrm{d}\boldsymbol{S}) = \boldsymbol{I}\frac{\mathrm{d}\boldsymbol{\Omega}}{\mathrm{d}t} + \boldsymbol{\Omega} \times (\boldsymbol{I}\boldsymbol{\Omega}), \tag{74}$$

where $\boldsymbol{\Omega}$ is particle's angular velocity and $\boldsymbol{I}$ the diagonal inertia matrix relative to solid-body principal axes. Present work simulations of a rigid body using IBM considers that the opposite forces $(-\boldsymbol{f}\Delta b\Delta A)$, in conjunction with the change of momentum from the fluid contained in $\partial\forall$, must account for the first term in Equation 73, so

$$\oint_{\partial S} \boldsymbol{\sigma} \cdot \mathrm{d}\boldsymbol{S} = -\sum_{L_h} \boldsymbol{f}\Delta b\Delta A + \frac{\mathrm{d}}{\mathrm{d}t}\oint_{\partial\forall} \mathrm{d}\boldsymbol{P}, \tag{75}$$

where $\boldsymbol{P}$ is the linear momentum inside $\partial\forall$ and, $\mathrm{d}\boldsymbol{P} = \rho\boldsymbol{u}\mathrm{d}\forall$. Similarly, for the angular momentum of internal fluid $\boldsymbol{L}$, the first term from Euler's equation is written as:

$$\oint_{\partial S} (\boldsymbol{X} - \boldsymbol{X}_c) \times (\boldsymbol{\sigma} \cdot \mathrm{d}\boldsymbol{S}) = \sum_{L_h} \boldsymbol{M} + \frac{\mathrm{d}}{\mathrm{d}t}\oint_{\partial\forall} \mathrm{d}\boldsymbol{L}. \tag{76}$$

In this equation, $\boldsymbol{M} = (\boldsymbol{X} - \boldsymbol{X}_c) \times (-\boldsymbol{f}\Delta b\Delta A)$ and $\mathrm{d}\boldsymbol{L} = (\boldsymbol{X} - \boldsymbol{X}_c) \times (\rho\boldsymbol{u}\mathrm{d}\forall)$. Suzuki and Inamuro (2011) proposed the treatment of internal momentum terms through the use of discrete Lagrangian points $\boldsymbol{X}_{\text{int}}$ inside IBM mesh:

$$\frac{\mathrm{d}}{\mathrm{d}t}\oint_{\partial\forall} \mathrm{d}\boldsymbol{P} = \frac{\mathrm{d}}{\mathrm{d}t}\sum_{\partial\forall} \left[\rho\left(\boldsymbol{X}_{\text{int}}\right)\boldsymbol{u}\left(\boldsymbol{X}_{\text{int}}\right)\Delta\forall\left(\boldsymbol{X}_{\text{int}}\right)\right]; \tag{77a}$$

$$\frac{\mathrm{d}}{\mathrm{d}t}\oint_{\partial\forall} \mathrm{d}\boldsymbol{L} = \frac{\mathrm{d}}{\mathrm{d}t}\sum_{\partial\forall} \left[\boldsymbol{X}_{\text{int}} - \boldsymbol{X}_c\right] \times \left[\rho\left(\boldsymbol{X}_{\text{int}}\right)\boldsymbol{u}\left(\boldsymbol{X}_{\text{int}}\right)\Delta\forall\left(\boldsymbol{X}_{\text{int}}\right)\right]. \tag{77b}$$

In Equations 77a and 77b, $\Delta\forall(\boldsymbol{X}_{\text{int}})$ is the volume associated with each internal node and whose summation must be $\partial\forall$. The density and velocity are both calculated through the

same IBM interpolative process with D_h:

$$\rho\left(\boldsymbol{X}_{\text{int}}\right) = \sum_{\boldsymbol{x}\in E_h} \rho\left(\boldsymbol{x}\right) D_h\left(\boldsymbol{x} - \boldsymbol{X}_{\text{int}}\right) \Delta x^3; \tag{78a}$$

$$\boldsymbol{u}\left(\boldsymbol{X}_{\text{int}}\right) = \sum_{\boldsymbol{x}\in E_h} \boldsymbol{u}\left(\boldsymbol{x}\right) D_h\left(\boldsymbol{x} - \boldsymbol{X}_{\text{int}}\right) \Delta x^3. \tag{78b}$$

The identification of these internal points in three-dimensional convex geometry and association of a $\Delta\forall$ for each position is achieved by tracing divisions inside IBM mesh. Each vector $\boldsymbol{X}_i - \boldsymbol{X}_c$ is associated with a oblique pyramid of base area ΔA with height given by dot product $H = (\boldsymbol{X}_i - \boldsymbol{X}_c) \cdot \boldsymbol{n}\,(\boldsymbol{X}_i - \boldsymbol{X}_c)$, with n being the vector normal to surface, calculated when building the mesh and adjusted after any rotation. The internal points are drawn by dividing each vector $(\boldsymbol{X}_i - \boldsymbol{X}_c)$ in k equally spaced segments cutting planes on pyramidal geometry perpendicular to n, as illustrated in Figure 17. Under the assumption that each portion of the vector $(\boldsymbol{X}_i - \boldsymbol{X}_c)$ can be associated with a $\Delta\forall(\boldsymbol{X}_{\text{int}})$ corresponding to a clipped pyramid, or frustum, of height $\Delta h = H/k$, as in a finite volumes technique, the summation of these $\Delta\forall(\boldsymbol{X}_{\text{int}})$ from all mesh vectors $(\boldsymbol{X}_i - \boldsymbol{X}_c)$ returns total mesh volume.

Figure 17 – Consideration of a convex volume as being a composition of pyramids. The vectors indicating geometry surface are divided, and a frustum is associated with each segment.

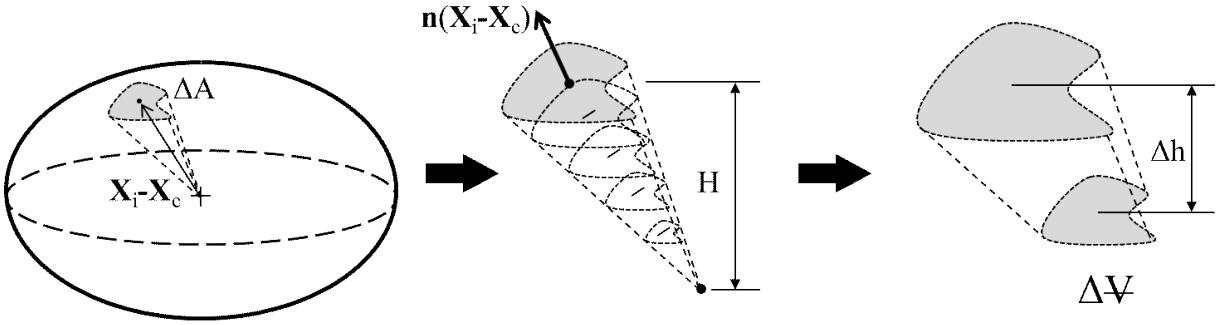

Source: Own elaboration.

The values for $\Delta\forall(\boldsymbol{X}_{\text{int}})$ are defined as the region occupied by the original pyramid, minus the volume of the sliced apex. This reasoning is illustrated in Figure 18.

If the 0^{th} internal point is placed at the center of the convex geometry and the k^{th} ones placed on its surface. For any point in-between, $\Delta\forall^{(i+1)}$ can be written as

$$\Delta\forall^{(i+1)} = \frac{1}{3}\left[\Delta A^{(i+1)}\left(h + \Delta h\right) - \Delta A^{(i)} h\right], \tag{79}$$

Figure 18 – Example of a volume element of a generic point $i+1$ from a single mesh vector associated with a pyramidal geometry.

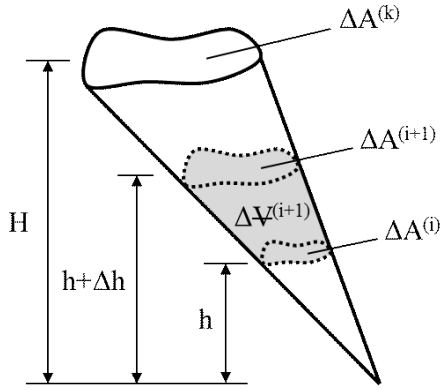

Source: Own elaboration.

where the areas of cross-section and the base are proportional to the squares of their heights (KISELEV, 2008), thus

$$\frac{\Delta A^{(i+1)}}{\Delta A^{(k)}} = \left(\frac{h+\Delta h}{H}\right)^2 \quad ; \quad \frac{\Delta A^{(i)}}{\Delta A^{(k)}} = \left(\frac{h}{H}\right)^2$$

Since $\Delta A^{(k)} = \Delta A$, $h = i\Delta h$ and $\Delta h = H/k$, an expression for the i^{th} volume $\Delta\mathbb{V}^{(i)}$, with $0 \leq i \leq k$, can be found by rearranging Equation 79:

$$\Delta\mathbb{V}^{(i)} = \frac{H\Delta A}{3k^3}\left(3i^2 - 3i + 1\right). \tag{80}$$

This procedure used to compensate for the internal fluid influence does not require storing the positions of internal points at each time-step, since they are drawn from mesh vectors $(\boldsymbol{X}_i - \boldsymbol{X}_c)$. The equations describing particle motion are discretized for a time interval Δt using a finite-difference scheme with a Crank-Nicholson method for all terms except the internal mass compensation, which is discretized only up to first-order in a backward Euler scheme. The evolution of translational and rotational velocities is given by:

$$\boldsymbol{U}_c^{(t+1)} = \boldsymbol{U}_c^{(t)} - \frac{\Delta t}{2m}\sum_{L_h}\left(\boldsymbol{f}^{(t+1)} + \boldsymbol{f}^{(t)}\right)\Delta b\Delta A + \frac{\boldsymbol{P}_{\text{int}}^{(t)} - \boldsymbol{P}_{\text{int}}^{(t-1)}}{m} + \boldsymbol{g}\Delta t + \frac{\boldsymbol{F}_B\Delta t}{m}; \tag{81a}$$

$$\begin{aligned}\boldsymbol{\Omega}^{(t+1)} = \boldsymbol{\Omega}^{(t)} + \boldsymbol{I}^{-1}\Bigg\{\sum_{L_h}\frac{\left(\boldsymbol{M}^{(t+1)} + \boldsymbol{M}^{t}\right)}{2} + \frac{\boldsymbol{L}_{\text{int}}^{(t)} - \boldsymbol{L}_{\text{int}}^{(t-1)}}{\Delta t} \\ -\frac{1}{4}\left[\left(\boldsymbol{\Omega}^{(t+1)} + \boldsymbol{\Omega}^{(t)}\right)\times\boldsymbol{I}\left(\boldsymbol{\Omega}^{(t+1)} + \boldsymbol{\Omega}^{(t)}\right)\right]\Bigg\}\Delta t,\end{aligned} \tag{81b}$$

where $\boldsymbol{P}_{\text{int}}$ and $\boldsymbol{L}_{\text{int}}$ are the linear and angular momenta of internal fluid, respectively. The central mesh position and its angular displacement $\Delta\theta^{(t+1)}$ are calculated using second-order Crank-Nicholson method:

$$\boldsymbol{X}_c^{(t+1)} = \boldsymbol{X}_c^{(t)} + \frac{\Delta t}{2}\left(\boldsymbol{U}_c^{(t+1)} + \boldsymbol{U}_c^{(t)}\right); \tag{82a}$$

$$\Delta\theta^{(t+1)} = \frac{\Delta t}{2}\left\|\boldsymbol{\Omega}^{(t+1)} + \boldsymbol{\Omega}^{(t)}\right\|. \tag{82b}$$

Knowing the values for $\boldsymbol{X}_c^{(t+1)}$ and $\Delta\theta^{(t+1)}$, all mesh nodes are updated with rotation being computed using quaternion operation:

$$\boldsymbol{X}_i^{(t+1)} = \boldsymbol{X}_c^{(t+1)} + q\left(\boldsymbol{X}_i^{(t)} - \boldsymbol{X}_c^{(t)}\right)q'. \tag{83}$$

Introduced by William R. Hamilton in 1843, the quaternion is a hypercomplex number that can be represented in $\mathbb{R}^4$ as the sum of a scalar and vector parts, this is written as (KUIPERS, 1999):

$$q = q_0 + \boldsymbol{q}, \tag{84}$$

where q_0 corresponds to a real number and $\boldsymbol{q} = (q_0,q_1,q_2)$ is the vector part from the quaternion. This category of numbers forms a non-commutative ring, meaning that non-commutativity of division the only property differing from a field (KUIPERS, 1999). The product of two quaternions q and p is given by:

$$pq = p_0q_0 - \boldsymbol{p}\cdot\boldsymbol{q} + p_0\boldsymbol{q} + q_0\boldsymbol{p} + \boldsymbol{p}\times\boldsymbol{q}. \tag{85}$$

Defining the conjugate of a quaternion as $q' = q_0 - \boldsymbol{q}$ and as a vector $\boldsymbol{v} \in \mathbb{R}^3$ can simply be treated as a quaternion $q \in \mathbb{R}^4$ whose real part is $q_0 = 0$, a pure quaternion (KUIPERS, 1999), it can be shown that for a pure quaternion $v = 0 + \boldsymbol{v}$ the operation qvq' returns a w that will be a pure quaternion. This is illustrated in Figure 19.

For a quaternion whose norm $|q|^2 = q_0^2 + q_1^2 + q_2^2 + q_3^2 = 1$, in an operation $w = qvq'$, $||\boldsymbol{w}|| = ||\boldsymbol{v}||$. If $\boldsymbol{w} \neq \boldsymbol{v}$, the initial vector went through a rotation, it can be shown that the operation with unitary quaternion

$$q = \cos\left(\frac{\Delta\theta}{2}\right) + \sin\left(\frac{\Delta\theta}{2}\right)\boldsymbol{m}, \tag{86}$$

Figure 19 – Schematic of operation between pure quaternions and its conjugate that can describe the rotation of a pure quaternion.

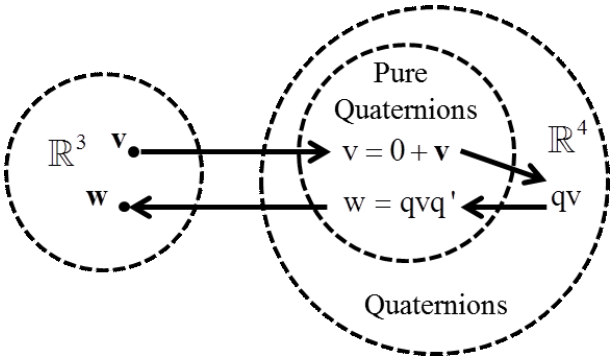

Source: Own elaboration.

implies that $\boldsymbol{w}$ will be the resulting vector of a $\Delta\theta$ rotation of $\boldsymbol{v}$ around the unitary vector $\boldsymbol{m}$ axis (KUIPERS, 1999). That way, the quaternion q from Equation 83 is:

$$q_0 = \cos\left(\frac{\Delta\theta^{(t+1)}}{2}\right); \quad \boldsymbol{q} = \frac{\boldsymbol{\Omega}^{(t+1)} + \boldsymbol{\Omega}^{(t)}}{||\boldsymbol{\Omega}^{(t+1)} + \boldsymbol{\Omega}^{(t)}||}\sin\left(\frac{\Delta\theta^{(t+1)}}{2}\right)$$

The operation qvq' can be written in a matrix-vector multiplication $Q\boldsymbol{v}$, in which

$$Q = \begin{bmatrix} 2q_0^2 - 1 + 2q_1^2 & 2q_1q_2 - 2q_0q_3 & 2q_1q_3 + 2q_0q_2 \\ 2q_1q_2 + 2q_0q_3 & 2q_0^2 - 1 + 2q_2^2 & 2q_2q_3 - 2q_0q_1 \\ 2q_1q_3 - 2q_0q_2 & 2q_2q_3 + 2q_0q_1 & 2q_0^2 - 1 + 2q_3^2 \end{bmatrix}$$

One of the main advantages to work with quaternions rather than Euler angles is that it prevents gimbal lock, the loss of one degree of freedom, which degenerates the three-dimensional rotation system in a two-dimensional space (KOZAK; FRIEDRICH, 2009).

3.2 REGULARIZATION OF COLLISION OPERATOR

Despite the BGK collision operator being very computationally efficient, as τ approaches 0.5, higher-order "ghost" moments arising from an insufficient Hermitian representation can introduce spurious currents into the LBM calculations (MATTILA *et al.*, 2017). Although these higher-order moments have small magnitude, they do spoil the numerical stability. There are many ways around this problem. Present work adopts LB regularization, a procedure developed by Latt and Chopard (2006). It is important to not mistake this technique for the regularization of viscoplastic viscosity in models such as Papanastasiou.

In LBM the flow evolution is described by two major processes. First, is the collision, an event that represents the variations of populations due to collisions and, for the BGK collision

operator, is written from LBE as

$$f_i^* = f_i - \frac{[f_i - f_i^{\text{eq}}]}{\tau} + S_i, \tag{87}$$

and second is the streaming, or propagation, in which post-collision populations f_i^* migrate to a neighbor lattice according to their velocity direction

$$f_i(\boldsymbol{x} + \Delta\boldsymbol{x}, t + \Delta t) = f_i^*(\boldsymbol{x},t). \tag{88}$$

By rewriting collision equation in terms of equilibrium and non-equilibrium populations

$$f_i^* = f_i^{\text{eq}} + \left(1 - \frac{1}{\tau}\right) f_i^{\text{neq}} + S_i, \tag{89}$$

it can be identified f_i^{neq} as the source of the mentioned "ghost" moments. To find an expression for $f_i^{\text{neq}} = f_i - f_i^{\text{eq}}$, such that it recovers the proper hydrodynamic moments, the non-equilibrium function is written as a Hermite polynomial expansion up to second-order:

$$f^{\text{neq}}(\boldsymbol{\xi}) = \omega(\boldsymbol{\xi}) \sum_{n=0}^{2} \frac{a^{(n),\text{neq}} \cdot \boldsymbol{H}^{(n)}(\boldsymbol{\xi})}{n!}, \tag{90}$$

where $a^{(n),\text{neq}}$ are the coefficients of the expansion and $\boldsymbol{H}^{(n)}$ is the Hermite polynomial of order n, which is given by (KRÜGER *et al.*, 2017)

$$\boldsymbol{H}^{(n)}(\boldsymbol{\xi}) = (-1)^{(n)} \frac{1}{\omega(\boldsymbol{\xi})} \nabla^{(n)} \omega(\boldsymbol{\xi}), \tag{91}$$

with $\omega(\boldsymbol{\xi}) = \exp(-||\boldsymbol{\xi}||^2/2)/(2\pi)^{3/2}$ being the weight function. The values of Hermite polynomials up to second-order are (MATTILA *et al.*, 2017):

$$H^{(0)} = 1; \quad H^{(1)}_{\alpha\beta} = \xi_\alpha; \quad H^{(2)} = \xi_\alpha\xi_\beta - \delta_{\alpha\beta}$$

As one of the features of Hermite polynomials is their orthogonality, the coefficients $a^{(n),\text{neq}}$ can be obtained from:

$$a^{(n),\text{neq}} = \int f^{\text{neq}} \boldsymbol{H}^{(n)} d\boldsymbol{\xi}. \tag{92}$$

Since the moments of discrete non-equilibrium populations must return the continuous approach:

$$a^{(0),\text{neq}} = \int f^{\text{neq}} d\xi_\alpha = \sum_i f_i^{\text{neq}} = 0; \tag{93a}$$

$$a^{(1),\text{neq}} = \int f^{\text{neq}} \xi_\alpha d\xi_\alpha = \sum_i f_i^{\text{neq}} \xi_{i\alpha} = \frac{1}{c_s} \sum_i f_i^{\text{neq}} e_{i\alpha} = -\frac{\Delta t}{2c_s} F_\alpha; \tag{93b}$$

$$a^{(2),\text{neq}} = \int f^{\text{neq}} \left(\xi_\alpha \xi_\beta - \delta_{\alpha\beta}\right) d\xi_\alpha = \sum_i f_i^{\text{neq}} \xi_{i\alpha} \xi_{i\beta} = \frac{1}{c_s^2} \sum_i f_i^{\text{neq}} e_{i\alpha} e_{i\beta}. \tag{93c}$$

Substituting those and the Hermite polynomials values in Equation 90:

$$f^{\text{neq}} = \omega\left(\boldsymbol{\xi}\right) \left[-\frac{\Delta t}{2c_s} F_\alpha \xi_\alpha + \frac{1}{2c_s^2} \sum_i f_i^{\text{neq}} e_{i\alpha} e_{i\beta} \left(\xi_\alpha \xi_\beta - \delta_{\alpha\beta}\right) \right], \tag{94}$$

since $c_s \boldsymbol{\xi_i} = \boldsymbol{e}_i$. From Gauss-Hermite quadrature rule:

$$\int_{-\infty}^{+\infty} \omega\left(\boldsymbol{\xi}\right) f^{\text{neq}}\left(\boldsymbol{\xi}\right) d\boldsymbol{\xi} = \sum_{i=1}^{n} w_i f^{\text{neq}}\left(\boldsymbol{\xi}_i\right). \tag{95}$$

The regularized non-equilibrium populations f_i^{reg} are then written as:

$$f_i^{\text{reg}} = \frac{w_i}{2c_s^4} \left[\sum_i f_i^{\text{neq}} e_{i\alpha} e_{i\beta} \left(e_{i\alpha} e_{i\beta} - c_s^2 \delta_{\alpha\beta}\right) - c_s^2 \Delta t F_\alpha e_{i\alpha} \right]. \tag{96}$$

Substituting in Equation 89, the collision equation is rewritten as:

$$f_i^* = f_i^{\text{eq}} + \left(1 - \frac{1}{\tau}\right) f_i^{\text{reg}} + S_i. \tag{97}$$

Applying this formulation results in a considerable increase of numerical stability of BGK collision operator (MATTILA *et al.*, 2017), allowing the use of τ values nearer 0.5.

3.3 BOUNDARY CONDITIONS

Boundary conditions are fundamental in fluid dynamics, as they assure unique solutions for partial differential equations. They are a mathematical description of an observed phenomenon and "their number in the direction of each independent variable of a problem is equal to the order of the highest derivative of the governing differential equation in the same direction" (ARPACI, 1966). As LBM describes a fluid flow in terms of populations in a domain also

discretized for velocity space, boundary conditions have to be defined both in space location and velocity direction i. This is well illustrated in Figure 20, where the dotted lines represent unknown populations at boundaries during streaming.

Figure 20 – Unknown populations (represented by dotted arrows at boundaries for a generic domain during streaming.

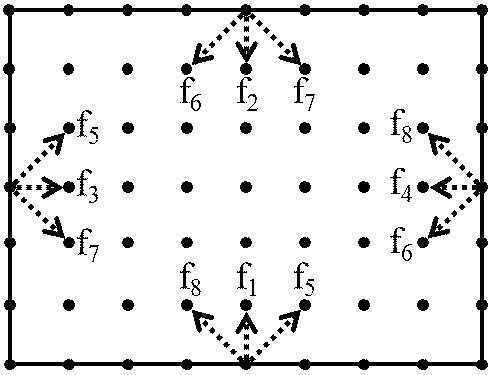

Source: Own elaboration.

This section focus on how to achieve a macroscopically-defined boundary condition in LBM by attributing the proper values to the unknown populations.

3.3.1 Periodic Boundary Condition

Periodic boundary conditions apply to a situation in which is desirable to isolate a repeating flow pattern within a cyclic flow system. This can be attained by assuring that the fluid leaving domain at one boundary simultaneously re-enter the opposite side, as illustrated in Figure 21.

Figure 21 – Example of periodic boundary condition, in which populations leaving one of extremities from computational domain are streamed to the opposite side, attributing values for the unknown populations.

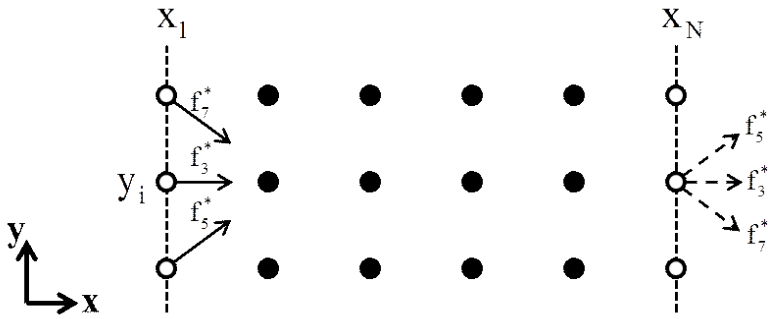

Source: Own elaboration.

As a consequence, periodic boundary conditions conserve mass and momentum at all

times (KRÜGER *et al.*, 2017). For the situation depicted in Fig 21, the unknown populations at (x_1,y_i) can be written as:

$$\begin{cases} f_3\left(x_1,y_i,t+\Delta t\right) = f_3^*\left(x_N,y_i,t\right); \\ f_5\left(x_1,y_i,t+\Delta t\right) = f_5^*\left(x_N,y_{i-1},t\right); \\ f_7\left(x_1,y_i,t+\Delta t\right) = f_7^*\left(x_N,y_{i+1},t\right). \end{cases} \tag{98}$$

Analogously, the unknown populations at x_N are obtained from x_1. In short, the principle of periodic condition is to connect opposite boundaries as if the domain is folded onto itself.

3.3.2 Dirichlet Boundary Condition - Halfway Bounce-Back

As many problems in fluid dynamics deal with no-slip boundary conditions, it is important to find an expression for the unknown populations at boundary $\boldsymbol{x}_b$ that will assure a $\boldsymbol{u}(\boldsymbol{x}_b) = 0$. An alternative is the use of the bounce-back method, whose principle is that populations hitting a wall during streaming are reflected back to their original position (LADD, 1994a), as illustrated in Figure 22.

Figure 22 – Representation of the Halfway Bounce-Back method for no-slip boundary condition. The populations hitting the wall are reflected returning to the same node they left but with opposite velocity, accounting for unknown populations.

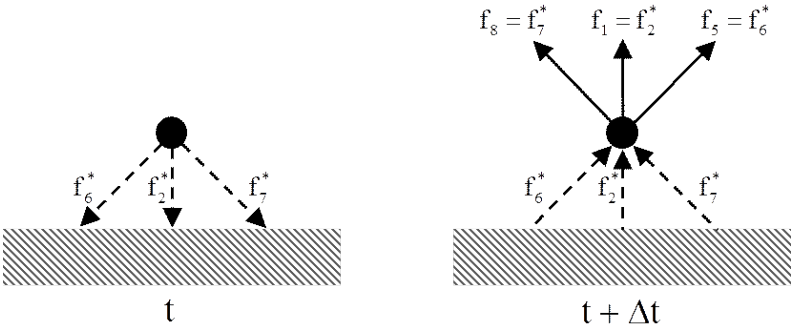

Source: Own elaboration.

In this representation, the wall is located in a $0.5\Delta x$ distance from the boundary node and inversion of velocity occurs at the streaming process, hence unknown populations at propagation are given by (LADD, 1994a):

$$f_{-i}(\boldsymbol{x}_b,t+\Delta t) = f_i^*(\boldsymbol{x}_b,t), \tag{99}$$

where $-i$ stands for the direction opposite to i. This approach implies no flux across the boundary and is known as halfway bounce-back, which is formally second-order accurate (KRÜGER *et al.*, 2017).

The extension to moving walls requires a small correction in Equation 99. Since the populations are no longer hitting a wall at rest, they have to gain or lose an amount of momentum so that the outcome respects Galilean invariance. For a Dirichlet boundary condition of velocity $\boldsymbol{u}_{\text{wall}}$, the unknown populations will be given by:

$$f_{-i}(\boldsymbol{x}_b,t+\Delta t) = f_i^*(\boldsymbol{x}_b,t) - 2w_i\rho_{\text{wall}}\frac{\boldsymbol{e}_i\cdot\boldsymbol{u}_{\text{wall}}}{c_s^2}, \tag{100}$$

in which ρ_{wall} is estimated as the local fluid density at boundary $\rho(\boldsymbol{x}_b)$.

3.3.3 Neumann Boundary Condition

As the present work requires outflow considerations in many simulations, a Neumann boundary condition was also implemented. Though there are better ways to represent outflow boundaries (ABBASSI *et al.*, 2002), the Neumann boundary condition $\partial\boldsymbol{u}/\partial\boldsymbol{n} = 0$ has a relatively easy implementation in LBM. Through a second-order central difference approximation:

$$\frac{\partial\boldsymbol{u}}{\partial\boldsymbol{n}_b}(\boldsymbol{x}_b) = \frac{\boldsymbol{u}(\boldsymbol{x}_b+\boldsymbol{n}_b\Delta x) - \boldsymbol{u}(\boldsymbol{x}_b-\boldsymbol{n}_b\Delta x)}{2\Delta x} = 0. \tag{101}$$

This can be achieved by assuming $f_i^*(\boldsymbol{x}_b+\boldsymbol{n}_b\Delta x) = f_i^*(\boldsymbol{x}_b-\boldsymbol{n}_b\Delta x)$. As $\boldsymbol{x}_b+\boldsymbol{n}_b\Delta x$ goes beyond the computational domain, ghost nodes are employed (JUNK; YANG, 2008), as illustrated in Figure 23.

Figure 23 – Illustration of ghost nodes used for the application of Neumann boundary condition.

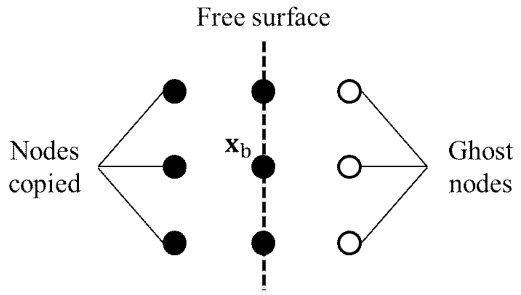

Source: Own elaboration.

By copying the nodes from boundary neighborhood the normal derivative equals zero is assured during streaming, which is performed normally with the ghost nodes.

3.4 BOUNDARY RELOCATION SCHEME

To represent the particle moving in an unbounded domain, the boundaries are dislocated altogether with particle to prevent approach. For a gravity-driven motion, the object may be falling or ascending. The boundary to which particle is traveling towards has zero velocity, and remaining planes have no variation of velocity at normal direction outside the domain. The configurations that can be assumed for both ascending and falling particle situations are illustrated in Figure 24, in which d_{z1} is the distance between the centroid of solid-body and the upwind boundary.

Figure 24 – Schematic of boundary conditions in the computational domain for a particle falling or ascending in quiescent fluid. At the upwind boundary, zero velocity Dirichlet BC is assumed, while Neumann BC is adopted at the remaining boundaries. The solid-body is usually positioned such that $d_{z1} < 0.5N_z$, therefore the simulation domain is mostly dedicated to compute the downstream of the particle's wake.

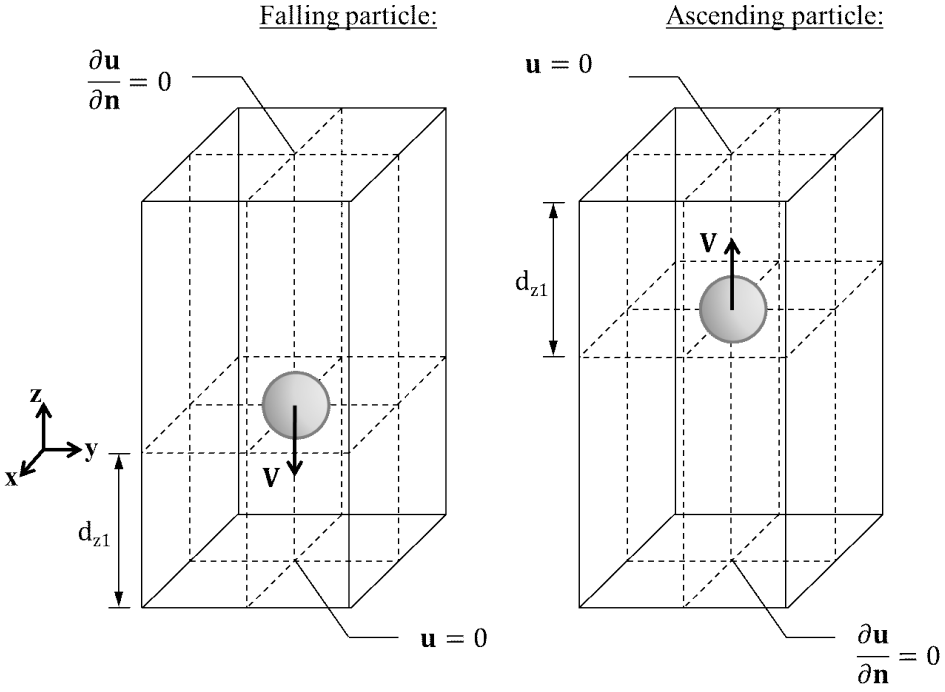

Source: Own elaboration.

The boundary conditions are satisfied through the already described methods. For a DNS limited for a $N_x \times N_y \times N_z$ domain, it is employed a periodic $(N_x+1)\times(N_y+1)\times(N_z+1)$ computational grid. The three extra planes are positioned between the boundaries, separating them. The populations streaming from their nodes do not take part in the simulation, as their values are replaced during the application of the BCs. Figure 25 exemplifies the setup of the computational domain with each block representing a lattice. As illustrated, with the combination

of periodicity and relocation of boundaries, the domain relative to particle's position keeps virtually unaltered.

Figure 25 – Configuration of the computational grid for a boundary relocation scheme. (a) The extra rows outside the simulation domain, shown in light gray, separate the boundaries, represented in dark gray. (b) The boundaries are kept at an almost constant distance from particle's center during the simulation (c) as boundary displacement can only be either zero or Δx.

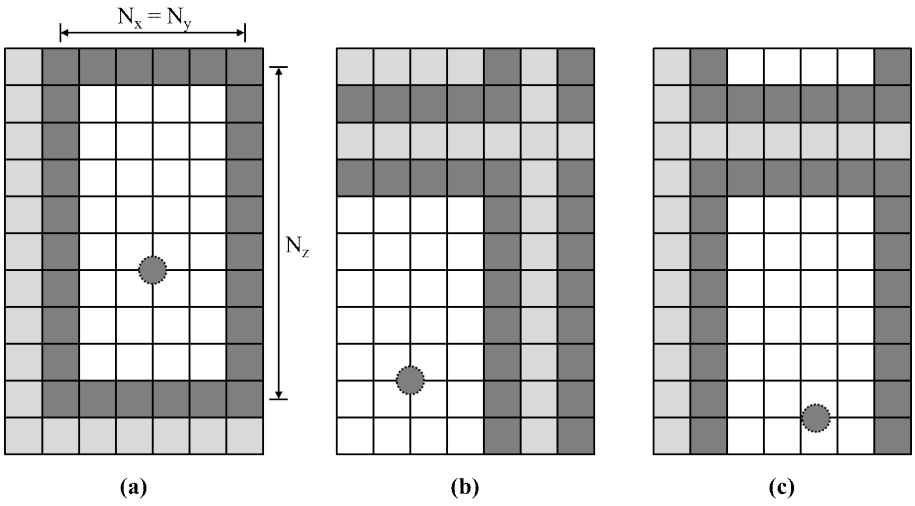

Source: Own elaboration.

When a boundary is relocated in the fixed computational grid, the before inactive nodes from the extra plane are added into simulation confines. The values for populations in these separation planes are copied from the boundaries that particle is moving towards for x-, y-, and z-direction. Velocity and pressure field variations at regions beyond object trajectory are much smaller than they are at downstream and could be disregarded for a sufficiently large domain. Hence, sphere position has to be designed to minimize bottom effects, while keeping a sufficient distance from the outlet. This truncation of the numerical domain is represented in Figure 26, showing how the values at inactive nodes are defined according to the particle's direction of movement. This approach is implemented for x-, y-, and z-direction and edges are also replicated diagonally, in case of oblique displacement of boundaries.

For a square cross-section domain ($N_x = N_y$), the distance between the particle's center and the lateral simulation limits is kept at a value between $0.5(N_x - \Delta x)$ and $0.5(N_x + \Delta x)$. In the vertical direction, the object position d_{z1} might be turned to an appropriate value, depending on the Reynolds number from the simulation. As downstream wake develops for longer distances when Reynolds number increases, it is usually set $d_{z1} < 0.5N_z$.

Figure 26 – Representation of procedure to define the values of populations at the inactive nodes. When the particle's horizontal velocity is positive (Case 1), the inactive nodes replicate the population values from x_{b1}. For a negative horizontal velocity (Case 2), the population values at the inactive nodes are copied from x_{b2}. It is assumed $N_x = N_y$, $d_x = 0.5N_x$, and $d_{z1} \leq 0.5N_z$.

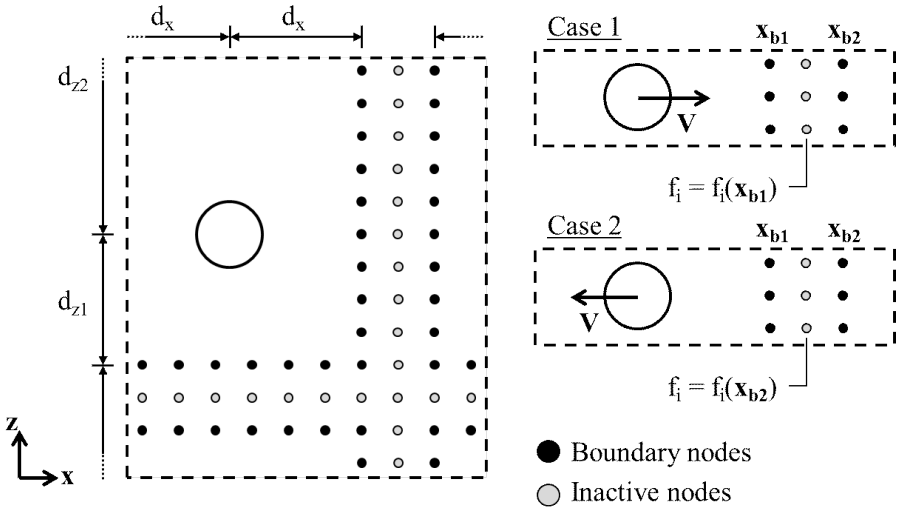

Source: Own elaboration.

3.5 VISCOPLASTIC FLOW IN LBM

As previously suggested, the relaxation time in the LBGK equation does not have to be necessarily constant, which allows for some GNF models to be reproduced in LBM. For those developments, it is convenient to work with LBE in terms of the collision frequency $\omega = 1/\tau$. In a GNF model, the apparent viscosity η is a function of both shear rate $\dot{\gamma}_{\alpha\beta}$ and viscous stress $\tau_{\alpha\beta}$, therefore it is necessary to obtain these variables from the mesoscopic populations. As shown through Chapman-Enskog expansion $\epsilon\Pi^{(1)}_{\alpha\beta} = \tau_{\alpha\beta}$. Assuming that only the first-order terms in ϵ are responsible for the second velocity moment of f_i^{neq}, $\epsilon\Pi^{(1)}_{\alpha\beta} \approx \Pi^{\text{neq}}_{\alpha\beta}$. By rearranging Equation 41c to

$$\Pi_{\alpha\beta} = \left(1 - \frac{\Delta t}{2\tau}\right)\sum_i f_i e_{i\alpha\beta} + \frac{\Delta t}{2\tau}\sum_i f_i^{\text{eq}} e_{i\alpha} e_{i\beta} + \frac{\Delta t}{2}\left(1 - \frac{\Delta t}{2\tau}\right)\left(F_\alpha u_\beta + F_\beta u_\alpha\right), \quad (102)$$

and subtracting $\Pi^{\text{eq}}_{\alpha\beta}$ gives the stress tensor $\sigma_{\alpha\beta}$ as:

$$\tau_{\alpha\beta} = \Pi^{\text{neq}}_{\alpha\beta} = \left(1 - \frac{\Delta t}{2\tau}\right)\left[\sum_i f_i^{\text{neq}} e_{i\alpha} e_{i\beta} + \frac{\Delta t}{2}\left(F_\alpha u_\beta + F_\beta u_\alpha\right)\right]. \quad (103)$$

The regularization of ghost moments is also performed for the stress by using f_i^{reg} instead of f_i^{neq} in Equation 103 (LUGARINI *et al.*, 2020). The shear rate is obtained dividing

$\sigma_{\alpha\beta}$ by the fluid apparent viscosity η from Equation 54, which gives:

$$\dot{\gamma}_{\alpha\beta} = \frac{\omega}{\rho c_s^2}\left[\sum_i f_i^{\text{reg}} e_{i\alpha} e_{i\beta} + \frac{\Delta t}{2}\left(F_\alpha u_\beta + F_\beta u_\alpha\right)\right]. \tag{104}$$

For the representation of the Bingham model with LBM, Lugarini *et al.* (2020) proposed to define the collision frequency operator ω as:

$$\omega = \begin{cases} 0 & |II_{\boldsymbol{\tau}}| \leq \sigma_y^2; \\ \rho c_s^2 / \left[\frac{\Delta t}{2}\rho c_s^2 + \left(\eta_0 + \frac{\sigma_y}{|\dot{\boldsymbol{\gamma}}|}\right)\right] & |II_{\boldsymbol{\tau}}| > \sigma_y^2. \end{cases} \tag{105}$$

For situations in which $\dot{\boldsymbol{\gamma}} = 0$, the value calculated for ω will also be 0, which causes the shear rate in Equation 104 to be zero even if $|II_{\boldsymbol{\tau}}| > \sigma_y$. Therefore, when $\omega = 0$ and $|II_{\boldsymbol{\tau}}| > \sigma_y^2$, the shear rate is computed from a central finite-difference scheme of $\dot{\boldsymbol{\gamma}} = \nabla \boldsymbol{u} + \nabla(\boldsymbol{u})^T$, hence:

$$\dot{\boldsymbol{\gamma}} = \begin{bmatrix} \frac{u(\boldsymbol{x}+\boldsymbol{i}\Delta x) - u(\boldsymbol{x}-\boldsymbol{i}\Delta x)}{\Delta x} & \dots & \dots \\ \frac{v(\boldsymbol{x}+\boldsymbol{i}\Delta x) - v(\boldsymbol{x}-\boldsymbol{i}\Delta x)}{2\Delta x} + \frac{u(\boldsymbol{x}+\boldsymbol{j}\Delta x) - u(\boldsymbol{x}-\boldsymbol{j}\Delta x)}{2\Delta x} & \dots & \dots \\ \frac{w(\boldsymbol{x}+\boldsymbol{i}\Delta x) - w(\boldsymbol{x}-\boldsymbol{i}\Delta x)}{2\Delta x} + \frac{u(\boldsymbol{x}+\boldsymbol{k}\Delta x) - u(\boldsymbol{x}-\boldsymbol{k}\Delta x)}{2\Delta x} & \dots & \dots \end{bmatrix}, \tag{106}$$

where $\boldsymbol{i}$, $\boldsymbol{j}$, $\boldsymbol{k}$ are the unit vectors in the x-, y- and z-directions, respectively. As viscoplasticity is expected to solve the Stokes paradox (HEWITT; BALMFORTH, 2018), it seems more appropriate to adopt the zero velocity bounce-back BC at all boundaries for the representation of particle motion instead of applying Neumann BC at the downwind and lateral boundaries.

3.6 ALGORITHM SUMMARY

The first part of the algorithm consists in the design of IBM mesh from the determined parameters and positioning of the particle and boundaries. In the Eulerian grid populations are initially assumed to be equal f_i^{eq} for a uniform quiescent fluid ($\boldsymbol{u} = 0$ and $\rho = 1$). Linear and angular velocities from the particle are also assumed to be null at the initial instant. At each time step, it is first calculated the values of t, $\boldsymbol{P}_{\text{int}}^{(t)}$, and $\boldsymbol{L}_{\text{int}}^{(t)}$. Then, an iterative process with interpolation of velocity field into Lagrangian mesh and spreading of forces in Eulerian grid is conducted. After 6 iterations, which was found to be sufficient for a velocity deviation $L_1 < 10^{-3}$, the values of $\boldsymbol{U}_c^{(t+1)}$ and $\boldsymbol{\Omega}_c^{(t+1)}$ are obtained. Afterward, collision/streaming from LBM is executed, boundary nodes are copied to inactive planes. At the end, particle and boundaries

positions are updated and simulation advances to the next time step. A summary of the formulated algorithm is shown in a flowchart at Flowchart 1.

Flowchart 1 – Developed algorithm for the simulation of a single-particle settling in an unbounded domain filled with viscoplastic fluid.

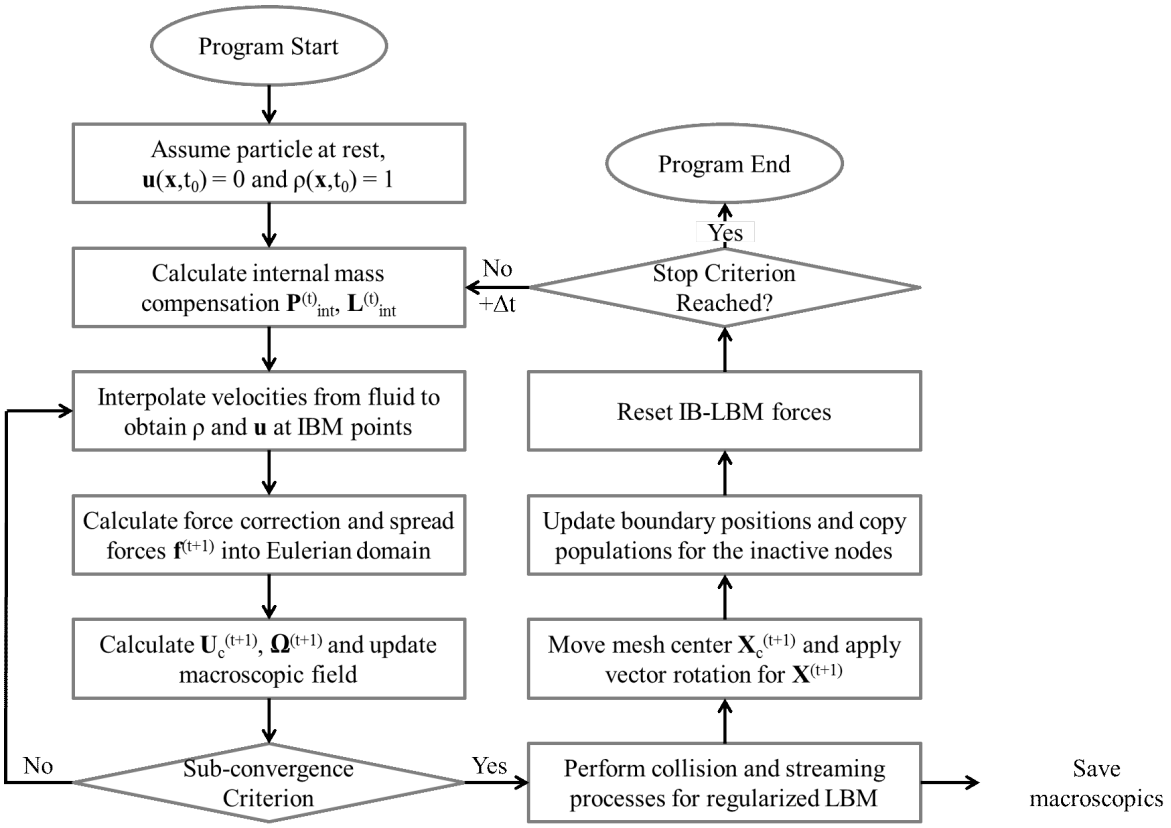

Source: Own elaboration.

The code was written in C/C++ programing language and the processing of simulations was done in parallel with CUDA platform in a GeForce RTX 2070 GPU, 8 GB RAM, allowing for computational domains containing a maximum of approximately 19,360,000 elements for Newtonian and 16,000,000 for viscoplastic settling. When using the whole GPU memory, the typical execution time of a standard settling simulation was around 32 hours for 500,000-time steps, corresponding to 80 million lattice updates per second (MLUPS). It was observed that the implementation of the boundary relocation scheme caused the MLUPS to decrease by approximately 0.92%. The post-processing tool for the rendering of simulation data was ParaView.

3.7 CHAPTER CLOSURE

This chapter detailed the implementation of IBM and LBM for a three-dimensional case of a particle settling in quiescent media. It also presents a meshing technique for generation of ellipsoidal meshes along with the procedure used for the compensation of internal fluid mass for gravity-driven motion in IBM. LBM stability for the evolution of flow is improved with regularization of non-equilibrium populations. A method for calculating the collision frequency that allows for LBM simulations of viscoplastic flow was presented. A boundary relocation scheme, whose purpose is to depict a single particle settling in infinite media, was also introduced. In the next chapter, the proposed scheme is validated for a series of cases.

4 VALIDATION AND VERIFICATION TESTS

This Chapter presents the validation of the numerical methodology, which was conducted by systematically testing the implemented tools. First, LBM D3Q19 velocity set is verified with the simulation of a laminar Hagen-Poiseuille flow in a rectangular cross-section channel (Section 4.1), then, IBM as no-slip boundary condition is validated for uniform flow over a spherical obstacle (Section 4.2). Simulations of a sphere settling in a closed tank and comparison with experimental data are used as validation for translation dynamics of solid-body. The accuracy of rotation dynamics is verified using the analytical solution of an ellipsoidal particle centered at a Couette flow (Section 4.4). At Section 4.5, the boundary relocation scheme for the representation of an unbounded domain is tested for a creeping flow. A sphere rising at Galileo number of 173 is simulated and results are compared with experimental data (Section 4.6). The non-Newtonian Bingham model is first validated for a Poiseuille flow (Section 4.7) and its implementation in viscoplastic settling is verified for a spherical particle (Section 4.8).

4.1 POISEUILLE FLOW IN RECTANGULAR CROSS-SECTION CHANNEL

Boussinesq (1868) derived the solution for the velocity profile of a Hagen-Poiseuille laminar Newtonian flow in a rectangular cross-section channel which is illustrated in Figure 27.

Figure 27 – Illustration of Hagen-Poiseuille flow for a pressure gradient $\mathrm{d}p/\mathrm{d}x$ in $H \times W$ rectangular cross-section channel.

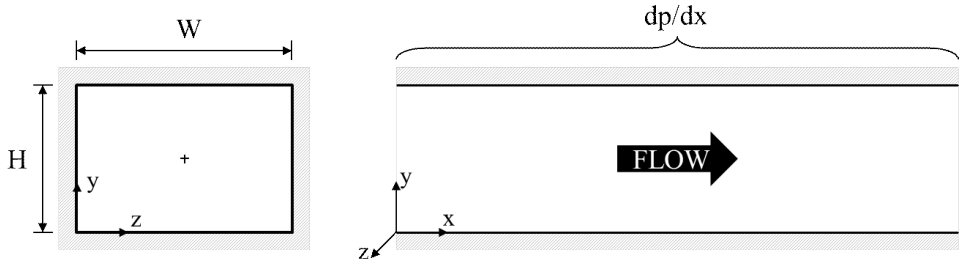

Source: Own elaboration.

For $0 \leq y \leq H$ and $0 \leq z \leq W$, a Newtonian fluid of viscosity μ under a constant pressure gradient $-\mathrm{d}p/\mathrm{d}x$ will have its velocity field $u(y,z)$ only at x-direction and given by:

$$u(y,z) = -\frac{y(H-y)}{2\mu}\frac{\mathrm{d}p}{\mathrm{d}x} + \frac{4H^2}{\mu\pi^3}\frac{\mathrm{d}p}{\mathrm{d}x}\sum_{n=1}^{\infty}\frac{\sin(\alpha_n y)}{(2n-1)^3}\frac{\sinh(\alpha_n z)+\sinh(\alpha_n(W-z))}{\sinh(\alpha_n z W)}, \quad (107)$$

in which, $\alpha_n = (2n-1)\pi/H$. For this configuration, the flow average velocity u_0 is used for scaling and is given by:

$$u_0 = \frac{1}{WH}\left[-\frac{H^3 W}{12\mu}\frac{\mathrm{d}p}{\mathrm{d}x} + \frac{16H^4}{\pi^5\mu}\frac{\mathrm{d}p}{\mathrm{d}x}\sum_{n=1}^{\infty}\frac{1}{(2n-1)^5}\frac{\cosh(\alpha_n W)-1}{\sinh(\alpha_n W)}\right]. \tag{108}$$

The simulations were set assuming periodicity at x-direction and no-slip boundary conditions at the remaining boundaries, the pressure gradient is taken into account from the force density $\boldsymbol{F} = \boldsymbol{i}(-\mathrm{d}p/\mathrm{d}x)$. Simulations are performed for $W/H = 1$ and $W/H = 0.5$, using four grid resolutions for each aspect ratio. The deviation from the analytical solution is evaluated through the quadratic error norm L_2:

$$L_2 = \sqrt{\frac{\sum \left(q_{\text{num}} - q_{\text{ref}}\right)^2}{\sum \left(q_{\text{ref}}\right)^2}}, \tag{109}$$

where q_{num} is the DNS value that will be compared with a reference value q_{ref}. The comparison of L_2 parameter with the analytical solution helps in determining the truncation error order of the numerical model. The domain length is fixed $N_x = 1$. For $W/H = 1/1$, N_y and N_z were varied to 32, 64, 128, and 256. For $W/H = 1/2$, the grid sizes $N_y \times N_z$ were 32×16, 64×32, 128×64, and 256×128. The relaxation time was set $\tau = 3.5$ and $\mathrm{d}p/\mathrm{d}x$ adjusted to maintain $u_0 = 0.01$. The values for L_2 are shown in Graph 1.

Graph 1 – Error decay under grid refinement for two different aspect ratios.

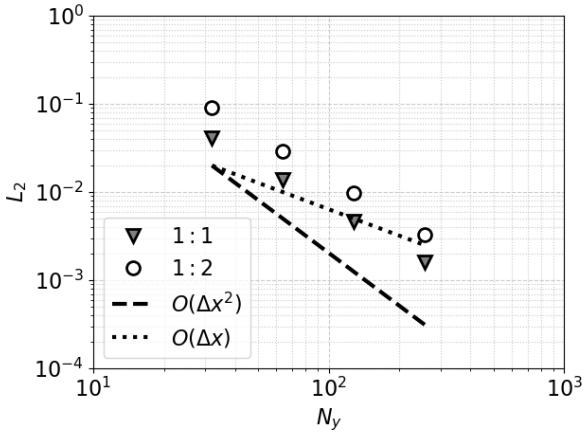

Source: Own elaboration.

A 1.65$^{\text{th}}$-order of accuracy was obtained. The normalized velocity contours of both configurations are shown in Figure 28. After verifying the flow representation with D3Q19 velocity set, validation proceeded to IBM implementation.

Figure 28 – Velocity contours of laminar flow at the rectangular cross-section for (a) $H/W = 1$ and (b) $H/W = 2$.

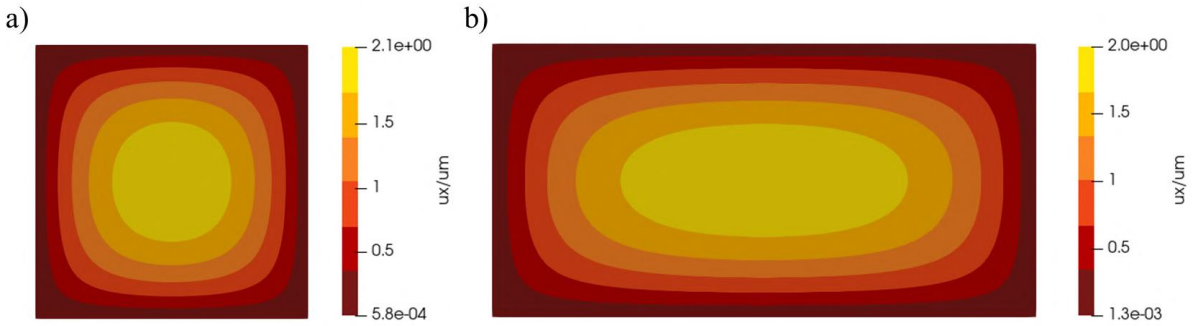

Source: Own elaboration.

4.2 UNIFORM FLOW PAST STATIONARY SPHERE

The IBM is first employed to describe a uniform flow past a spherical object, as illustrated in Figure 29. The fluid leaves inlet with uniform velocity and collides with a stationary rigid sphere.

Figure 29 – Numerical modeling of uniform flow past a spherical object.

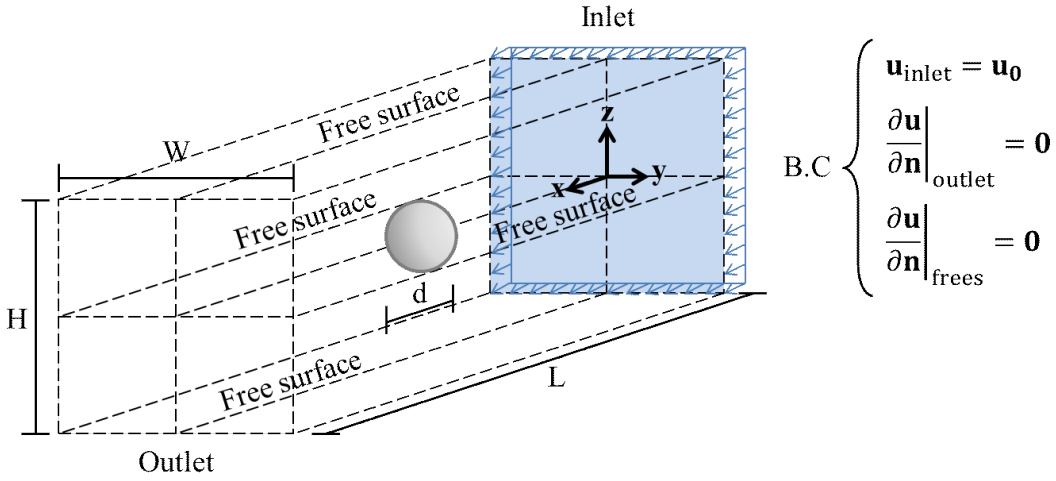

Source: Own elaboration.

The uniform velocity condition at the inlet is attained through Equation 100, at all the other boundaries the Neumann BC is implemented using the ghost nodes technique. A sphere with diameter occupying 30 lattices is positioned at the center of domain, the size of the simulation domain is fixed $180 \times 180 \times 540$ and the simulations were performed for Reynolds numbers of 9.15, 25.5, 37.7 and 118. Frames 1 and 2 compare the pathlines and streamlines of present work with the photographs from Taneda (1956).

Frame 1 – Comparison of present work profiles for wake behind sphere with experimental work from Taneda (1956) at Reynolds numbers of 9.15 and 25.5.

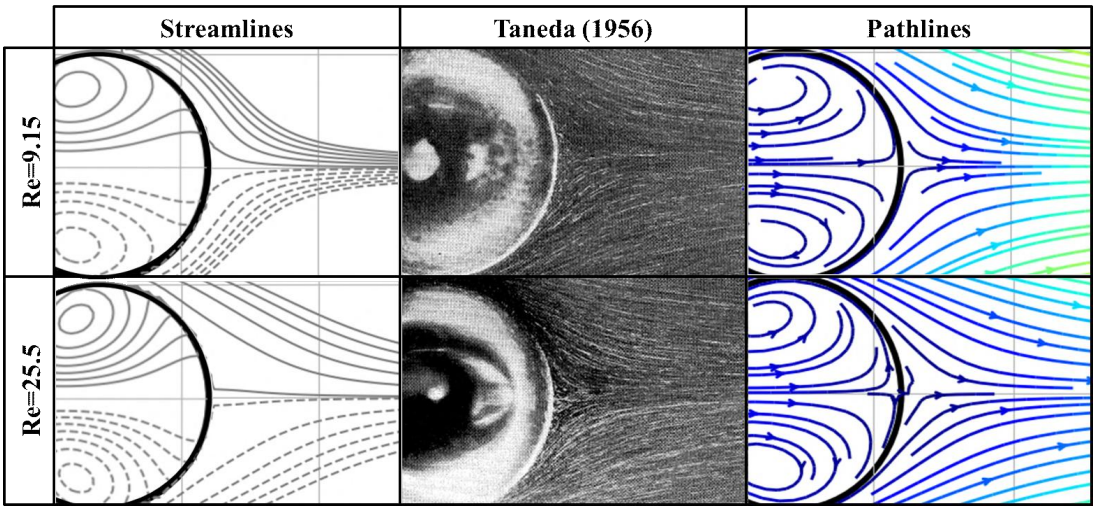

Source: Own elaboration.

Frame 2 – Comparison of present work profiles for wake behind sphere with experimental work from Taneda (1956) at Reynolds numbers of 37.7 and 118.

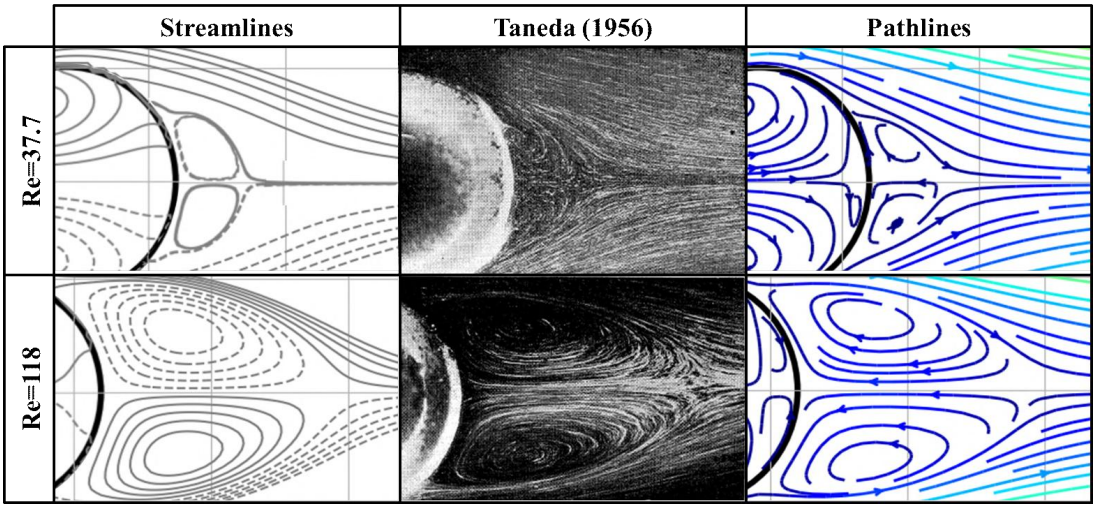

Source: Own elaboration.

Good reproduction of the flow profile from IB-LBM algorithm is seen, its accuracy is also evaluated through measurement of the drag coefficient C_D, calculated taking the summation of Lagrangian forces and internal fluid mass compensation, which gives:

$$C_D = \frac{8}{\rho_0 (u_0 d)^2} \left(-\sum_{L_h} \boldsymbol{f} \Delta b \Delta A + \frac{\mathrm{d}}{\mathrm{d}t} \oint_{\partial \forall} \mathrm{d}\boldsymbol{P} \right). \tag{110}$$

The values of C_D from present work are compared with both Schiller and Naumann

(1935) empirical correlation

$$C_D = \frac{24}{Re}\left(1 + 0.15Re^{0.687}\right), \tag{111}$$

valid for Re $\leq$ 1000, and with Concha and Almendra (1979) correlation, which was developed combining boundary-layer theory and experimental data for pressure distribution and the boundary-layer thickness and is given by:

$$C_D = 0.28\left(1 + \frac{9.06}{Re^{1/2}}\right)^2. \tag{112}$$

This correlation produces reliable results of C_D for $0.1 <$ Re $< 10^4$. A fifth case with Re $= 420$ is also examined, the results for the drag coefficient are shown in Table 2.

Table 2 – Drag coefficients obtained for different Reynolds numbers.

Reynolds number	9.15	25.5	37.7	118	420
Present work	4.973	2.446	1.889	1.067	0.593
Schiller and Naumann (1935)	4.423	2.248	1.792	1.012	0.601
Concha and Almendra (1979)	4.469	2.186	1.716	0.942	0.582
% Deviation	12.4 / 11.3	8.8 / 11.9	5.4 / 10.1	5.4 / 13.3	1.3 / 1.9

Source: Own elaboration.

Good agreement is also shown for drag coefficient results, at Re $=$ 420, there is instability at the downstream wake, shown by the vorticity surfaces of the flow in Figure 30. It can be seen that the flow still keeps a symmetry plane and generates vortex rings at the wake with an aspect that resembles Figure 2.

Figure 30 – Vorticity surfaces for Re $=$ 420, (a) side view and (b) top view.

Source: Own elaboration.

After the implementation of IBM as boundary condition, particle translational motion is validated.

4.3 SPHERICAL PARTICLE SETTLING IN CLOSED TANK

For validation of the particle gravity-driven motion, the setup from Cate *et al.* (2002) experiment of a sphere settling in a tank with square cross-section filled with Newtonian fluid is reproduced. The density of the sphere of diameter $d = 15$ mm was $\rho_p = 1120$ kg/m^3. The fluid's density ρ and viscosity μ were varied as shown in Table 3.

Table 3 – Fluid density and viscosity ranges used in the experiment from Cate *et al.* (2002).

Case	1	2	3	4
ρ(kg/m^3)	970	965	962	960
μ(Ns/m^2)	0.353	0.212	0.113	0.058

Source: Cate *et al.* (2002).

The dimensions of container were $depth \times width \times width = 100 \times 100 \times 160$ mm and the particle's lower part was positioned 120 mm from the tank bottom, as illustrated in Figure 31.

Figure 31 – Representation of experiment configuration in terms of grid size variables.

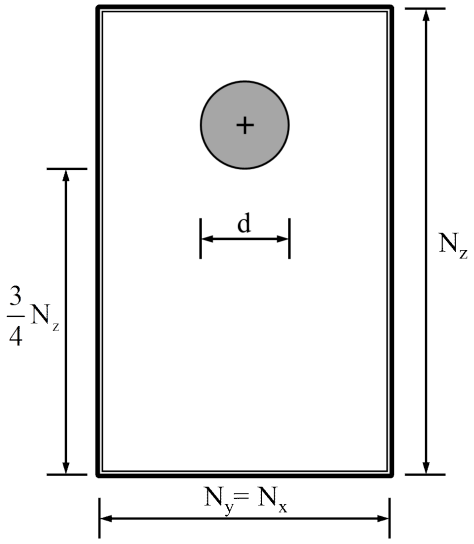

Source: Own elaboration.

No-slip boundary condition is adopted at all boundaries, a Lagrangian mesh of $d = 30$ in a $200 \times 200 \times 320$ computational domain was employed. Being $m^* = \rho_p/\rho$, the LBM parameters were set by fixing a reference velocity $u_0 = \sqrt{(m^* - 1)dg}$ of 0.03 and according to the Galileo number of the experimental setup. A comparison of particle velocity between the present work simulations and the experimental results is shown in Graph 2.

Graph 2 – Comparison of the present work results of vertical velocity obtained for given configurations with experimental data from Cate *et al.* (2002).

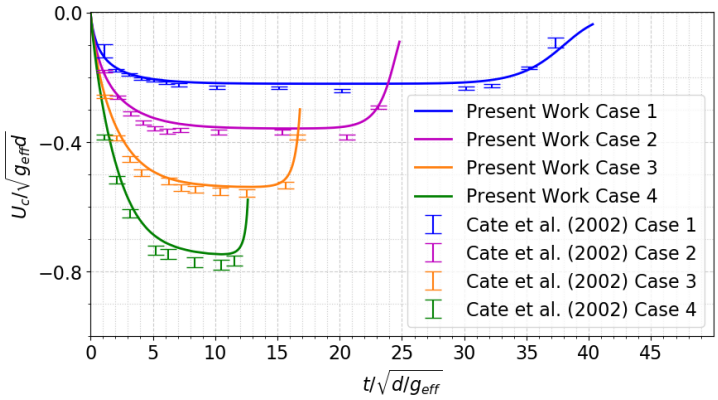

Source: Own elaboration.

Where $g_{\text{eff}} = |m^* - 1|\, g$ is named effective gravity. As shown, there is good consistency of translation dynamics described by the numerical model, the next section proceeds with the validation of solid-body rotation.

4.4 ROTATION OF AN ELLIPSOIDAL PARTICLE IN A COUETTE FLOW

Jeffery (1922) developed a solution for the rotation of an ellipsoidal particle positioned in the center of a creeping Couette flow, as illustrated in Figure 32.

Figure 32 – Ellipsoidal particle centered at $z = 0.5(N_z - 1)$ of a Couette flow. For this configuration an analytical solution can be developed under the consideration of a creeping flow.

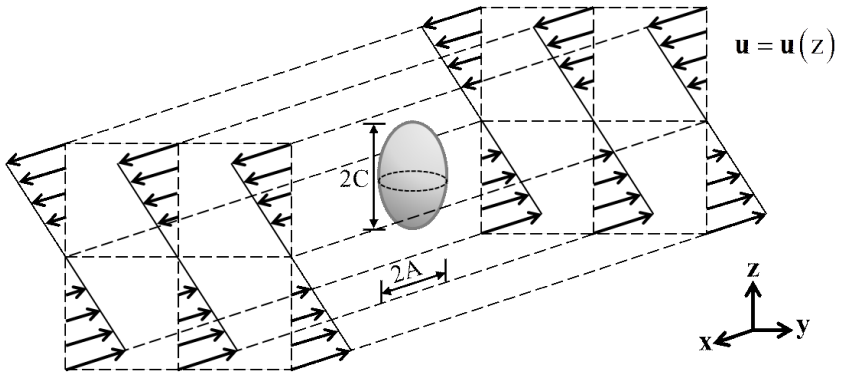

Source: Own elaboration.

For the given situation, Jeffery (1922) solved analytically the periodic rotation $\Omega(\theta,\phi)$ of spheroids ($A = B$), where θ and ϕ are the polar and azimuthal angles, respectively. For $\phi = 0$ the rotation occurs only around y-axis such that $\Omega_y = \Omega_y(\theta)$. That way, the solid-body's angular

velocity is given by:

$$\Omega_y = -\frac{\zeta}{A^2 + C^2}\left(A^2 \sin^2\theta + C^2 \cos^2\theta\right), \tag{113}$$

where ζ is the angular coefficient of the Couette velocity profile. It is then assumed velocities of the same magnitude u_{wall} but opposite direction at top and bottom planes of the domain, and periodicity at the remaining boundaries. The aspect ratio $\chi = C/A$ was fixed 2/3 and the relaxation time $\tau = 9.5$. The adopted Eulerian grid and Lagrangian mesh parameters are specified in Table 4.

Table 4 – Grid and mesh parameters used on the evaluation of error decay under grid refinement.

Simulation	$N_x \times N_y \times N_z$	$A \times B \times C$	u_{wall}
S1	$60 \times 60 \times 60$	$6 \times 6 \times 4$	0.05
S2	$120 \times 120 \times 120$	$12 \times 12 \times 8$	0.025
S3	$240 \times 240 \times 240$	$24 \times 24 \times 16$	0.0125

Source: Own elaboration.

With simulations set at equivalent Reynolds numbers, the quadratic error norm is measured in the periodic regime through the normalized angular velocity $\Omega_y/\Omega_{y,\text{max}}$ of numerical and analytical solutions for one period, Graph 3 shows obtained values for L_2. An $O(\Delta x)$ truncation order approximately was obtained, agreeing with the reports of some available IBM studies (CAIAZZO; MADDU, 2009; ZHU *et al.*, 2011; PENG *et al.*, 2019).

Graph 3 – Quadratic error norm L_2 varying grid resolution. The dashed line shows the first-order truncation error.

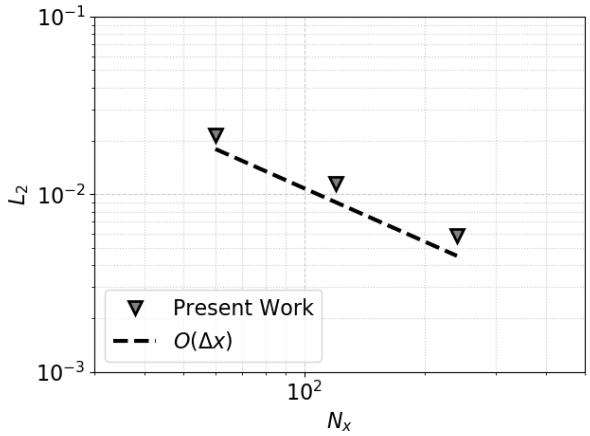

Source: Own elaboration.

Even though high τ values are possible to solve thanks to the regularization of ghost moments (LUGARINI *et al.*, 2020), more accurate results are achieved using small τ. For an

ellipsoid of $\chi = 1/3$ and $A = 24$ in a $180 \times 180 \times 180$ grid, $\tau = 2.6$ and $u_{\text{wall}} = 0.02$ were set, obtaining a $L_2 = 1.19 \times 10^{-2}$. The flow profile and evolution of angular velocity can be seen in Graph 4, in which an excellent agreement with the analytical solution is noted.

Graph 4 – (a) Angular velocity evolution for $\chi = 1/3$ and (b) instantaneous velocity field.

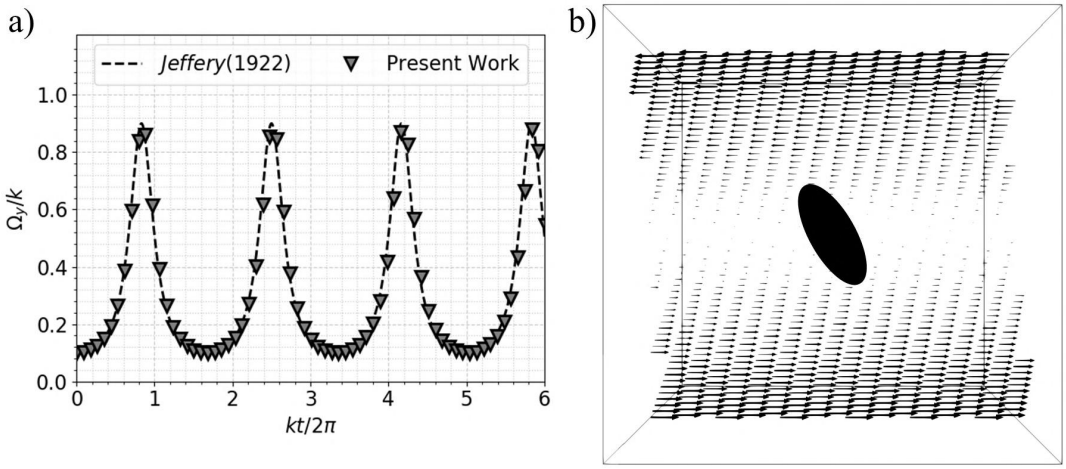

Source: Own elaboration.

Subsequently, $\tau = 1.4$ and $u_{\text{wall}} = 0.01$ were set in a $120 \times 120 \times 120$ grid for an ellipsoidal particle of $\chi = 2$ and $A = 8$. The quadratic error norm was $L_2 = 6.96 \times 10^{-3}$, which results in an angular velocity profile very close to the analytical solution, as shown in Graph 5.

Graph 5 – (a) Angular velocity evolution for $\chi = 2$ and (b) instantaneous velocity field.

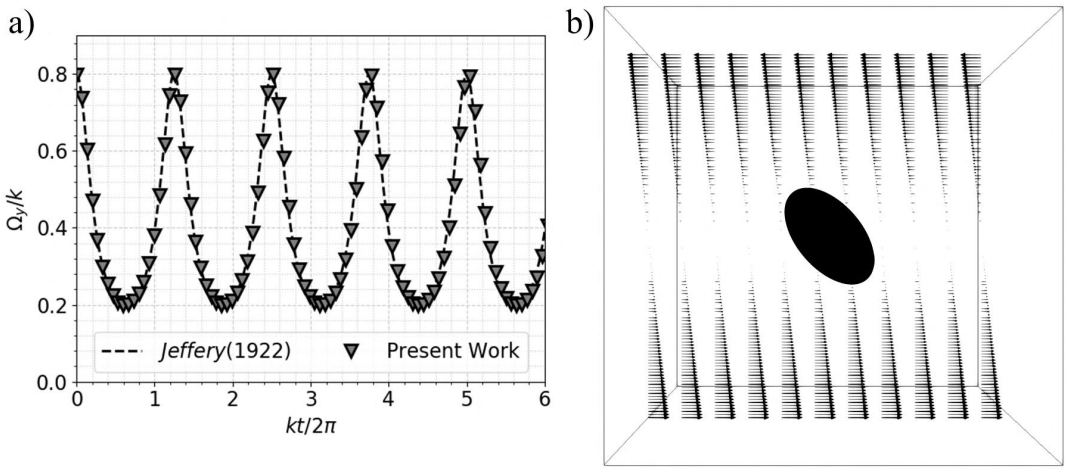

Source: Own elaboration.

With the simulations indicating an adequate representation of solid-body rotation of our algorithm, the present work proceeded with the validation of the boundary relocation scheme.

4.5 SPHERE SETTLING IN CREEPING FLOW

The first assessment of the boundary relocation scheme consists of an investigation of a sphere settling at a creeping flow. For a sufficiently small terminal Reynolds number, an exact solution is possible (DEY *et al.*, 2019). Considering the terminal velocity U_T as the velocity scale in the Reynolds number $\mathrm{Re} = \rho U_T d/\mu$, the exact solution predicts $\mathrm{Re}_T = \mathrm{Ga}^2/18$.

The Galileo number is fixed $\mathrm{Ga} = 0.4$, as it gives $\mathrm{Re}_T = 8.89 \times 10^{-3}$ and assures the creeping flow assumption. A relaxation time $\tau = 6.0$ and a density ratio $m^* = 10$ are fixed, with gravity acceleration term adjusted to each scale through the Galileo number. The particle is positioned at the center of the computational domain with the boundary conditions set for a falling sphere, as illustrated in Figure 33.

Figure 33 – Schematic of the numerical description of a sphere settling at creeping flow. The particle is kept at the center of the domain by the relocation of boundaries and $N_x = N_y$.

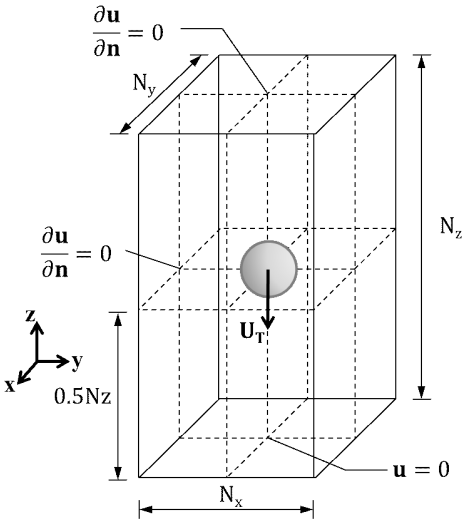

Source: Own elaboration.

The proximity of lateral boundaries in the numerical model carries an associated error. Nevertheless, it is expected that small ratios d/N_x to provide good accuracy for an unbounded domain. A boundary factor $f_b(d/N_x) = U_{T,\mathrm{num}}/U_{T,\mathrm{theo}}$ is defined. This parameter is analogous to the wall factor $f_{\mathrm{wall}}(d/D) = U_W/U_T$ that compares the terminal velocity of a particle settling in a circular tube of diameter D (denoted by U_W) with Stokes solution U_T. An analytical expression of good acceptance for the wall factor $f_{\mathrm{wall}}(d/D)$ at creeping flow was given by Haberman and

Sayre (1958):

$$f_{\text{wall}}\left(\frac{d}{D}\right) = \frac{1 - 2.105(d/D) + 2.0865(d/D)^3 - 1.7068(d/D)^5 + 0.72603(d/D)^6}{1 - 0.75857(d/D)^5}. \quad (114)$$

The parameters $N_z = 500$, $N_x = N_y$, $d = 12$ and $d_{z1} = 0.5N_z$ were fixed. The domain's width was set to 24, 48, 96 and 192, to compare the numerical boundary parameter $f_b(d/N_x)$ with the wall factor for a tube circumscribing the computational domain ($D = \sqrt{2}N_x$). Their comparison is shown in Graph 6a as a function of N_x. The results show that the Neumann boundary condition at lateral boundaries leads to terminal velocities closer to the exact solution than those using a cylindrical wall. The boundary factor converges with grid refinement, verified with simulations varying the Lagrangian mesh diameter to 6, 12 and 24 in a $9 \times 9 \times 17d$ domain. The convergence of the f_b is shown in Graph 6b.

Graph 6 – (a) Comparative chart of wall and boundary factors. By employing Neumann boundary condition, good approximation of the analytical solution is possible without necessity of a vast domain width. (b) Boundary factor behavior with grid refinement. The theoretical wall factor for the same N_x is shown for reference.

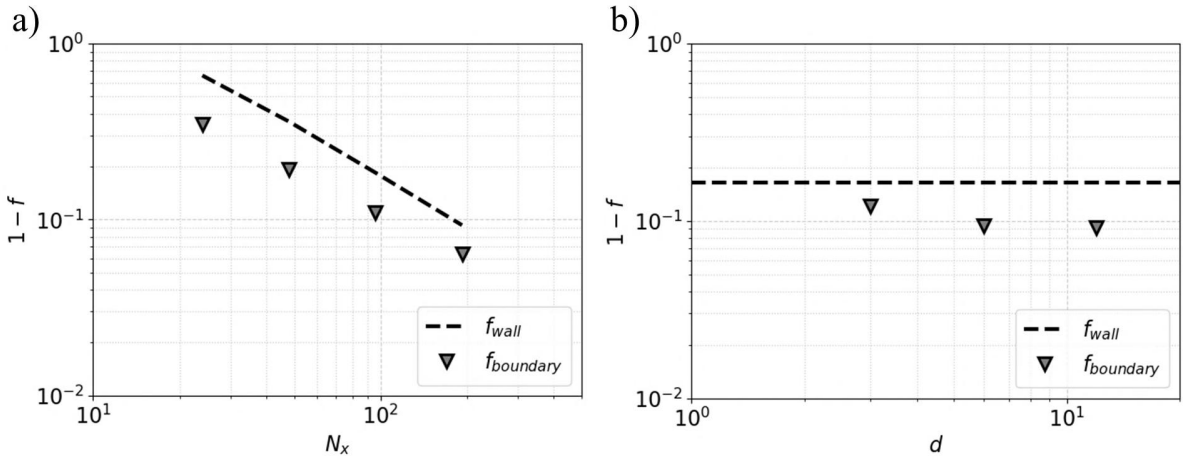

Source: Own elaboration.

The shear stress profile also approaches analytical solution with the increase of resolution, as shown in Graph 7. It is observable that the stress points deviating the furthest from the analytical solution are located at the laterals. Part of the error can be attributed to the lateral boundaries proximity. The analytical solution for the shear stress around the sphere surface for Stokes flow is known to be $\tau_{r\theta} = 3\rho\nu d^{-1}U_T \sin\theta$ (BIRD *et al.*, 1987).

The L_2 values obtained for $d = 6$ and $d = 24$ were 0.364 and 0.126, respectively. As particle motion was purely vertical, the boundary relocation was performed only for z-direction

Graph 7 – $\tau_{r\theta}$ stress profile for resolutions of $d = 6$ and $d = 24$.

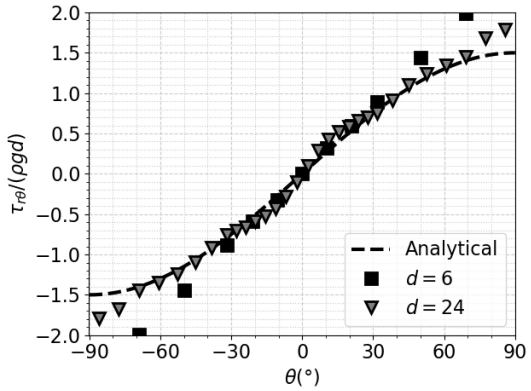

Source: Own elaboration.

each time particle center dislocated a lattice unit. Next case investigates the boundary relocation applied also to the horizontal direction.

4.6 RISING SPHERE

A simulation of a rising sphere with a high Galileo number was performed. Comparisons were made with the experiment of Jenny and Dušek (2004) with $m^* = 0.89$ and Ga $= 173$. In this case, the sphere travels a diagonal trajectory with horizontal velocity behaving as a damped sinusoidal wave centered at its final value. A schematic of employed domain configuration is shown in Figure 34.

Figure 34 – Schematic of the domain for simulation of a particle ascending in a quiescent fluid.

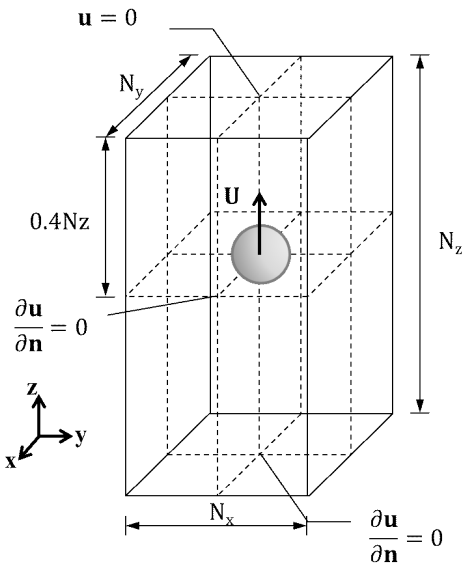

Source: Own elaboration.

A Lagrangian mesh with diameter of 48 lattice units in a $212 \times 212 \times 430$ grid was employed for $\tau = 0.53$ and $d_{z1} = 0.4N_z$. The particle trajectory and its horizontal velocity are shown in Graph 8, in which a good agreement with experimental data is shown despite the small computational domain relative to sphere diameter ($4.4 \times 4.4 \times 9d$).

Graph 8 – Plots of particle trajectory (a) horizontal velocity (a) for a Lagrangian mesh with a diameter of 48 lattice units, $r = \sqrt{x^2 + y^2}$ is the horizontal distance. The present work results are compared with validation experiment from Jenny and Dušek (2004), taking into consideration the time interval in which the particle starts its horizontal motion.

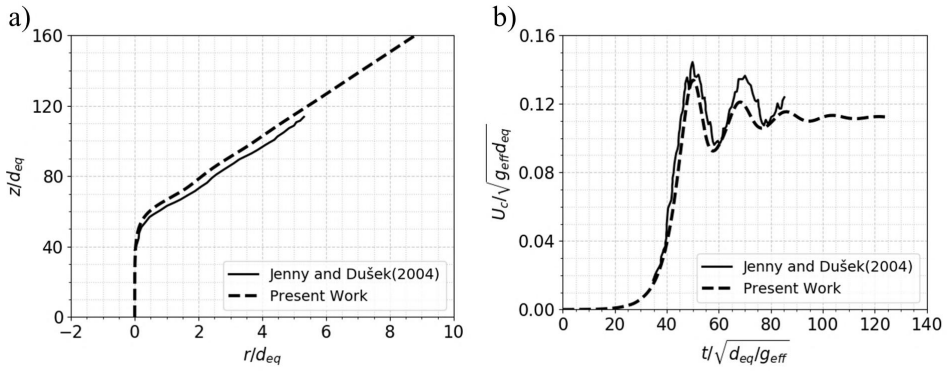

Source: Own elaboration.

This deviation from the vertical trajectory also results in oblique vorticity contours as depicted in Figure 35. The relocation of boundaries is also represented, being noticeable that part of the information regarding downstream wake is lost as the boundaries are relocated, which could be one of the causes for the more dissipative results obtained in the present work. For a total of 200,000-time steps, the boundaries were relocated 426, 136, and 9,507 times at x-, y-, and z-direction, respectively.

Figure 35 – Vorticity contours obtained in the present work at (a) $t/\sqrt{d/g_{\text{eff}}} = 112.63$, (b) $t/\sqrt{d/g_{\text{eff}}} = 120.14$ and (c) $t/\sqrt{d/g_{\text{eff}}} = 127.65$. With time given in lattice-units, the darkened planes represent the boundaries that are relocated during particle motion.

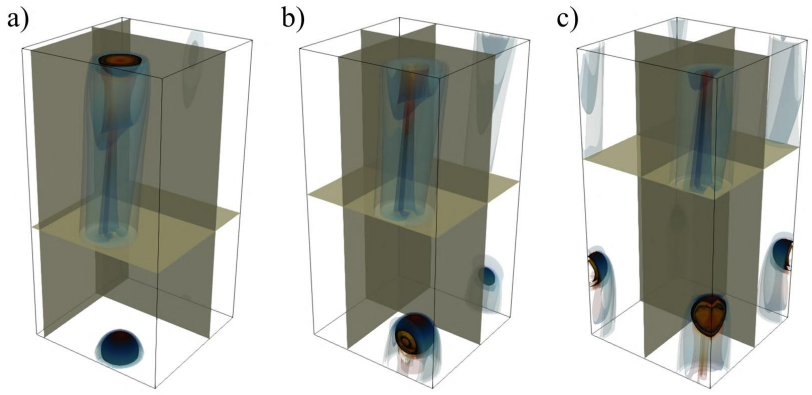

Source: Own elaboration.

4.7 POISEUILLE BINGHAM FLOW BETWEEN PARALLEL PLATES

The implementation of the non-Newtonian Bingham model is validated for a laminar Poiseuille flow between parallel plates distanced by L with a pressure gradient $\partial p/\partial x$, as depicted in Figure 36. As shown, for $-0.5y_0 \leq y \leq 0.5y_0$ the shear stress is lower than σ_y and the fluid move as a rigid plastic material in a region named plug zone. The analytical solution for this flow can be found in (BIRD *et al.*, 1987).

Figure 36 – Representation of a Poiseuille flow with Bingham fluid between parallel plates separated by a L distance. y_0 is the size of plug region.

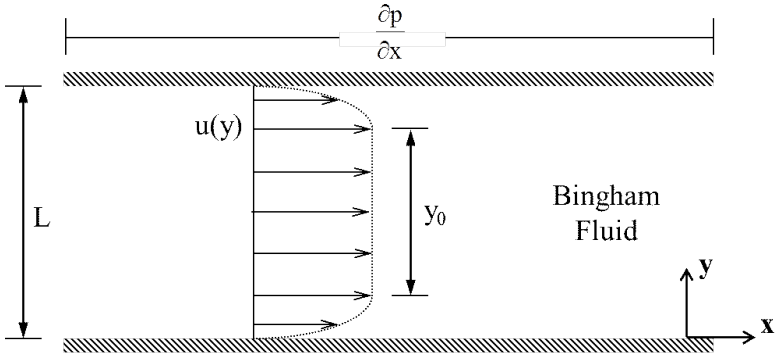

Source: Own elaboration.

Being η_0 the plastic viscosity, two non-dimensional groups are used on the flow description, the Reynolds number $\text{Re} = \rho u_0 L \eta_0^{-1}$ and the Bingham number, given by:

$$\text{Bi} = \frac{\sigma_y}{LF_x}, \tag{115}$$

in which $F_x = -\partial p/\partial x$ is the macroscopic force at x-direction, equivalent to the pressure drop necessary to maintain am average velocity u_0, and is given by:

$$F_x = \frac{12\eta_0 u_0}{L^2\left(1 - 3\text{Bi} + 4\text{Bi}^3\right)}. \tag{116}$$

The size of the unyielded region is given by $y_0 = 2\text{Bi}L$, which implies on the absence of a plug region at $\text{Bi} = 0$, and no flow at $\text{Bi} = 0.5$, as the whole cross-section behaves as a plug. The normalized velocity at the plug region is

$$\frac{u}{u_0} = \frac{3}{2}\frac{(2\text{Bi} - 1)^2}{\left(1 - 3\text{Bi} + 4\text{Bi}^3\right)}, \tag{117}$$

and normalized velocity at the yielded region is

$$\frac{u}{u_0} = \frac{1}{\left(1 - 3\text{Bi} + 4\text{Bi}^3\right)} \left\{ \frac{3}{2} \left[1 - \left(2 \left| \frac{1}{2} - \frac{y}{L} \right| \right)^2 \right] - 6\text{Bi} \left[1 - 2 \left| \frac{1}{2} - \frac{y}{L} \right| \right] \right\}. \tag{118}$$

For the simulation of given flow, periodicity was assumed at both x- and z-direction, and $N_z = N_x = 1$ was fixed. Halfway bounce-back was applied at y-direction boundaries. The value $\eta_0 = 0.5$ was chosen and F_x was set such that $u_0 = 0.01$. The quadratic norm error L_2 was measured for Bi $= 0$, 0.2, and 0.4, and the results are shown in Graph 9

Graph 9 – (a) Error decay under grid refinement for Bi $= 0$, 0.2 and 0.4. (b) Velocity profile with simulation grid of $N_y = 256$. The solid lines are the analytical solution.

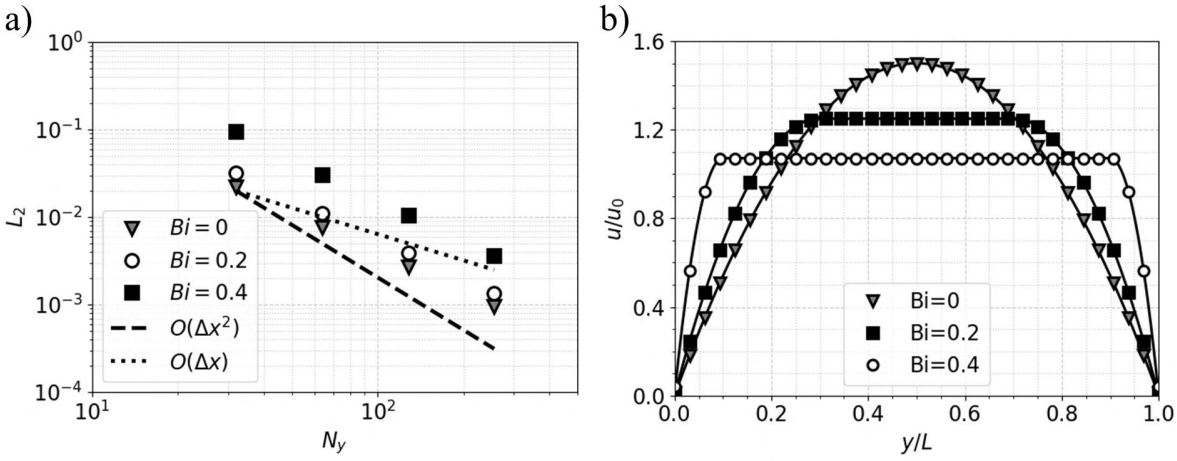

Source: Own elaboration.

It is confirmed that the implementation of the Bingham model does not affect the convergence order of LBM.

4.8 VISCOPLASTIC SETTLING OF SPHERICAL PARTICLE

During the settling of a particle in quiescent viscoplastic fluid, the flow is characterized by a yielded fluid portion that moves with the body and is surrounded by plastic material. To evaluate the plastic effect on the shape of the yielded region and on the motion of the particle, simulations were conducted for a rigid sphere settling at a creeping flow regime. The configuration of the computational domain is illustrated in Figure 37. For simulations with a Bingham fluid, the particle is positioned at the center and halfway bounce-back is applied at all boundaries.

Figure 37 – Computational domain schematic for simulation of viscoplastic settling.

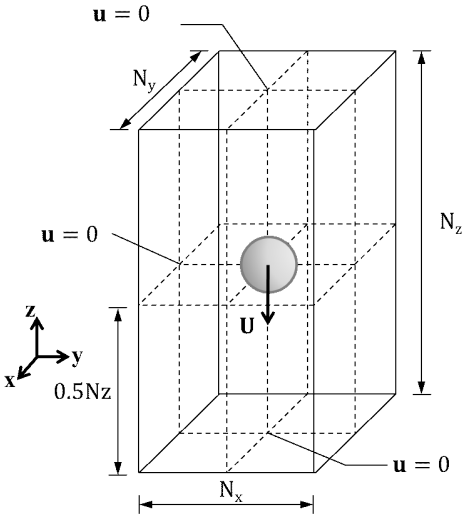

Source: Own elaboration.

The non-dimensional groups used on the flow definition were, the Reynolds number of equivalent Stokes flow $\mathrm{Re}_S = \rho U_S d \eta_0^{-1}$, where $U_S = (\eta_0 \mathrm{Ga}^2)/(18\rho d)$ is the creeping flow terminal velocity of a particle settling in Newtonian fluid of viscosity η_0, and the Bingham number with U_S as the reference velocity

$$\mathrm{Bi}_S = \frac{\sigma_y d}{\eta_0 U_S}. \tag{119}$$

The Reynolds number is fixed $\mathrm{Re}_S = 1$ to match the setup from (BLACKERY; MITSOULIS, 1997; BERIS *et al.*, 1985; YU; WACHS, 2007; DERKSEN, 2011). The mass ratio $m^* = 1.1$ was chosen to match the parameters of DLM/FD numerical work from Yu and Wachs (2007). The Lagrangian mesh had a diameter of 32 lattice units in a $4d \times 4d \times 6d$ ($N_x \times N_y \times N_z$) domain, same proportion adopted by (DERKSEN, 2011). The plastic viscosity was fixed $\eta_0 = 0.5$ and Bi_S was varied to 0.05, 0.21, 0.36, 0.53, 0.60, 0.66, 0.72 and 0.81. Another dimensionless parameter widely adopted is the yield parameter Y_g, which measures the ratio between yield-stress and external forces (BERIS *et al.*, 1985):

$$Y_g = \frac{3\sigma_y}{\rho d g_{\mathrm{eff}}}. \tag{120}$$

For a critical value $Y_g = Y_{\mathrm{crit}}$, there will be no flow and particle will be kept suspended. The value of Y_{crit} for a sphere is usually found to be around 0.14. Being U_T the particle terminal velocity, the non-dimensional groups measured at the simulations were the Stokes drag coefficient

$C_S = U_S/U_T$ and the terminal Bingham number Bi_T

$$\mathrm{Bi}_T = \frac{\sigma_y d}{\eta_0 U_T}. \tag{121}$$

The values obtained for C_S are compared with results available in the literature and are presented in Graph 10, in which the plots are built as a function of Bi_T and Bi_S. It can be seen good agreement with, the experimental results from Ansley and Smith (1967), the variational upper and lower limits calculations from (YOSHIOKA *et al.*, 1971) and the numerical models from Beris *et al.* (1985), Blackery and Mitsoulis (1997), Yu and Wachs (2007) and Derksen (2011).

Graph 10 – Comparison of dimensionless parameters obtained in present work with data available in literature.

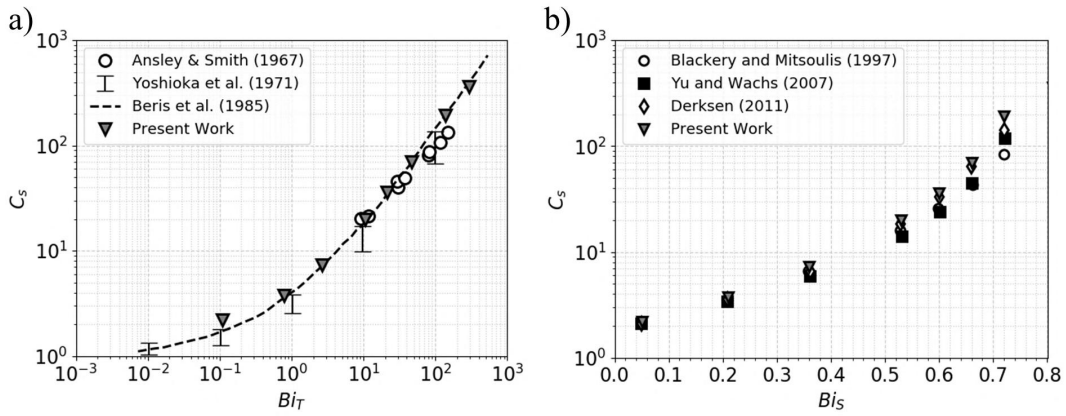

Source: Own elaboration.

For the same time interval, the particle displacement at higher Bingham numbers was much smaller. In Figure 38 the contours of shear rate divided by $\sqrt{g/d}$ are shown for plane xz at $t/\sqrt{d/g} = 130.02$. At that instant, the particle is almost completing a lap in the computational domain for $\mathrm{Bi}_S = 0.05$, while it barely moved for $\mathrm{Bi}_S = 0.53$.

The yielded region also is reduced as the Bingham number increases, and the shapes obtained for the envelopes in the present work were very similar to the predictions from (DERKSEN, 2011), which are shown in Figure 39.

Having a good agreement with literature data at the analyses performed for both Newtonian and viscoplastic cases, the study proceeded with the settling of ellipsoidal particles.

Figure 38 – Envelope shapes at $t/\sqrt{d/g} = 130.02$ for (a) $\mathbf{Bi}_S = 0.05$, (b) $\mathbf{Bi}_S = 0.21$, (c) $\mathbf{Bi}_S = 0.36$ and (d) $\mathbf{Bi}_S = 0.53$.

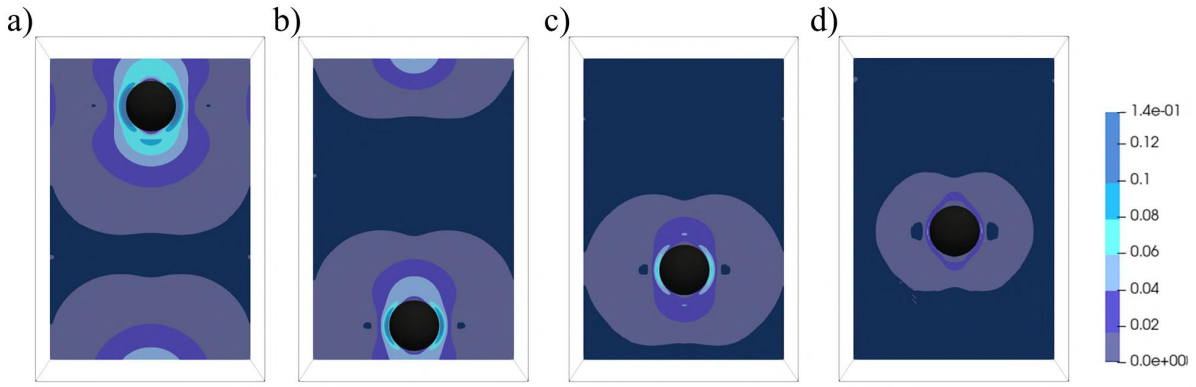

Source: Own elaboration.

Figure 39 – Envelope shapes at different $\mathbf{Bi}_S$.

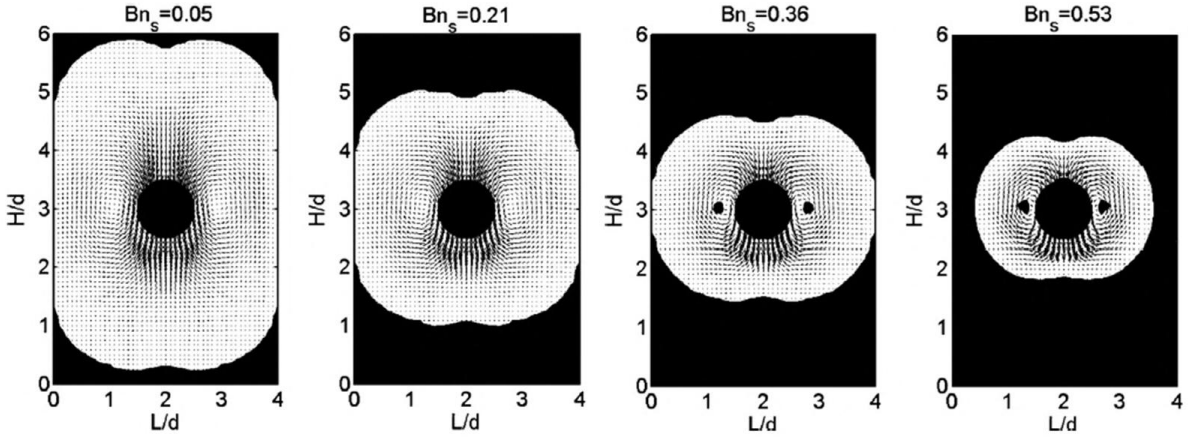

Source: Adapted from Derksen (2011)

4.9 REMARKS ON THE METHODOLOGY

The validation of the algorithm was performed in steps. Good agreement with the analytical solution was shown for a Hagen-Poiseuille Newtonian flow in rectangular cross-section channel. For a uniform flow over a spherical surface, present work results agreed very well with pertinent literature data. The translational motion of solid-body was verified through comparison with experimental results of a sphere settling in a closed tank, to which the performed simulations had a good agreement. The proximity of obtained results with the analytical solution for an ellipsoidal particle in a Couette flow indicated a satisfactory description of solid-body rotation.

The boundary relocation scheme was verified for a Stokes flow, in which it was shown

the domain's width influence on the particle terminal velocity. For the case of an ascending sphere at intermediate Reynolds number, present work had good agreement with experimental data. The Bingham constitutive equation for LBM was successfully implemented without depreciation of the accuracy order, as shown in the solution of a Poiseuille flow between parallel plates. For a particle settling in a viscoplastic fluid, good agreement with pertinent literature data was obtained with an accurate representation of the yielded region.

In summary, the developed scheme can be advantageous over some of the existing methodologies since it has no restrictions of solid-body geometry and has excellent stability. Despite particle motion being implicitly described, flow evolution is fully explicit and can be efficiently parallelized. As the method dismisses viscosity regularization, it achieves great yield surface representation.

5 RESULTS AND DISCUSSION

This Chapter presents the simulations of a oblate spheroid settling at different Galileo numbers (Section 5.1) and the simulations of an ellipsoidal particle settling in Bingham fluid with different configurations (Section 5.2 and Section 5.3).

5.1 SETTLING OF OBLATE SPHEROIDS IN NEWTONIAN FLUID

The domain setup from present work is schematized in Figure 40. The ellipsoid was positioned without inclination and d_{z1} was fixed $0.3N_z$.

Figure 40 – Domain configuration adopted on simulations of oblate spheroid settling.

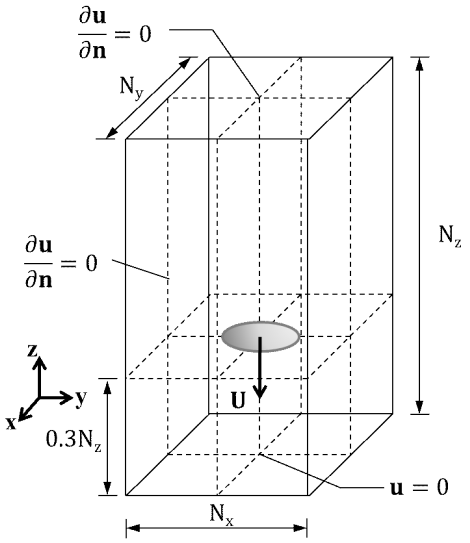

Source: Own elaboration.

The settling of oblate spheroids is performed for aspect ratios $\chi = 1/3$, to which expected trajectories at different Galileo numbers are exemplified in (ARDEKANI *et al.*, 2016). In their work, they made use of large computational domains to approximate solutions in a quiescent Newtonian medium. Though they also used IBM for the representation of solid-fluid interaction, some differences in the outcome are expected because, in addition to our boundary relocation treatment, the internal mass compensation was also performed distinctly. Ardekani *et al.* (2016) considered the fluid had the same velocity and rotation as the solid-body for inertia compensation, as proposed by Uhlmann (2005). The fluid phase was solved with an explicit low-storage three-step Runge-Kutta method of Wray (SPALART *et al.*, 1991) in a $480 \times 480 \times 4000$ grid. Simulations were performed for an oblate spheroid with $\chi = 1/3$, $m^* = 1.14$ and Galileo

numbers of 100, 170, 210 and 250. The Galileo number for an oblate spheroid is calculated from Equation 1 by replacing d with d_{eq}, which is the equivalent diameter of a sphere that has the same volume of ellipsoidal particle.

In their work, Ardekani *et al.* (2016) used a Lagrangian mesh of equivalent diameter of $32\Delta x$. Same value was adopted in present work in a $224 \times 224 \times 386$ computational grid. For Ga $= 100$, τ was set to 0.52 and g was adjusted accordingly. The ellipsoid followed a straight line in our simulation, as well as the example trajectory depicted by Ardekani *et al.* (2016). Graph 11 shows the particle's trajectory.

Graph 11 – Trajectory for oblate spheroid at Ga $= 100$. (a) Ardekani *et al.* (2016) and (b) present work.

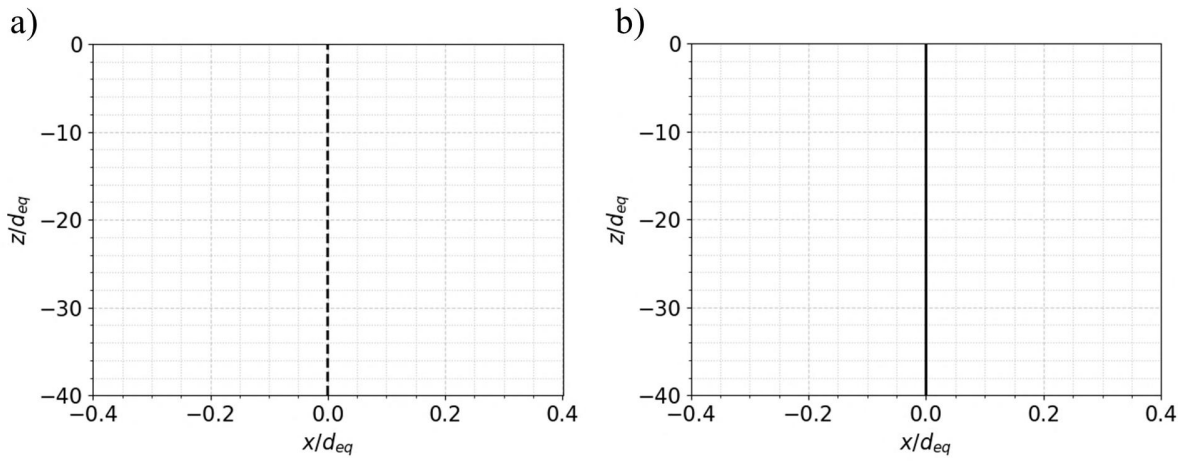

Source: Own elaboration.

At remaining simulations, $\tau = 0.51$ was adopted. The particle travels a periodic pendulum movement when Ga $= 170$, as shown in Graph 12. Qualitative agreement with Ardekani *et al.* (2016) was obtained with almost the same period, despite present work simulations predicting a lateral motion of slightly higher amplitude. As the computational domain has a length of only $12d_{\text{eq}}$, this deviation of the results is possibly due to the information that is lost beyond the simulation domain, which may include the formation of vortexes that could decelerate the horizontal movement from particle, reducing the amplitude of its periodic motion. The differences in the results are expected to be more evident with higher Galileo numbers.

Graph 12 – Trajectory for oblate spheroid at Ga $= 170$. (a) Ardekani *et al.* (2016) and (b) present work.

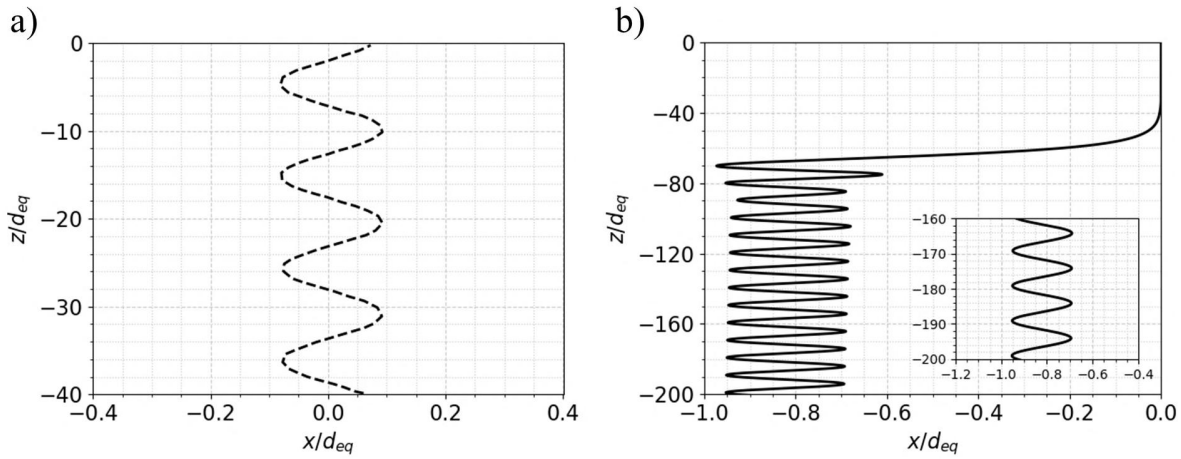

Source: Own elaboration.

With Ga $= 210$, the particle displayed an oscillating oblique motion, as Graph 13 shows. Despite the qualitative agreement with (ARDEKANI *et al.*, 2016), the motion amplitude and inclination show a higher discrepancy than the results with Ga $= 170$.

Graph 13 – Trajectory for oblate spheroid at Ga $= 210$. (a) Ardekani *et al.* (2016) and (b) present work.

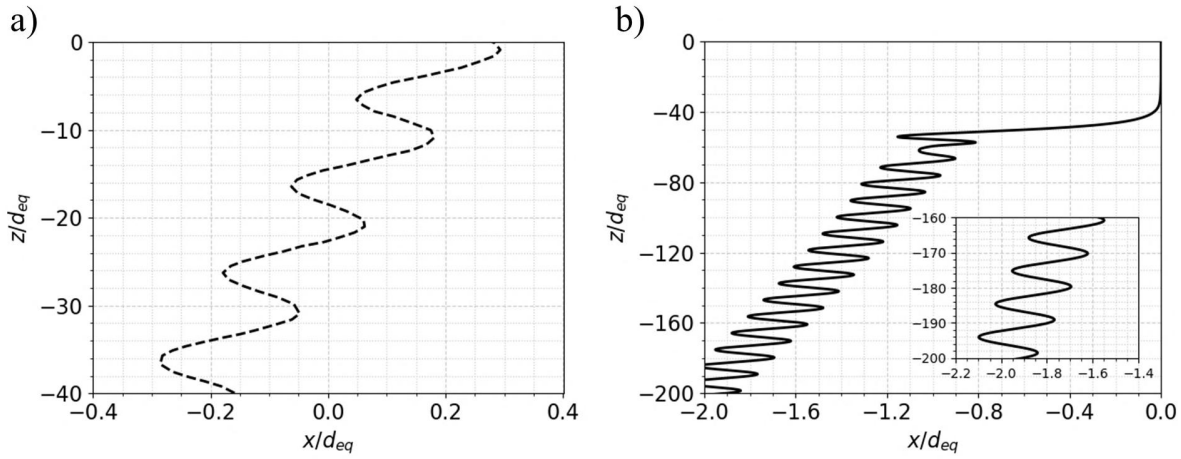

Source: Own elaboration.

The particle displayed chaotic motion with Ga $= 250$ and has its trajectory presented in Graph 14 along with the path exemplified by (ARDEKANI *et al.*, 2016).

Graph 14 – Trajectory for oblate spheroid at Ga $= 250$. (a) Ardekani *et al.* (2016) and (b) present work.

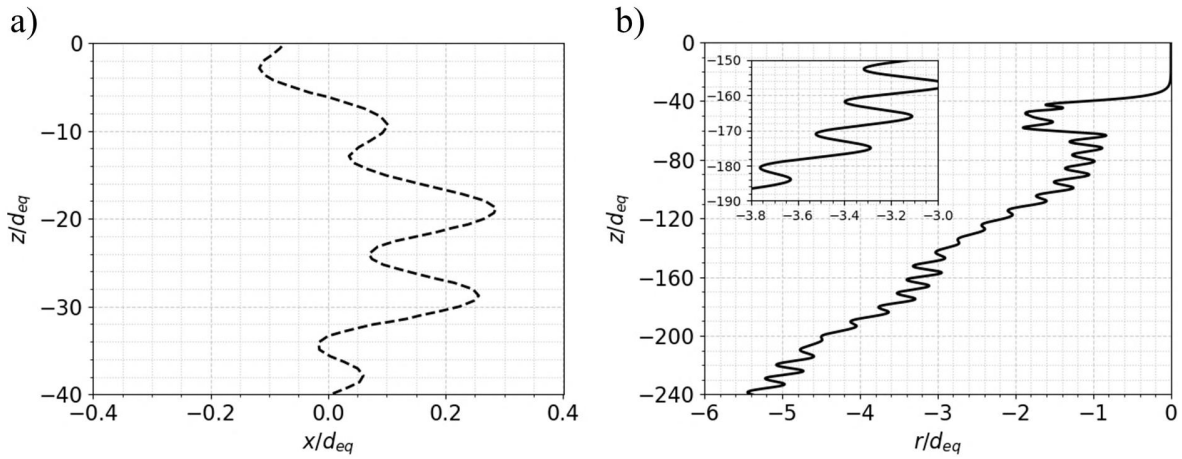

Source: Own elaboration.

The terminal Reynolds numbers $\mathrm{Re}_T = U_T d_{\mathrm{eq}}/\nu$ shown in Graph 15, have great proximity with those from Ardekani *et al.* (2016). At both studies Re_T increases almost linearly with Ga.

Graph 15 – Terminal Reynolds number vs Galileo number. The dashed line represent a proper curve fit.

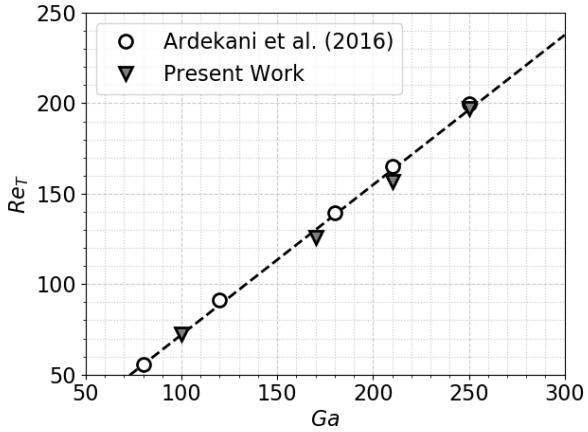

Source: Own elaboration.

The next figures give more details of the particle's motion and vorticity field. The evolution of vertical velocity at each Galileo number is shown in Graph 16.

Graph 16 – Evolution of vertical velocity at (a) Ga $= 100$, (b) Ga $= 170$, (c) Ga $= 210$, (d) Ga $= 250$.

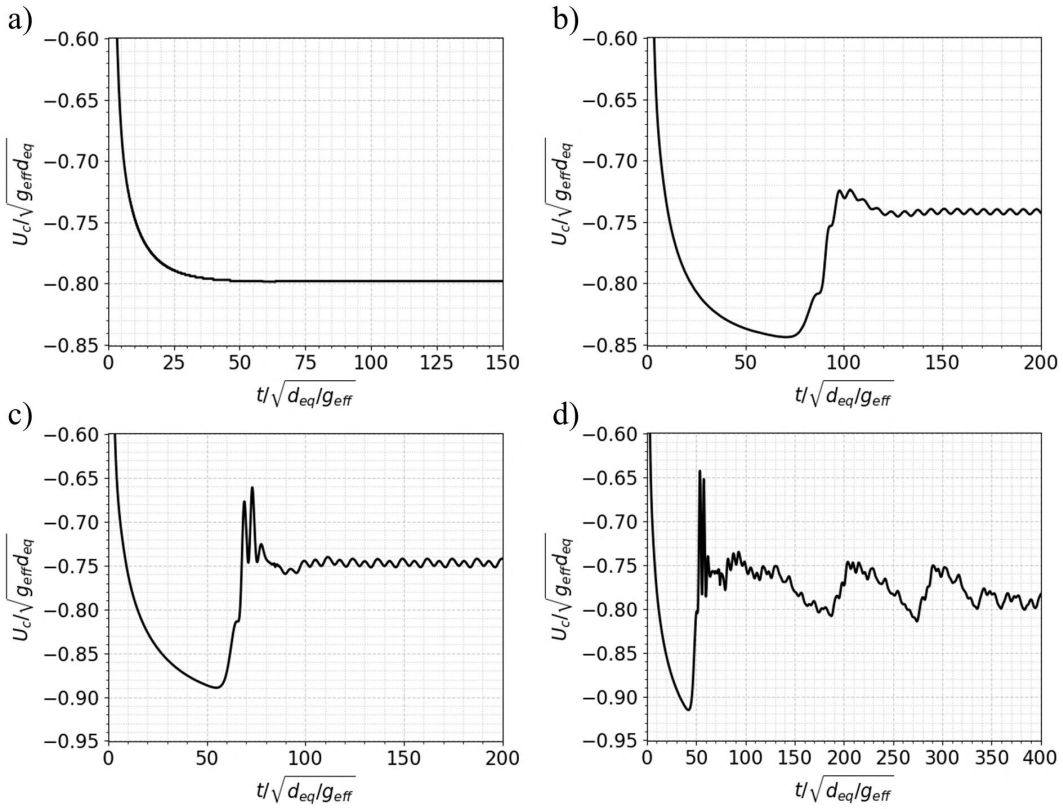

Source: Own elaboration.

With Ga $= 100$, the particle reaches its terminal velocity and assumes a steady motion, demanding the use of boundary relocation scheme only for the vertical direction, as depicted in Figure 41.

Figure 41 – Vorticity contours obtained in the present work with Ga $= 100$ at (a) $t/\sqrt{d_{eq}/g_{eff}} = 52.08$, (b) $t/\sqrt{d_{eq}/g_{eff}} = 58.59$, and (c) $t/\sqrt{d_{eq}/g_{eff}} = 65.10$.

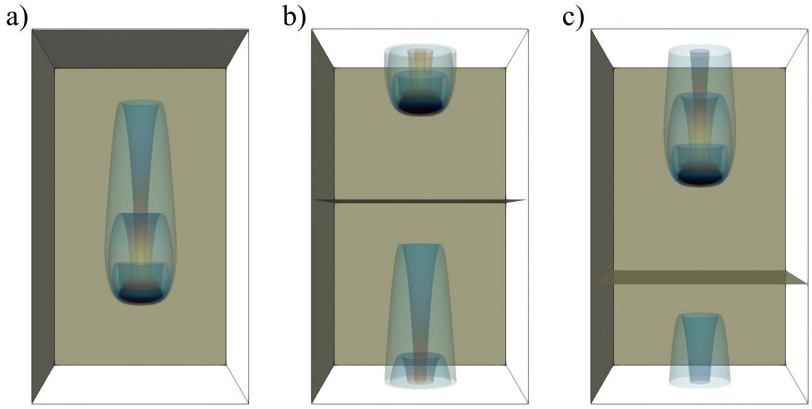

Source: Own elaboration.

With Ga $= 170$, the particle accelerates vertically up to a maximum velocity that

reduces as solid-body starts its lateral motion. The horizontal and angular velocities of the ellipsoid are shown in Graph 17.

Graph 17 – (a) Horizontal and (b) angular velocities obtained in the present work with Ga $= 170$.

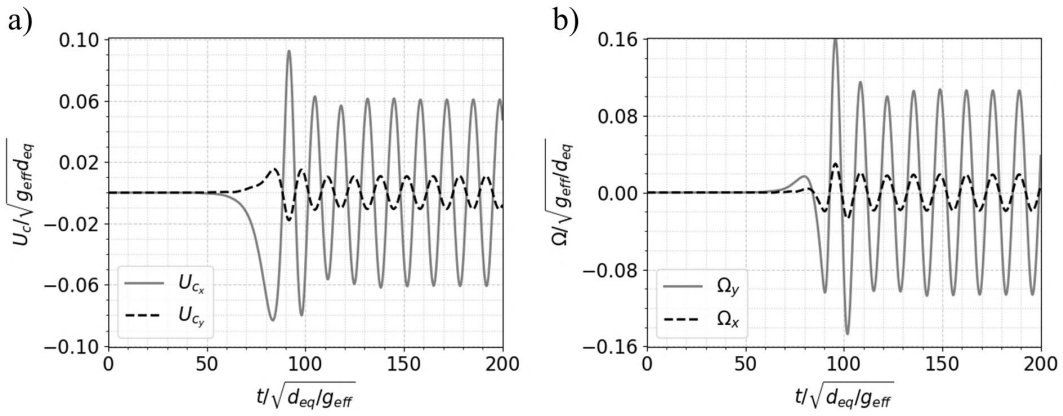

Source: Own elaboration.

The particle exhibits a periodic motion at y-direction and amplitude lower than unity, and therefore, the relocation of boundaries is only required at x-, and z-direction, as illustrated in Figure 42.

Figure 42 – Vorticity contours obtained in the present work with Ga $= 170$ at (a) $t/\sqrt{d_{eq}/g_{eff}} = 83.01$, (b) $t/\sqrt{d_{eq}/g_{eff}} = 88.54$, and (c) $t/\sqrt{d_{eq}/g_{eff}} = 94.08$.

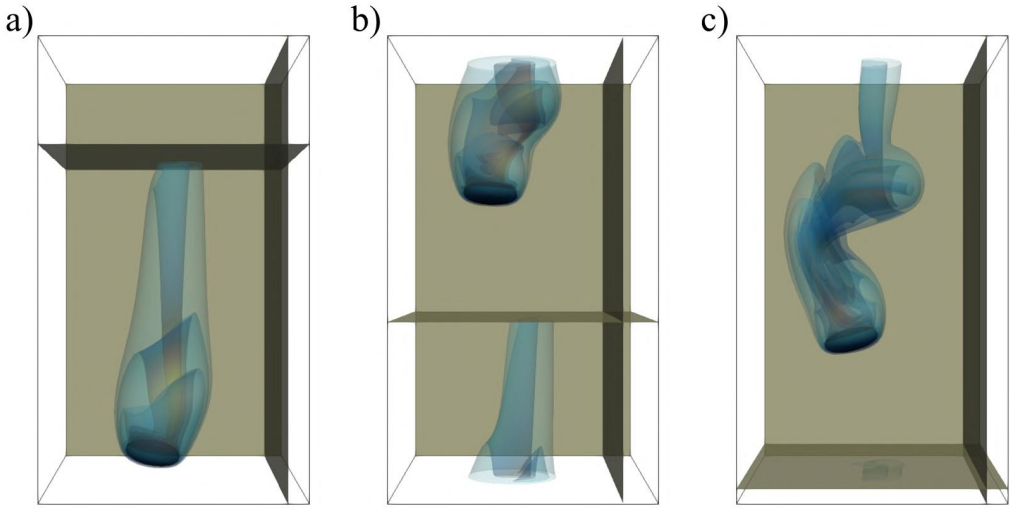

Source: Own elaboration.

When Ga $= 210$, the particle experiences accentuated deceleration as it starts moving laterally, eventually reaching a periodic state, as shown by the plots of angular and horizontal velocities in Graph 18.

Graph 18 – (a) Horizontal and (b) angular velocities obtained in the present work with Ga $= 210$.

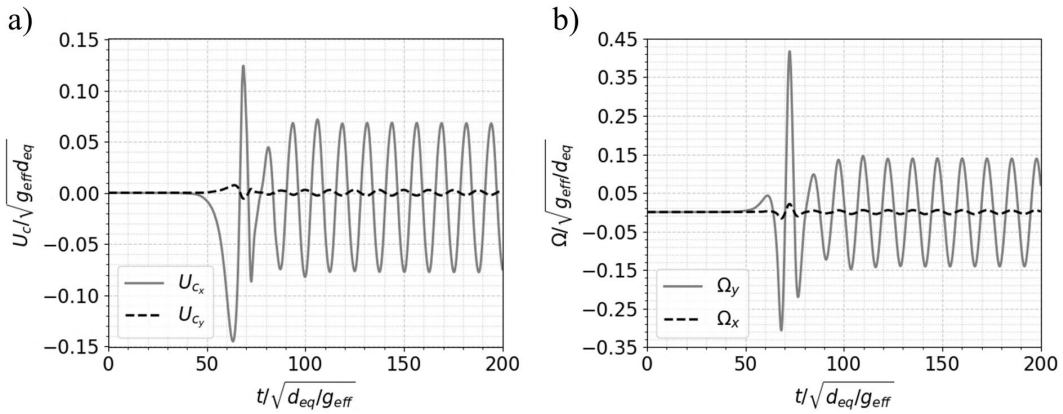

Source: Own elaboration.

In this simulation, the periodic motion at y also has amplitude lower than unity, and boundary relocation is only used at x- and z-direction. The vorticity contours and positions of boundaries at different instants are depicted in Figure 43.

Figure 43 – Vorticity contours obtained in the present work with Ga $= 210$ at (a) $t/\sqrt{d_{eq}/g_{eff}} = 68.36$, (b) $t/\sqrt{d_{eq}/g_{eff}} = 75.20$, and (c) $t/\sqrt{d_{eq}/g_{eff}} = 82.03$.

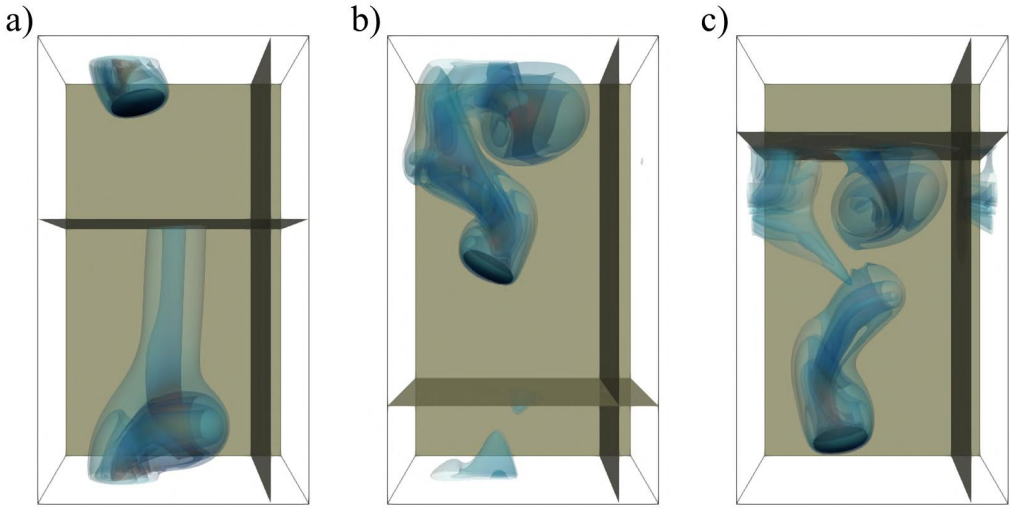

Source: Own elaboration.

As shown in the plots in Graph 19, when Ga $= 250$, the particle experiences a chaotic motion with its x and y velocities presenting almost the same magnitude and with the angular velocities in phase.

Graph 19 – (a) Horizontal and (b) angular velocities obtained in the present work with Ga $= 250$.

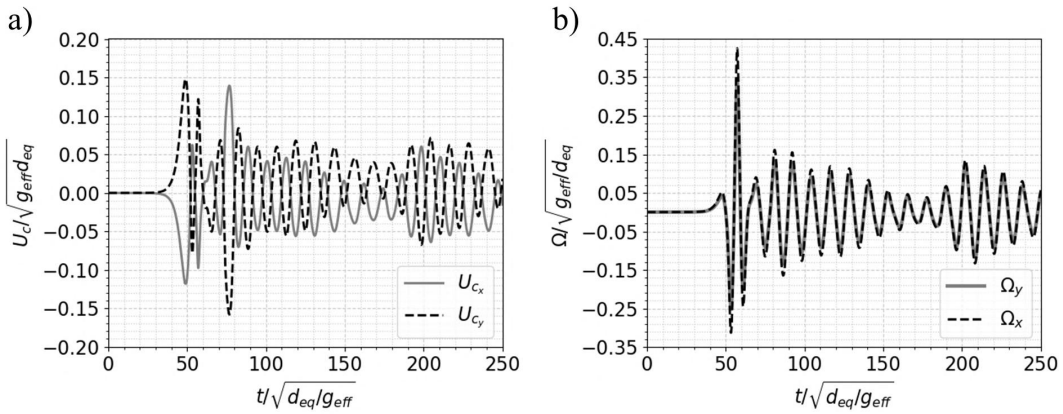

Source: Own elaboration.

Though the movement can be delineated in a single plane, the boundary relocation is applied at all directions, as illustrated in Figure 44.

Figure 44 – Vorticity contours obtained in the present work with Ga $= 250$ at (a) $t/\sqrt{d_{eq}/g_{eff}} = 48.83$, (b) $t/\sqrt{d_{eq}/g_{eff}} = 56.97$, and (c) $t/\sqrt{d_{eq}/g_{eff}} = 65.10$.

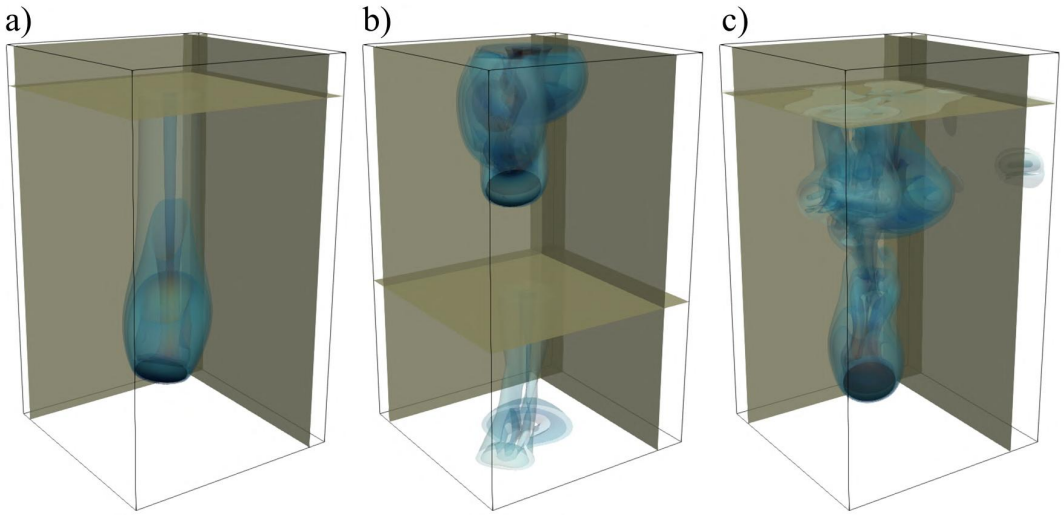

Source: Own elaboration.

It is easy to notice that the onset of particle horizontal motion occurs earlier as the Galileo number increases. The boundary relocation scheme has not caused any apparent deterioration of algorithm stability. With Ga $= 250$, the technique was evoked for the negative and positive directions of x- and y-axes, since the particle inverts its horizontal motion direction, accounting for both cases illustrated in Figure 26.

5.2 SETTLING OF SPHEROIDS IN VISCOPLASTIC FLUID

To investigate shape influences on viscoplastic settling, an spheroidal particle with $d_{\text{eq}} = 32$ and $m^* = 1.1$ was simulated for the same Bi_S adopted previously for the sphere (Section 4.8), but varying the aspect ratio χ and orientation θ_0 of the solid-body. The domain configuration is schematized in Figure 45.

Figure 45 – Domain configuration adopted in the simulations of spheroid settling in viscoplastic fluid.

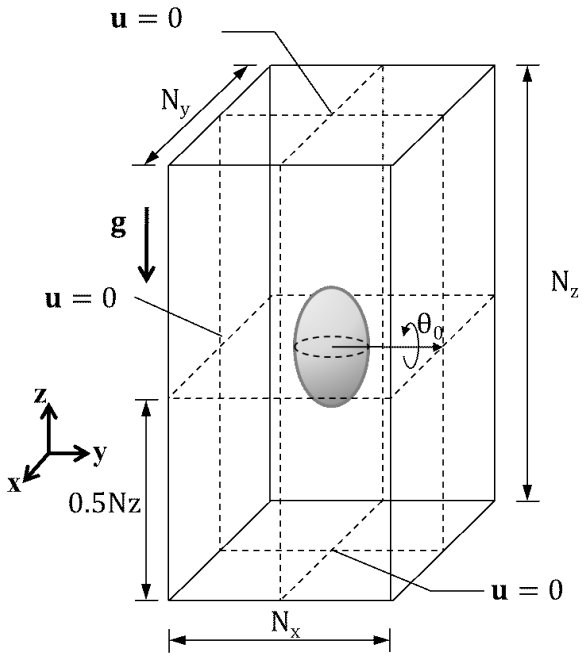

Source: Own elaboration.

Simulations were conducted for oblate and prolate spheroids of aspect ratio $\chi = 1/3$ and $\chi = 3$ respectively. The ellipsoids were then analyzed for initial inclinations θ_0 of 0 and $90°$. Simulation parameters were set for a $d_{\text{eq}} = 32$ in a $256 \times 256 \times 256$ computational grid for all cases except for the prolate spheroid with $\theta_0 = 0$, to which a $224 \times 224 \times 320$ grid was adopted. The values obtained for C_S are shown in Graph 20. The prolate and oblate spheroids with $\theta_0 = 90°$ and $\theta_0 = 0$, respectively, presented higher values of C_S than the sphere. This can be attributed to a larger cross-sectional area, which also results in smaller values of C_S for prolate and oblate particles with $\theta_0 = 0$ and $\theta_0 = 90°$, respectively.

Graph 20 – Values obtained for Stokes drag coefficient in ellipsoid settling simulations for (a) prolate and (b) oblate spheroids. Dashed lines represent a exponential curve fit.

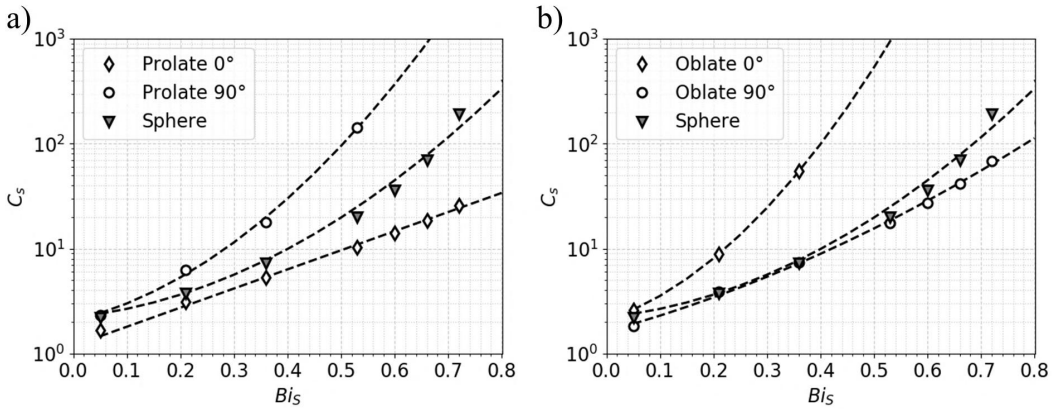

Source: Own elaboration.

For the prolate spheroid with $\theta_0 = 90°$ and Bi ≥ 0.6, the vertical velocity oscillated around zero, indicating that there is a shape influence on the value of critical yield Y_{crit}. The yielded region for the prolate spheroid with $\text{Bi}_S = 0.36$ at both orientations is shown in Figure 46 with shear rate scale normalized dividing it by $\sqrt{g/d_{\text{eq}}}$.

Figure 46 – Shape of the yielded region for (a) sphere, and (b) prolate spheroids with (b) $\theta_0 = 90°$ and (c) $\theta_0 = 0$ at $\text{Bi}_S = 0.36$.

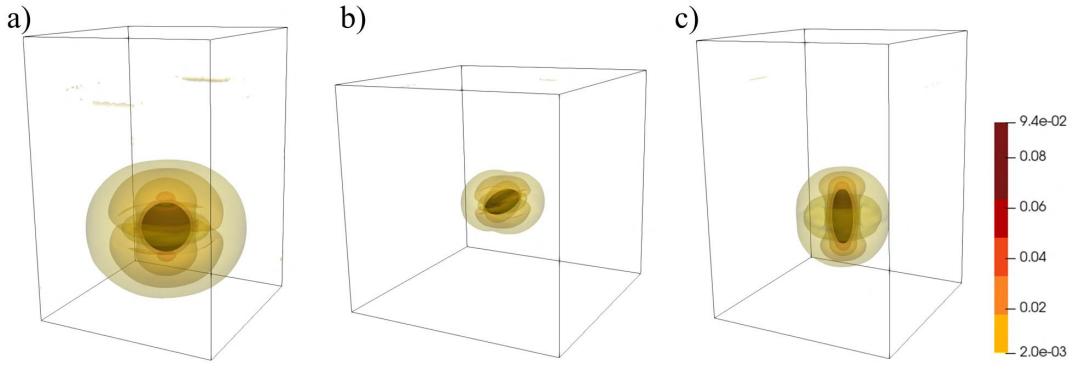

Source: Own elaboration.

Though the prolate spheroid reaches higher shear rate values, the size of its yielded region is smaller than for a sphere of the same volume. This is also true for the oblate spheroid, as shown in Figure 47, in which it is easily noticeable the reduced size of the yielded region for an oblate particle settling, especially for $\theta_0 = 90°$.

After the initial verification of shape influences on particle settling in viscoplastic fluid, the present work proceeds with an investigation of an inclined prolate spheroid settling at moderate Reynolds number.

Figure 47 – Shape of the yielded region for (a) sphere, and (b) oblate spheroids with (b) $\theta_0 = 90°$ and (c) $\theta_0 = 0$ at Bi$_S = 0.36$.

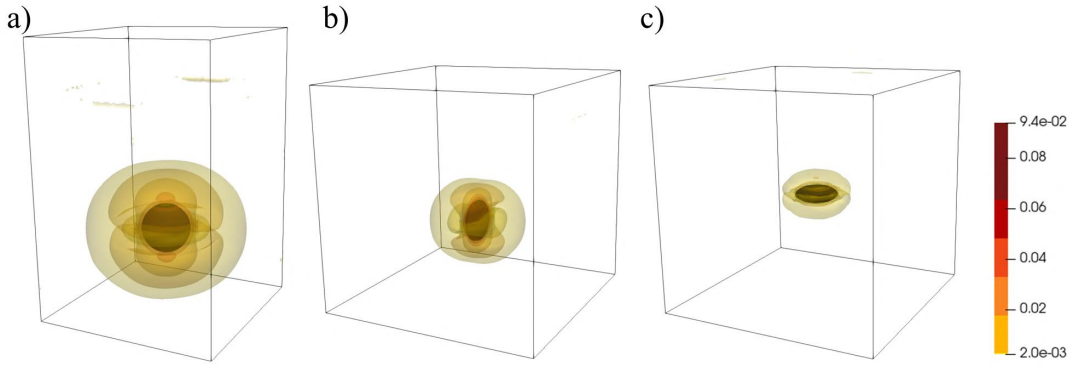

Source: Own elaboration.

5.3 INCLINED PROLATE SPHEROID IN VISCOPLASTIC FLUID

At moderate to high Reynolds numbers, it is more appropriate to work with a velocity scaling U_I given by (YU *et al.*, 2004):

$$U_I = \sqrt{\frac{4}{3}\left(m^* - 1\right) d_{\text{eq}} g}. \tag{122}$$

The Reynolds and Bingham numbers can then be defined from U_I. A series of subsequent simulations is then set for Re$_I = 100$ with $\eta_0 = 0.01$ and Bi$_I$ of 0.01, 0.1, 1 and 2. The aspect ratio of the ellipsoid is fixed $\chi = 2$ and the equivalent diameter $d_{\text{eq}} = 24$ in a $168 \times 168 \times 360$ computational grid. The particle initial inclination was set $\theta_0 = 45°$. As the Bingham number increases, vertical velocity reduces and solid-body travels larger horizontal paths before assuming a steady motion, as shown in Graph 21.

Graph 21 – Plots of paths traveled by the particle at different Bi$_I$ for $t/\sqrt{(d_{\text{eq}}/g)} = 190.18$ in (a) reduced and (b) larger scales.

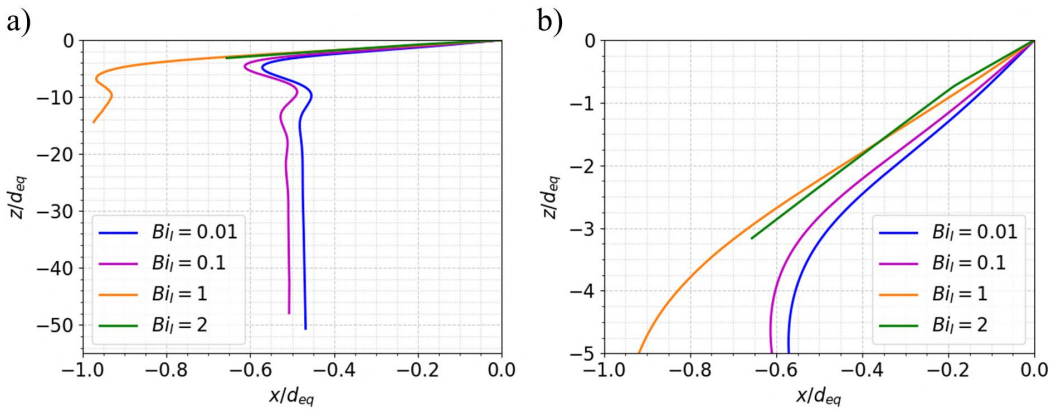

Source: Own elaboration.

The normalized shear rate contours at $t/\sqrt{(d_{\text{eq}}/g)} = 190.18$ are shown in the same scale for all simulations in Figure 48, in which the reduction of the yielded region is clearly evidenced. At the end of simulations, the particle presented an angular displacement of almost $45°$ counterclockwise, except for $\text{Bi}_I = 2$, in which the solid-body had an angular displacement of approximately $-3.40°$ clockwise.

Figure 48 – Normalized shear rate for (a) $\text{Bi}_I = 0.01$, (b) $\text{Bi}_I = 0.1$, (c) $\text{Bi}_I = 1$ and (d) $\text{Bi}_I = 2$.

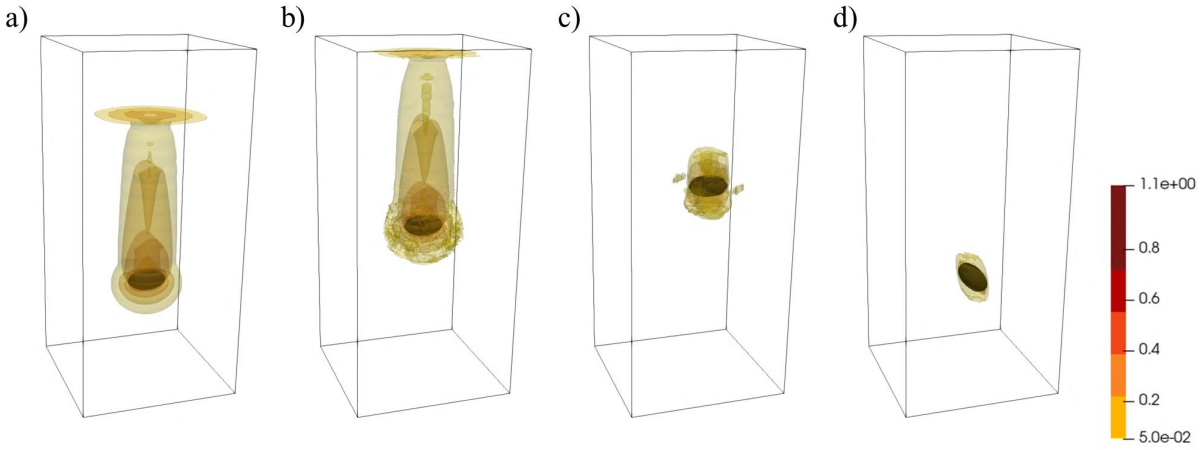

Source: Own elaboration.

This constraint in rotation can be partially explained by the reduction of the yielded region, while the change in direction of rotation when $\text{Bi}_I = 2$ can be due to the formation of a plastic torus encompassing the ellipsoidal particle. This is shown in Figure 49 using a more detailed scale for the normalized shear rate.

Figure 49 – Yielded region surrounding the particle with $\text{Bi}_I = 2$ and at $t/\sqrt{(d_{\text{eq}}/g)} = 9.51$, showing the plastic torus formed around the particle.

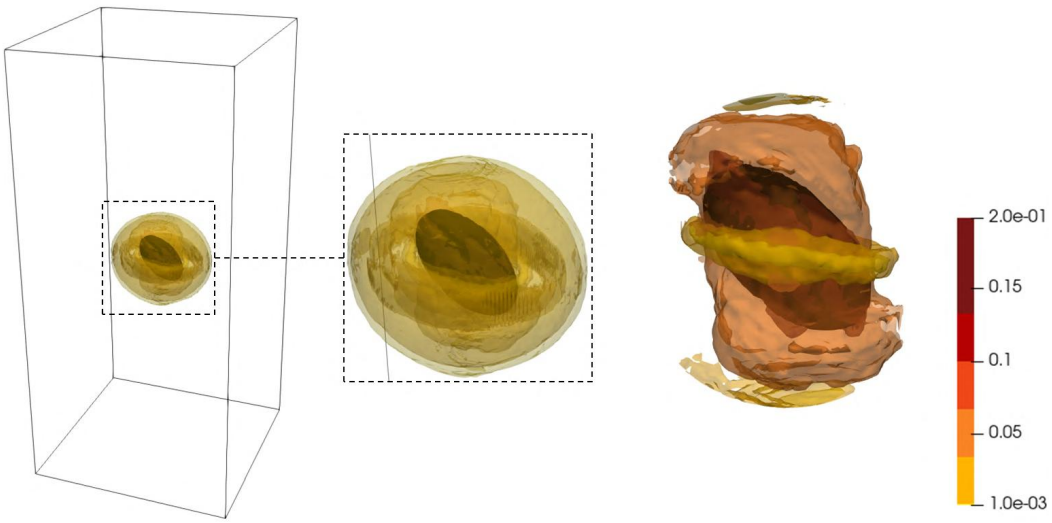

Source: Own elaboration.

The plastic torus surrounding the ellipsoid can impose a binary moment due to reaction forces resulting from an initial tendency of particle to assume a counterclockwise rotation, as illustrated in Figure 50.

Figure 50 – Schematic of reaction forces and direction of velocity for an inclined ellipsoidal particle settling in viscoplastic fluid at high Bingham number.

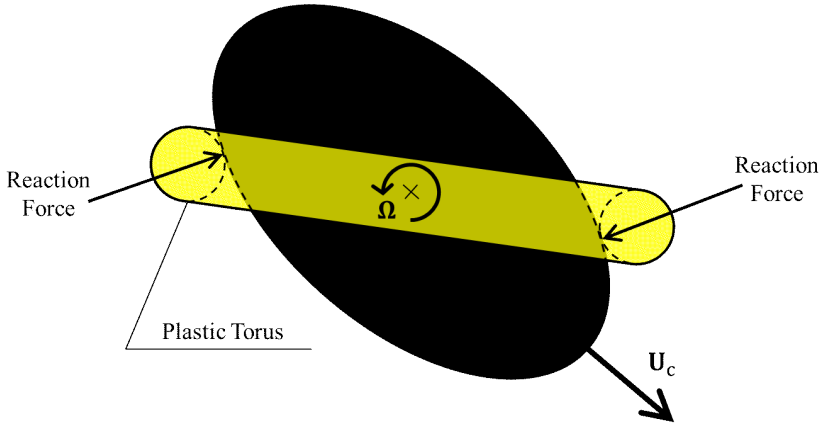

Source: Own elaboration.

As the increase of Bingham number also constrains the rotation, it takes a longer time for the particle to reach a vertical equilibrium position, resulting in a larger horizontal displacement. The trajectory traveled by the inclined particle at $\mathrm{Bi}_I = 2$ for 600,000-time steps is shown in Graph 22, in which a much more accentuated horizontal motion is perceived.

Graph 22 – Trajectory of a prolate spheroid with an initial inclination of $45°$ and $\mathrm{Bi}_I = 2$. The $x : y$ scale from the plot is 1:10.

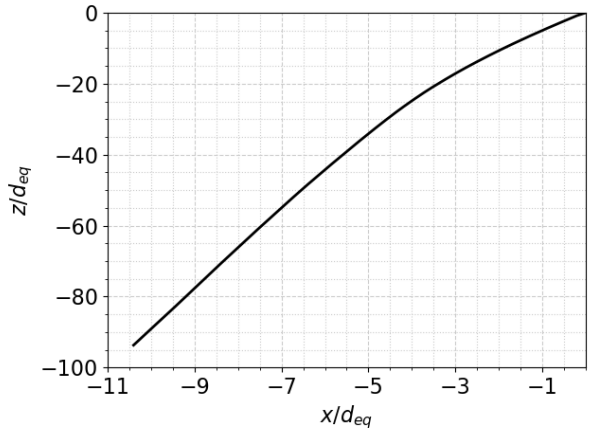

Source: Own elaboration.

This series of analyses confirms the ability of the developed algorithm to simulate an ellipsoidal particle settling in viscoplastic fluid.

5.4 CHAPTER CLOSURE

Simulations in Newtonian fluid predicted a variety of motion patterns for oblate spheroids that change as the Galileo number is increased. At smaller values of Ga the solid-body travels a straight path, going to periodic, oblique periodic and reaching chaotic regime at the highest Ga simulated. Present work simulations reported a good agreement with the results from Ardekani *et al.* (2016) for both qualitative aspects of motions and terminal values of Reynolds numbers.

The analyses with ellipsoidal particles in viscoplastic fluid showed the influence of shape on Stokes drag coefficient, it was also shown that the orientation of the particle can affect its terminal velocity. At simulations with an inclined ellipsoid, the capability of algorithm on simulating settling in viscoplastic fluid at high Reynolds number was put to test. It was also demonstrated how the shape of the yielded region can impact on the motion of the particle. For an elevated Bingham number, there is the formation of a plastic torus that can be responsible for a change in the direction of solid-body rotation.

6 SUMMARY AND CONCLUSIONS

In this project, an scheme for the lattice Boltzmann method (LBM) to perform fully-resolved simulations of an ellipsoidal particle settling in unbounded Newtonian and Bingham fluids-domain was developed. A practical consequence of the proposed scheme is the ability to solve particle settling for longer trajectories or reducing by order of magnitude the number of grid nodes required to solve an immersed particle flow. With the increasing popularity of LBM, motivated by its high parallel efficiency, it is desired that the use of the boundary relocation scheme can help on reducing the severe memory demands of the method.

The particle-fluid coupling was treated with the well-established immersed boundary method (IBM), to which a proper compensation of internal fluid mass based on the strategy from Suzuki and Inamuro (2011) was developed. A detailed description of a mesh generation procedure for ellipsoidal particles was provided. The numerical stability of the combined IB-LBM methods was assured by the regularization of ghost moments (LATT; CHOPARD, 2006; MATTILA *et al.*, 2017). The implementation of the boundary relocation scheme decreased the numerical efficiency of the plain IB-LB methods by only 0.92%. An apparent viscosity treatment with the approach developed from Lugarini *et al.* (2020) allowed for simulations using the Bingham model. As viscoplastic fluids present a yield-stress, they are capable of keeping particles suspended if the appropriate conditions are met. This characteristic is of great interest in the oil industry, as it is necessary for the drilling mud to hold cuttings of most varied shapes still during an operational stop.

The accuracy of the particle dynamics description was confirmed through comparison with analytical, experimental, and DNS solutions. It was observed that the proximity of lateral boundaries might have a significant effect on the object velocity, which means the numerical domain has to be designed such that the velocity field has a variation close to zero before reaching the lateral boundaries. For a sphere ascending with $\mathrm{Ga} = 173$, present work simulation reproduced very well the trajectory depicted in experimental data. The Bingham model was successfully implemented, with present work results showing good agreement with available data of a sphere settling in viscoplastic fluid at creeping flow.

For the settling of an oblate spheroid, good agreement with the DNS results from Ardekani *et al.* (2016) was shown, both in terms of flow regimes and terminal Reynolds numbers. However, it was employed nearly 50 times fewer grid nodes with the boundary relocation scheme.

The current numerical approach was capable of yielding good representation for all the four test cases investigated. For simulations in viscoplastic fluid, in which the aspect ratio of the spheroids was changed, it was observed that the shape of a solid-body can have significant impact on the particle's vertical velocity and the yielded region. When analyzing the sedimentation of an inclined prolate spheroid, it was shown that the increase of yield-stress of viscoplastic fluid not only reduces vertical velocity but also restrains and can even change the direction of ellipsoid rotation. It was then suggested that this shift may occur due to the reaction forces from plastic torus that is formed around the particle at high Bingham numbers. The constrain of rotation also results in longer periods before the solid-body reaches a vertical inclination, as a consequence, the particle travels larger horizontal paths before switching to a purely vertical motion.

6.1 RECOMMENDATIONS

Present work aimed to put forward an efficient numerical method for the simulation of single-particle settling in quiescent Newtonian and viscoplastic fluid. Through LBM, the flow evolution is solved explicitly, allowing for parallelization of collision and streaming operations. Further parametric studies can yet be conducted, as the herein validated method is applicable to a high variety of ellipsoidal geometries in Newtonian and Bingham fluid flows.

Computational limitations regarding maximum domain size emphasize that there is plenty of room for improvement, as it is possible to implement the developed algorithm in a multi-GPU system. Though boundary relocation scheme has no restrictions regarding particle geometry, this project restricted only on the study of spheroidal particles and future studies could include assessments with solid bodies of more complex shapes. The boundary relocation scheme can yet be highly profitable for aerodynamics analyses with a virtually infinite domain.

It is also employed IBM in its most general form which is testified to reach a first-order error decay. Thus, a more sophisticated description of fluid-structure interaction could bring improvement to the developed scheme. As the underlying motivation of this project resides on its application in the study of cuttings transport in oil industry, where the drilling muds are fluids of high complexity, it is highly desirable to extend the numerical method to cover for other non-Newtonian behaviors, such as elasticity and thixotropy. The extension for multiple particles is highly desirable, as it could be used for hindered settling analyses, however the scheme's suitability is yet to be addressed. The boundary relocation scheme would require modifications or a different approach to operate in configurations with multiple particles.

REFERENCES

ABBASSI, H.; TURKI, S.; NASRALLAH, S. B. Channel flow past bluff-body: outlet boundary condition, vortex shedding and effects of buoyancy. **Computational Mechanics**, Springer, v. 28, n. 1, p. 10–16, 2002.

ADACHI, K.; YOSHIOKA, N. On creeping flow of a visco-plastic fluid past a circular cylinder. **Chemical Engineering Science**, Elsevier, v. 28, n. 1, p. 215–226, 1973.

ANDRES, U. Equilibrium and motion of spheres in a viscoplastic liquid. *In*: **Doklady Akademii Nauk**. *[S.l.: s.n.]*, 1960. v. 133, n. 4, p. 777–780.

ANSLEY, R. W.; SMITH, T. N. Motion of spherical particles in a Bingham plastic. **AIChE Journal**, Wiley Online Library, v. 13, n. 6, p. 1193–1196, 1967.

ARDEKANI, M. N.; COSTA, P.; BREUGEM, W. P.; BRANDT, L. Numerical study of the sedimentation of spheroidal particles. **International Journal of Multiphase Flow**, Elsevier, v. 87, p. 16–34, 2016.

ARPACI, V. S. **Conduction heat transfer**. *[S.l.]*: Addison-Wesley, Reading, Massachusetts, 1966.

ATAPATTU, D. D.; CHHABRA, R. P.; UHLHERR, P. H. T. Wall effect for spheres falling at small Reynolds number in a viscoplastic medium. **Journal of Non-Newtonian Fluid Mechanics**, Elsevier, v. 38, n. 1, p. 31–42, 1990.

ATAPATTU, D. D.; CHHABRA, R. P.; UHLHERR, P. H. T. Creeping sphere motion in Herschel-Bulkley fluids: flow field and drag. **Journal of Non-Newtonian Fluid Mechanics**, Elsevier, v. 59, n. 2-3, p. 245–265, 1995.

AUGUSTE, F.; MAGNAUDET, J. Path oscillations and enhanced drag of light rising spheres. **Journal of Fluid Mechanics**, Cambridge University Press, v. 841, p. 228–266, 2018.

AUGUSTE, F.; MAGNAUDET, J.; FABRE, D. Falling styles of disks. **Journal of Fluid Mechanics**, Cambridge University Press, v. 719, p. 388–405, 2013.

BALACHANDRAN, P. **Fundamentals of compressible fluid dynamics**. *[S.l.]*: PHI Learning Pvt. Ltd., 2006.

BEAULNE, M.; MITSOULIS, E. Creeping motion of a sphere in tubes filled with Herschel–Bulkley fluids. **Journal of Non-Newtonian Fluid Mechanics**, Elsevier, v. 72, n. 1, p. 55–71, 1997.

BEENAKKER, J. J. M.; COHEN, E. G. D.; THIRRING, W. The Boltzmann equation, theory and applications. Springer Vienna, 1973.

BERIS, A. N.; TSAMOPOULOS, J. A.; ARMSTRONG, R. C.; BROWN, R. A. Creeping motion of a sphere through a Bingham plastic. **Journal of Fluid Mechanics**, Cambridge University Press, v. 158, p. 219–244, 1985.

BHATNAGAR, P.; GROSS, E.; KROOK, M. A model for collision processes in gases. **Physical Review**, v. 94, n. 3, p. 511, 1954.

BIRD, R. B.; ARMSTRONG, R. C.; HASSAGER, O. **Dynamics of polymeric liquids. Vol. 1: Fluid mechanics**. *[S.l.: s.n.]*, 1987.

BLACKERY, J.; MITSOULIS, E. Creeping motion of a sphere in tubes filled with a Bingham plastic material. **Journal of Non-Newtonian Fluid Mechanics**, Elsevier, v. 70, n. 1-2, p. 59–77, 1997.

BOARDMAN, G.; WHITMORE, R. L. Yield stress exerted on a body immersed in a Bingham fluid. **Nature**, Springer, v. 187, n. 4731, p. 50–51, 1960.

BOLTZMANN, L. Weitere Studien über das Wärmegleichgewicht unter Gasmolekülen. **Wiener Berichte**, v. 66, p. 275–370, 1872.

BOLTZMANN, L. **Über die Beziehung zwischen dem zweiten Hauptsatze des mechanischen Wärmetheorie und der Wahrscheinlichkeitsrechnung, respective den Sätzen über das Wärmegleichgewicht**. *[S.l.]*: Kk Hof-und Staatsruckerei, 1877.

BOLTZMANN, L. **Vorlesungen über Gastheorie, 2 vols**. *[S.l.: s.n.]*, 1896, 1898.

BOUSSINESQ, J. Mémoire sur l'influence des frottements dans les mouvements réguliers des fluids. **Journal de Mathématiques Pures et Appliquées**, v. 13, n. 2, p. 377–424, 1868.

BOUZIDI, M.; FIRDAOUSS, M.; LALLEMAND, P. Momentum transfer of a Boltzmann-lattice fluid with boundaries. **Physics of Fluids**, American Institute of Physics, v. 13, n. 11, p. 3452–3459, 2001.

BROOKES, G. F.; WHITMORE, R. L. Drag forces in Bingham plastics. **Rheologica Acta**, Springer, v. 8, n. 4, p. 472–480, 1969.

BUICK, J. M.; GREATED, C. A. Gravity in a lattice Boltzmann model. **Physical Review E**, APS, v. 61, n. 5, p. 5307, 2000.

CAIAZZO, A.; MADDU, S. Lattice Boltzmann boundary conditions via singular forces: Irregular expansion analysis and numerical investigations. **Computers & Mathematics with Applications**, Elsevier, v. 58, n. 5, p. 930–939, 2009.

CATE, A. T.; NIEUWSTAD, C. H.; DERKSEN, J. J.; AKKER, H. E. A. Van den. Particle imaging velocimetry experiments and lattice-Boltzmann simulations on a single sphere settling under gravity. **Physics of Fluids**, American Institute of Physics, v. 14, n. 11, p. 4012–4025, 2002.

CHAPARIAN, E.; FRIGAARD, I. A. Cloaking: Particles in a yield-stress fluid. **Journal of Non-Newtonian Fluid Mechanics**, Elsevier, v. 243, p. 47–55, 2017a.

CHAPARIAN, E.; FRIGAARD, I. A. Yield limit analysis of particle motion in a yield-stress fluid. **Journal of Fluid Mechanics**, Cambridge University Press, v. 819, p. 311–351, 2017b.

CHAPMAN, S.; COWLING, T. G.; BURNETT, D. **The mathematical theory of non-uniform gases: an account of the kinetic theory of viscosity, thermal conduction and diffusion in gases**. *[S.l.]*: Cambridge university press, 1990.

CHHABRA, R. P. **Bubbles, drops, and particles in non-Newtonian fluids**. *[S.l.]*: CRC Press, 2006.

CHRUST, M.; BOUCHET, G.; DUŠEK, J. Numerical simulation of the dynamics of freely falling discs. **Physics of Fluids**, American Institute of Physics, v. 25, n. 4, p. 044102, 2013.

CHRUST, M.; GOUJON-DURAND, S.; WESFREID, J. E. Loss of a fixed plane of symmetry in the wake of a sphere. **Journal of Fluids and Structures**, Elsevier, v. 41, p. 51–56, 2013.

CONCHA, F.; ALMENDRA, E. R. Settling velocities of particulate systems, 1. settling velocities of individual spherical particles. **International Journal of Mineral Processing**, Elsevier, v. 5, n. 4, p. 349–367, 1979.

COURANT, R.; FRIEDRICHS, K.; LEWY, H. On the partial difference equations of mathematical physics. **IBM Journal of Research and Development**, IBM, v. 11, n. 2, p. 215–234, 1967.

DAI, W.; PUPESCHI, S.; HANAOR, D.; GAN, Y. Influence of gas pressure on the effective thermal conductivity of ceramic breeder pebble beds. **Fusion Engineering and Design**, Elsevier, v. 118, p. 45–51, 2017.

DASH, S. M.; LEE, T. S.; LIM, T. T.; HUANG, H. A flexible forcing three dimension IB–LBM scheme for flow past stationary and moving spheres. **Computers & Fluids**, Elsevier, v. 95, p. 159–170, 2014.

DERKSEN, J. J. Direct simulations of spherical particle motion in Bingham liquids. **Computers & Chemical Engineering**, Elsevier, v. 35, n. 7, p. 1200–1214, 2011.

DEY, S.; ALI, S. Z; PADHI, E. Terminal fall velocity: the legacy of Stokes from the perspective of fluvial hydraulics. **Proceedings of the Royal Society A**, The Royal Society Publishing, v. 475, n. 2228, p. 20190277, 2019.

EWOLDT, R. H.; MCKINLEY, G. H. Mapping thixo-elasto-visco-plastic behavior. **Rheologica Acta**, Springer, v. 56, n. 3, p. 195–210, 2017.

FENG, Z. G.; MICHAELIDES, E. E. Robust treatment of no-slip boundary condition and velocity updating for the lattice-Boltzmann simulation of particulate flows. **Computers & Fluids**, Elsevier, v. 38, n. 2, p. 370–381, 2009.

FEYNMAN, R. P. **The Feynman Lectures on Physics**. *[S.l.]*: Addison Wesley Longman, 1970. v. 1.

FILIPPOVA, O.; HÄNEL, D. Grid refinement for lattice-BGK models. **Journal of Computational physics**, Elsevier, v. 147, n. 1, p. 219–228, 1998.

FRIGAARD, I. A.; NOUAR, C. On the usage of viscosity regularisation methods for visco-plastic fluid flow computation. **Journal of Non-Newtonian Fluid Mechanics**, Elsevier, v. 127, n. 1, p. 1–26, 2005.

GLOWINSKI, R.; PAN, T. W.; HESLA, T. I.; JOSEPH, D. D.; PERIAUX, J. A distributed Lagrange multiplier/fictitious domain method for the simulation of flow around moving rigid bodies: application to particulate flow. **Computer Methods in Applied Mechanics and Engineering**, Elsevier, v. 184, n. 2-4, p. 241–267, 2000.

GLOWINSKI, R.; PAN, T. W.; PERIAUX, J. A fictitious domain method for Dirichlet problem and applications. **Computer Methods in Applied Mechanics and Engineering**, Elsevier, v. 111, n. 3-4, p. 283–303, 1994.

GOLDSTEIN, S. The steady flow of viscous fluid past a fixed spherical obstacle at small Reynolds numbers. **Proceedings of the Royal Society of London. Series A, Containing Papers of a Mathematical and Physical Character**, The Royal Society London, v. 123, n. 791, p. 225–235, 1929.

GREENKORN, R. **Momentum, Heat, and Mass Transfer Fundamentals**. *[S.l.]*: CRC Press, 2018.

GUO, Z.; ZHENG, C.; SHI, B. Discrete lattice effects on the forcing term in the lattice Boltzmann method. **Physical Review E**, APS, v. 65, n. 4, p. 046308, 2002.

GUSHCHIN, V. A.; MATYUSHIN, R. V. Vortex formation mechanisms in the wake behind a sphere for 200< Re< 380. **Fluid Dynamics**, Springer, v. 41, n. 5, p. 795–809, 2006.

HABERMAN, W. L.; SAYRE, R. M. **Motion of rigid and fluid spheres in stationary and moving liquids inside cylindrical tubes**. *[S.l.]*, 1958.

HAERI, S.; SHRIMPTON, J. S. On the application of immersed boundary, fictitious domain and body-conformal mesh methods to many particle multiphase flows. **International Journal of Multiphase Flow**, Elsevier, v. 40, p. 38–55, 2012.

HAIDER, A.; LEVENSPIEL, O. Drag coefficient and terminal velocity of spherical and nonspherical particles. **Powder Technology**, Elsevier, v. 58, n. 1, p. 63–70, 1989.

HALWIDL, D. **Development of an effusive molecular beam apparatus**. *[S.l.]*: Springer, 2016.

HE, X.; LUO, L. S. Theory of the lattice Boltzmann method: From the Boltzmann equation to the lattice Boltzmann equation. **Physical Review E**, APS, v. 56, n. 6, p. 6811, 1997.

HEWITT, D. R.; BALMFORTH, N. J. Viscoplastic slender-body theory. **Journal of Fluid Mechanics**, Cambridge University Press, v. 856, p. 870–897, 2018.

HILL, R. **The mathematical theory of plasticity**. *[S.l.]*: Oxford University Press, 1998. v. 11.

HOROWITZ, M.; WILLIAMSON, C. H. K. The effect of Reynolds number on the dynamics and wakes of freely rising and falling spheres. **Journal of Fluid Mechanics**, Cambridge University Press, v. 651, p. 251–294, 2010.

HUANG, H.; YANG, X.; LU, X. Y. Sedimentation of an ellipsoidal particle in narrow tubes. **Physics of Fluids**, American Institute of Physics, v. 26, n. 5, p. 053302, 2014.

JEANS, J. **An introduction to the kinetic theory of gases**. *[S.l.]*: CUP Archive, 1940.

JEFFERY, G. B. The motion of ellipsoidal particles immersed in a viscous fluid. **Proceedings of the Royal Society of London. Series A, Containing papers of a mathematical and physical character**, The Royal Society London, v. 102, n. 715, p. 161–179, 1922.

JENNY, M.; DUŠEK, J. Efficient numerical method for the direct numerical simulation of the flow past a single light moving spherical body in transitional regimes. **Journal of Computational Physics**, Elsevier, v. 194, n. 1, p. 215–232, 2004.

JENNY, M.; DUŠEK, J.; BOUCHET, G. Instabilities and transition of a sphere falling or ascending freely in a Newtonian fluid. **Journal of Fluid Mechanics**, Cambridge University Press, v. 508, p. 201–239, 2004.

JOSSIC, L.; MAGNIN, A. Drag and stability of objects in a yield stress fluid. **AIChE Journal**, Wiley Online Library, v. 47, n. 12, p. 2666–2672, 2001.

JUNK, M.; YANG, Z. Outflow boundary conditions for the lattice Boltzmann method. **Progress in Computational Fluid Dynamics, an International Journal**, Inderscience Publishers, v. 8, n. 1-4, p. 38–48, 2008.

KISELEV, A. P. **Kiselev's geometry: Stereometry**. *[S.l.]*: Sumizdat, 2008.

KLAMKIN, M. S. Elementary approximations to the area of n-dimensional ellipsoids. **The American Mathematical Monthly**, Taylor & Francis, v. 78, n. 3, p. 280–283, 1971.

KLAMKIN, M. S. Corrections to "elementary approximations to the area of N-dimensional ellipsoids" (this monthly, 78 (1971) 280–283). **The American Mathematical Monthly**, Taylor & Francis, v. 83, n. 6, p. 478–478, 1976.

KOZAK, J.; FRIEDRICH, D. Quaternion: An alternate approach to medical navigation. *In*: SPRINGER. **World Congress on Medical Physics and Biomedical Engineering, September 7-12, 2009, Munich, Germany**. *[S.l.]*, 2009. p. 321–323.

KRÜGER, T.; KUSUMAATMAJA, H.; KUZMIN, A.; SHARDT, O.; SILVA, G.; VIGGEN, E. M. **The lattice Boltzmann method**. *[S.l.]*: Springer, 2017. v. 10. 978–3 p.

KUIPERS, J. B. **Quaternions and rotation sequences: a primer with applications to orbits, aerospace, and virtual reality**. *[S.l.]*: Princeton University Press, 1999.

KUNDU, P.; COHEN, I.; DOWLING, D. **Fluid mechanics, 920 pp**. *[S.l.]*: Academic Press, New York, NY, 2012.

KUNSZT, P. Z.; SZALAY, A. S.; THAKAR, A. R. The hierarchical triangular mesh. *In*: **Mining the Sky**. *[S.l.]*: Springer, 2001. p. 631–637.

LADD, A. J. C. Numerical simulations of particulate suspensions via a discretized Boltzmann equation. Part 1. Theoretical foundation. **Journal of Fluid Mechanics**, Cambridge University Press, v. 271, p. 285–309, 1994a.

LADD, A. J. C. Numerical simulations of particulate suspensions via a discretized Boltzmann equation. Part 2. Numerical results. **Journal of Fluid Mechanics**, Cambridge University Press, v. 271, p. 311–339, 1994b.

LALLEMAND, P.; LUO, L. S. Lattice Boltzmann method for moving boundaries. **Journal of Computational Physics**, Elsevier, v. 184, n. 2, p. 406–421, 2003.

LANEY, C. B. **Computational gasdynamics**. *[S.l.]*: Cambridge University Press, 1998.

LATT, J.; CHOPARD, B. Lattice Boltzmann method with regularized pre-collision distribution functions. **Mathematics and Computers in Simulation**, Elsevier, v. 72, n. 2-6, p. 165–168, 2006.

LIU, B. T.; MULLER, S. J.; DENN, M. M. Convergence of a regularization method for creeping flow of a Bingham material about a rigid sphere. **Journal of Non-Newtonian Fluid Mechanics**, Elsevier, v. 102, n. 2, p. 179–191, 2002.

LUGARINI, A.; FRANCO, A. T.; PHILIPPI, P. C. Lattice Boltzmann method for viscoplastic fluid flow based on regularization of ghost moments. **Journal of Non-Newtonian Fluid Mechanics**, Elsevier, v. 286, p. 104413, 2020.

MACOSKO, C. W. **Rheology principles**. *[S.l.]*: VCH Publishes, 1994.

MAGARVEY, R. H.; MACLATCHY, C. S. Vortices in sphere wakes. **Canadian Journal of Physics**, NRC Research Press, v. 43, n. 9, p. 1649–1656, 1965.

MATTILA, K. K.; PHILIPPI, P. C.; HEGELE, L. A. High-order regularization in lattice-Boltzmann equations. **Physics of Fluids**, AIP Publishing LLC, v. 29, n. 4, p. 046103, 2017.

MAXWELL, J. C. On the dynamical theory of gases. **Philosophical transactions of the Royal Society of London**, The Royal Society London, n. 157, p. 49–88, 1867.

MAXWORTHY, T. Accurate measurements of sphere drag at low Reynolds numbers. **Journal of Fluid Mechanics**, Cambridge University Press, v. 23, n. 2, p. 369–372, 1965.

MCNAMARA, G. R.; ZANETTI, G. Use of the Boltzmann equation to simulate lattice-gas automata. **Physical Review Letters**, APS, v. 61, n. 20, p. 2332, 1988.

MOHAMAD, A. A. **Lattice Boltzmann method**. *[S.l.]*: Springer, 2011. v. 70.

MOUGIN, G.; MAGNAUDET, J. The generalized Kirchhoff equations and their application to the interaction between a rigid body and an arbitrary time-dependent viscous flow. **International Journal of Multiphase Flow**, Elsevier, v. 28, n. 11, p. 1837–1851, 2002.

NARDI, V. G. **A numerical study of particle settling in Power-law fluids using lattice-Boltzmann method**. 2018. MSc Dissertation — Federal University of Technology - Paraná, 2018.

NGUYEN, J.-P. **Drilling: oil and gas field development techniques**. *[S.l.]*: Editions Technip, 1996.

OLDROYD, J. G. Two-dimensional plastic flow of a Bingham solid: a plastic boundary-layer theory for slow motion. *In*: CAMBRIDGE UNIVERSITY PRESS. **Mathematical Proceedings of the Cambridge Philosophical Society**. *[S.l.]*, 1947. v. 43, n. 3, p. 383–395.

OMLAND, T. H. Particle settling in non-Newtonian drilling fluids. University of Stavanger, Norway, 2009.

OSEEN, C. W. Über die Stokes'sche Formel, und über eine verwandte Aufgabe in der Hydrodynamik ark. **Math. Astronom. Fys**, v. 6, 1910.

OSEEN, C. W. Über den gültigkeitsbereich der stokesschen widerstandsformel. **Arkiv för Matematik, Astronomi och Fysik. Friedländer**, 1913.

PANTON, R. L. **Incompressible flow**. *[S.l.]*: John Wiley & Sons, 2013.

PAPANASTASIOU, T. C. Flows of materials with yield. **Journal of Rheology**, The Society of Rheology, v. 31, n. 5, p. 385–404, 1987.

PENG, C.; AYALA, O. M.; WANG, L. P. A comparative study of immersed boundary method and interpolated bounce-back scheme for no-slip boundary treatment in the lattice Boltzmann method: Part i, laminar flows. **Computers & Fluids**, Elsevier, v. 192, p. 104233, 2019.

PESKIN, C. S. Flow patterns around heart valves: a numerical method. **Journal of Computational Physics**, Elsevier, v. 10, n. 2, p. 252–271, 1972.

PESKIN, C. S. The immersed boundary method. **Acta Numerica**, Cambridge University Press, v. 11, p. 479–517, 2002.

PHILIPPI, P. C.; HEGELE, L. A.; SANTOS, L. O. E.; SURMAS, R. From the continuous to the lattice Boltzmann equation: The discretization problem and thermal models. **Physical Review E**, APS, v. 73, n. 5, p. 056702, 2006.

PINELLI, A.; NAQAVI, I. Z.; PIOMELLI, U.; FAVIER, J. Immersed-boundary methods for general finite-difference and finite-volume Navier–Stokes solvers. **Journal of Computational Physics**, Elsevier, v. 229, n. 24, p. 9073–9091, 2010.

PROUDMAN, I.; PEARSON, J. R. A. Expansions at small Reynolds numbers for the flow past a sphere and a circular cylinder. **Journal of Fluid Mechanics**, Cambridge University Press, v. 2, n. 3, p. 237–262, 1957.

PUTZ, A. M. V.; BURGHELEA, T. I.; FRIGAARD, I. A.; MARTINEZ, D. M. Settling of an isolated spherical particle in a yield stress shear thinning fluid. **Physics of Fluids**, American Institute of Physics, v. 20, n. 3, p. 033102, 2008.

QIAN, Y. H.; D'HUMIÈRES, D.; LALLEMAND, P. Lattice BGK models for Navier-Stokes equation. **EPL (Europhysics Letters)**, IOP Publishing, v. 17, n. 6, p. 479, 1992.

RAE, D. Yield stress exerted on a body immersed in a Bingham fluid. **Nature**, v. 194, n. 4825, p. 272–272, 1962.

RAHMANI, M.; WACHS, A. Free falling and rising of spherical and angular particles. **Physics of Fluids**, American Institute of Physics, v. 26, n. 8, p. 083301, 2014.

SCHILLER, L.; NAUMANN, A. A drag coefficient correlation. **Z. Ver. Deutsch. Ing**, v. 77, n. 318, p. e323, 1935.

SHAN, X.; YUAN, X. F.; CHEN, H. Kinetic theory representation of hydrodynamics: a way beyond the Navier–Stokes equation. **Journal of Fluid Mechanics**, Cambridge University Press, v. 550, p. 413–441, 2006.

SHENOY, A. R.; KLEINSTREUER, C. Influence of aspect ratio on the dynamics of a freely moving circular disk. **Journal of Fluid Mechanics**, Cambridge University Press, v. 653, p. 463–487, 2010.

SHI, X.; PHAN-THIEN, N. Distributed Lagrange multiplier/fictitious domain method in the framework of lattice Boltzmann method for fluid–structure interactions. **Journal of Computational Physics**, Elsevier, v. 206, n. 1, p. 81–94, 2005.

SILVA, G.; SEMIAO, V. First-and second-order forcing expansions in a lattice Boltzmann method reproducing isothermal hydrodynamics in artificial compressibility form. **Journal of Fluid Mechanics**, Cambridge University Press, v. 698, p. 282, 2012.

SOTO, H. P.; MARTINS-COSTA, M. L.; FONSECA, C.; FREY, S. A numerical investigation of inertia flows of Bingham-Papanastasiou fluids by an extra stress-pressure-velocity Galerkin least-squares method. **Journal of the Brazilian Society of Mechanical Sciences and Engineering**, SciELO Brasil, v. 32, n. SPE, p. 450–460, 2010.

SPALART, P. R.; MOSER, R. D.; ROGERS, M. M. Spectral methods for the navier-stokes equations with one infinite and two periodic directions. **Journal of Computational Physics**, Elsevier, v. 96, n. 2, p. 297–324, 1991.

STEWARTSON, K. XXXII. on the steady flow past a sphere at high Reynolds number using Oseen's approximation. **Philosophical Magazine**, Taylor & Francis, v. 1, n. 4, p. 345–354, 1956.

STOKES, G. G. On the effect of the internal friction of fluids on the motion of pendulums. Pitt Press Cambridge, v. 9, 1851.

SUCCI, S. **The lattice Boltzmann equation: for fluid dynamics and beyond**. *[S.l.]*: Oxford University Press, 2001.

SUZUKI, K.; INAMURO, T. Effect of internal mass in the simulation of a moving body by the immersed boundary method. **Computers & Fluids**, Elsevier, v. 49, n. 1, p. 173–187, 2011.

SWAMINATHAN, T. N.; MUKUNDAKRISHNAN, K.; HU, H. H. Sedimentation of an ellipsoid inside an infinitely long tube at low and intermediate Reynolds numbers. **Journal of Fluid Mechanics**, Cambridge University Press, v. 551, p. 357–385, 2006.

TABUTEAU, H.; COUSSOT, P.; BRUYN, J. R. de. Drag force on a sphere in steady motion through a yield-stress fluid. **Journal of Rheology**, The Society of Rheology, v. 51, n. 1, p. 125–137, 2007.

TANEDA, S. Experimental investigation of the wake behind a sphere at low Reynolds numbers. **Journal of the Physical Society of Japan**, The Physical Society of Japan, v. 11, n. 10, p. 1104–1108, 1956.

TOKPAVI, D.; MAGNIN, A.; JAY, P. Very slow flow of Bingham viscoplastic fluid around a circular cylinder. **Journal of Non-Newtonian Fluid Mechanics**, Elsevier, v. 154, n. 1, p. 65–76, 2008.

TOMOTIKA, S.; AOI, T. The steady flow of viscous fluid past a sphere and circular cylinder at small Reynolds numbers. **The Quarterly Journal of Mechanics and Applied Mathematics**, Oxford University Press, v. 3, n. 2, p. 141–161, 1950.

UHLMANN, M. An immersed boundary method with direct forcing for the simulation of particulate flows. **Journal of Computational Physics**, Elsevier, v. 209, n. 2, p. 448–476, 2005.

VALENTIK, L.; WHITMORE, R. L. The terminal velocity of spheres in Bingham plastics. **British Journal of Applied Physics**, IOP Publishing, v. 16, n. 8, p. 1197, 1965.

VOLAROVICH, M. P.; GUTKIN, A. M. Theory of flow of a viscoplastic medium. **Colloid J**, v. 15, p. 153, 1953.

WACHS, A.; FRIGAARD, I. A. Particle settling in yield stress fluids: limiting time, distance and applications. **Journal of Non-Newtonian Fluid Mechanics**, Elsevier, v. 238, p. 189–204, 2016.

WEISSTEIN, E. W. **CRC encyclopedia of mathematics**. *[S.l.]*: CRC Press Boca Raton, FL, 2009.

WHITEHEAD, A. N. On the motion of viscous incompressible fluids. **Quart. J. Math**, v. 23, p. 78, 1889.

YANG, X.; ZHANG, X.; LI, Z.; HE, G. W. A smoothing technique for discrete delta functions with application to immersed boundary method in moving boundary simulations. **Journal of Computational Physics**, Elsevier, v. 228, n. 20, p. 7821–7836, 2009.

YOSHIOKA, N.; ADACHI, K.; ISHIMURA, H. On creeping flow of a viscoplastic fluid past a sphere. **Kagaku Kogaku**, v. 10, n. 1144, p. 6–31, 1971.

YU, Z.; PHAN-THIEN, N.; FAN, Y.; TANNER, R. I. Viscoelastic mobility problem of a system of particles. **Journal of Non-Newtonian Fluid Mechanics**, Elsevier, v. 104, n. 2-3, p. 87–124, 2002.

YU, Z.; PHAN-THIEN, N.; TANNER, R. I. Dynamic simulation of sphere motion in a vertical tube. **Journal of Fluid Mechanics**, Cambridge University Press, v. 518, p. 61, 2004.

YU, Z.; WACHS, A. A fictitious domain method for dynamic simulation of particle sedimentation in Bingham fluids. **Journal of Non-Newtonian Fluid Mechanics**, Elsevier, v. 145, n. 2-3, p. 78–91, 2007.

ZHOU, W.; CHRUST, M.; DUŠEK, J. Path instabilities of oblate spheroids. **Journal of Fluid Mechanics**, Cambridge University Press, v. 833, p. 445–468, 2017.

ZHOU, W.; DUŠEK, J. Chaotic states and order in the chaos of the paths of freely falling and ascending spheres. **International Journal of Multiphase Flow**, Elsevier, v. 75, p. 205–223, 2015.

ZHU, L.; HE, G.; WANG, S.; MILLER, L.; ZHANG, X.; YOU, Q.; FANG, S. An immersed boundary method based on the lattice Boltzmann approach in three dimensions, with application. **Computers & Mathematics with Applications**, Elsevier, v. 61, n. 12, p. 3506–3518, 2011.